

Adsorption of (hetero-)organic Phthalocyanine and PTCDA thin films on Ag(111)

Christoph Kleimann

Adsorption of (hetero-)organic Phthalocyanine and PTCDA thin films on Ag(111)

Von der Fakultät für Mathematik, Informatik und
Naturwissenschaften der RWTH Aachen University zur
Erlangung des akademischen Grades eines Doktors der
Naturwissenschaften genehmigte Dissertation

vorgelegt von

Diplom-Physiker

Christoph Kleimann

aus Herford

Berichter: Universitätprofessor Christian Kumpf
Universitätprofessor Moritz Sokolowski

Tag der mündlichen Prüfung: 15.05.2013

Diese Dissertation ist auf den Internetseiten der
Hochschulbibliothek online verfügbar.

Forschungszentrum Jülich GmbH
Peter Grünberg Institut (PGI)
Functional Nanostructures at Surfaces (PGI-3)

Adsorption of (hetero-)organic Phthalocyanine and PTCDA thin films on Ag(111)

Christoph Kleimann

Schriften des Forschungszentrums Jülich
Reihe Schlüsseltechnologien / Key Technologies

Band / Volume 67

ISSN 1866-1807

ISBN 978-3-89336-888-4

Bibliographic information published by the Deutsche Nationalbibliothek.
The Deutsche Nationalbibliothek lists this publication in the Deutsche
Nationalbibliografie; detailed bibliographic data are available in the
Internet at <http://dnb.d-nb.de>.

Publisher and Distributor:	Forschungszentrum Jülich GmbH Zentralbibliothek 52425 Jülich Tel: +49 2461 61-5368 Fax: +49 2461 61-6103 Email: zb-publikation@fz-juelich.de www.fz-juelich.de/zb
Cover Design:	Grafische Medien, Forschungszentrum Jülich GmbH
Printer:	Grafische Medien, Forschungszentrum Jülich GmbH
Copyright:	Forschungszentrum Jülich 2013

Schriften des Forschungszentrums Jülich
Reihe Schlüsseltechnologien / Key Technologies, Band / Volume 67

D 82 (Diss., RWTH Aachen University, 2013)

ISSN 1866-1807
ISBN 978-3-80336-888-4

The complete volume is freely available on the Internet on the Jülicher Open Access Server (JUWEL) at www.fz-juelich.de/zh/juwell

Neither this book nor any part of it may be reproduced or transmitted in any form or by any means, electronic or mechanical, including photocopying, microfilming, and recording, or by any information storage and retrieval system, without permission in writing from the publisher.

The work described in this thesis was carried out at the
Peter Grünberg Institute (PGI-3), Forschungszentrum Jülich,
Germany

Supervisor:

Prof. Dr. Christian Kumpf

Referees:

1. Prof. Dr. Christian Kumpf, Forschungszentrum Jülich
2. Prof. Dr. Moritz Sokolowski, Bonn University

Disputation on May 15, 2013 at the RWTH Aachen University.

Board of examiners:

1. Prof. Dr. Christian Kumpf, Forschungszentrum Jülich
2. Prof. Dr. Moritz Sokolowski, Bonn University
3. Prof. Dr. Markus Morgenstern, RWTH Aachen University
4. Prof. Dr. Stefan Wessel, RWTH Aachen University

Contents

1	Introduction	1
2	Experimental methods	5
2.1	Low Energy Electron Diffraction	5
2.2	Scanning Tunneling Microscopy	9
2.3	X-ray Standing Waves	12
2.4	Pair potential calculations	15
2.5	Sample details and preparation	18
3	SnPc on Ag(111)	21
3.1	Scanning tunneling microscopy	23
3.1.1	Disordered phase at low coverages	23
3.1.2	Commensurate low temperature phase	29
3.1.3	Point-on-line phase at high coverages	32
3.2	Scanning tunneling spectroscopy	35
3.3	Pair potential calculations for SnPc	38
3.4	Conclusion	46
4	F₁₆CuPc on Ag(111)	49
4.1	Structural phase diagram	50
4.2	Disordered submonolayer regime at RT	52
4.3	Structural investigation of the ordered phase	55
4.3.1	LEED model	58
4.3.2	STM measurements	60
4.3.3	Origin of the structure formation	67
4.3.4	Growth of the 2nd layer	71
4.4	Conclusion	75
5	CuPc/F₁₆CuPc hetero-organic interfaces on Ag(111)	77
5.1	Laterally mixed layers of F ₁₆ CuPc and CuPc	79
5.1.1	Intermediate phase	80
5.1.2	CuPc-rich phase	91
5.1.3	F ₁₆ CuPc-rich phase	92
5.1.4	Conclusion	94
5.2	F ₁₆ CuPc on closed CuPc monolayers	96
5.2.1	SPA-LEED	96
5.2.2	XSW analysis of CuPc on Ag(111)	98
5.2.3	XSW analysis of F ₁₆ CuPc on CuPc/Ag(111)	104
5.2.4	Conclusion	113

Contents

6 F₁₆CuPc on PTCDA monolayers on Ag(111)	115
6.1 Structural phase diagram	116
6.2 LEED model	119
6.3 Layer distance	124
6.4 Conclusion	125
7 Summary	127
List of Acronyms	131
List of Figures	133
Bibliography	135
Acknowledgements	147
Curriculum Vitae	149

1 Introduction

Organic materials are frequently used in electronic devices due to their flexibility and the possibility for low cost mass fabrication. A lot of successful applications already exist for thin organic films, e.g., in organic light emitting diodes (OLEDs) [1], organic field effect transistors (OFETs) [2] or organic photovoltaic cells (OPVCs) [3, 4, 5]. However, many effects in these devices are still not understood. The development and optimization of new devices calls for a better understanding of the underlying processes at the interfaces (organic–organic or metal–organic) occurring in these systems, regarding, e.g., charge transfer. Hence, more fundamental research on the physical properties of contacts, interfaces, and thin films down to single molecular layers (monolayers), is necessary.

Consequently, the study of thin organic films on well defined surfaces has received increasing attention over the last decades. Knowledge about the structure formation in these films is crucial, since it influences, e.g., the electronic properties of the system. Of special interest for the conceptual design of organic electronic devices are interfaces between an organic material and a metal or semiconductor surface. In this context, the structure of the first layer of an organic adsorbate species on a substrate is decisive for the interface properties, which was the motivation for many studies on (sub-)monolayer films on well defined surfaces. While metal–organic interfaces have already been investigated quite extensively, the focus has recently shifted towards the investigation of organic–organic interfaces in hetero-organic adsorbate films.

The structural ordering of the first molecular adsorbate layer can also have a significant influence on the growth of higher layer. This is especially true for systems, in which the vertical interactions between the adsorbate molecules and the layer below (substrate or lower adsorbate layer) are dominant compared to lateral intermolecular interactions. In some cases, even the structure of thick films depends on the initial monolayer structure. To this extent, the self organized growth of molecules on well defined surfaces can be used to create specific structures, which is a ‘bottom-up’ approach for nanotechnology [6]. This self organized growth can be influenced by the choice of substrate and adsorbate atoms (or molecules) or by the variation of external parameters, such as the sample temperature. Crystalline substrates generally differ by their surface structure and the strength of interaction with molecules, leading to different potential energy landscapes for adsorbates. Temperature on the other hand changes the diffusivity of molecules on the surface and hence influences the balance between growth kinetics and thermodynamics. Higher sample temperatures may enable adsorbate molecules to overcome energy barriers and adopt structures, which are thermodynamically more stable.

1 Introduction

In many studies large, planar, π -conjugated molecules are investigated, which typically adsorb in a flat lying geometry on surfaces. Molecules in different layers are often bonded by vertical π -stacking in this case, which is, e.g., desirable for the photocurrent flow in organic solar cells. A common prototype for the investigation of large π -conjugated organic molecules on noble metal surfaces is PTCDA, for which a quite complete picture of structural and electronic properties has been achieved within the last decade [7]. Another popular choice for organic molecules are phthalocyanines, for which a rather unusual growth mode based on intermolecular repulsion was found on Ag(111) surfaces [8]. This class of molecules is the main subject of this work. Many variations of the basic phthalocyanine molecule exist, mainly differing by the metal atom or functional group in the center of the molecule. A different approach for tuning the molecular properties is fluorination, i.e. replacing the terminating hydrogen atoms by fluorine, which changes the electronic properties due to the large electron affinity of this atomic species. Since all these variants show different intermolecular and molecule–substrate interactions, the phthalocyanine family presents an interesting opportunity to customize desired surface structures.

This work shall contribute to the understanding of structure formation in metal–organic as well as hetero-organic interfaces by investigating different exemplary phthalocyanine variants on a Ag(111) surface, namely SnPc, CuPc, as well as the fluorinated variant F₁₆CuPc. While CuPc and F₁₆CuPc are rather flat in the gas phase, SnPc exhibits a permanent vertical dipole moment due to its bent geometry.

The organization of this work is as follows:

- All experimental methods are shortly introduced in chapter 2.
- The first experimental chapter 3 deals with the structure formation of SnPc films on Ag(111) surfaces as an example of a metal–organic interface. Thereby, previous scattering and spectroscopic measurements [9] were complemented by high resolution scanning tunneling microscopy (STM). Molecular orientations of the molecules have been determined to complete our picture about the structure formation in this system.
- A second metal–organic interface consisting of F₁₆CuPc on Ag(111) was investigated in detail by electron diffraction (SPA-LEED) and STM in chapter 4. Similarities and differences to the growth behavior of the related system CuPc/Ag(111) are discussed here.
- Afterwards in chapter 5, we turn our attention to hetero-organic systems formed by the two molecules CuPc and F₁₆CuPc, also adsorbed on the Ag(111) surface.

In part 5.1 we report results on *laterally* mixed films of both species. The rather complex structure formation behavior has been investigated by SPA-LEED. By controlling the macroscopic parameters temperature, coverage, and stoichiometric ratio of the two components, different structural phases could be formed on the surface.

In the second part, 5.2, the *vertical* stacking of these two molecules is dealt

with, using SPA-LEED and X-ray Standing Wave (XSW).

- In chapter 6 we present results on a second stacked system of $F_{16}CuPc$ on PTCDA/Ag(111) and discuss them in context with the system $F_{16}CuPc$ on CuPc/Ag(111) and earlier results on CuPc/PTCDA/Ag(111) by Stadtmüller et al. [10]. The influence of the lower adsorbate layer (interlayer) on the structure formation of the $F_{16}CuPc$ top layer is discussed. In addition to the lateral structure determination, the adsorption height of the top layer has been estimated experimentally by SPA-LEED to characterize the vertical interaction strength at the interface.
- Finally, a summary of the most important results is given in chapter 7.

For all systems investigated in the frame of this work, calculations of electrostatic and van-der-Waals potentials have been performed to help elucidating the role of intermolecular forces on the structure formation in organic thin films. Although organic molecules typically show a weak chemisorptive bonding character on Ag(111) surfaces which is not included in our calculations, we found that intermolecular potentials are sufficient to explain the structure formation in many cases.

2 Experimental methods

2.1 Low Energy Electron Diffraction

Electron diffraction was first discovered in 1927 by Davison and Germer [11] and has been one of the best established surface science techniques for decades. Structural informations about a sample are gained from the analysis of elastically scattered electrons. The prerequisite of surface sensitivity is naturally achieved because of the small mean free path of low energetic (10 to 100 eV) electrons within solids of about a few Ångstroms. In this energy range, the de Broglie wavelength $\lambda = \sqrt{\hbar^2/2m_e E}$ of the electrons is in the order of interatomic distances, so that measuring atomic arrangements in adsorbate layers becomes possible. One disadvantage compared to X-ray- or neutron-diffraction is that multiple scattering processes play a significant role in *Low Energy Electron Diffraction* (LEED). Hence, for a quantitative description of scattering intensities, the rather complex dynamic LEED theory is necessary. However, for describing the diffraction spot positions, multiple scattering effects can be neglected. Therefore, the simpler kinematic theory, which only treats single scattering events, is used in this work.

For scattering from a 3-dimensional crystal, diffraction spots can only be found at discrete points (Bragg reflexes) of the reciprocal lattice G according to the Laue conditions. On the other hand, in the case of diffraction from a single atomic layer, the Laue condition perpendicular to the surface is completely relaxed, as no periodicity is given in this direction. This leads to crystal truncation rods [12] with uniform intensity in the direction of \vec{K}_\perp . Electron diffraction represents an intermediate situation between the two extreme cases described above. The electron penetration depth is finite, but not limited to a single atomic layer. The results are lattice rods with a certain intensity modulation along \vec{K}_\perp . If the lateral structure of the layer(s) closest to the surface is different from the bulk structure, additional rods appear. Such a different symmetry can be caused by reconstruction or simply by an adsorbate layer.

The condition for observing LEED spots can be visualized by the well known Ewald construction, as shown in Fig. 2.1 a). The wave vector \vec{k}_0 of the incident electron beam is placed with its end pointing at the $(0,0)$ point of the reciprocal lattice and a sphere with radius $|\vec{k}|$ is drawn around its starting point. The scattering condition for the scattering vector component parallel to the surface,

$$\vec{K}_\parallel = \vec{k}_{f\parallel} - \vec{k}_{0\parallel} = \vec{G}_\parallel, \quad (2.1)$$

is fulfilled for every point where the Ewald sphere crosses a lattice rod. As a consequence of the relaxed 3rd Laue condition, diffraction spots are visible at

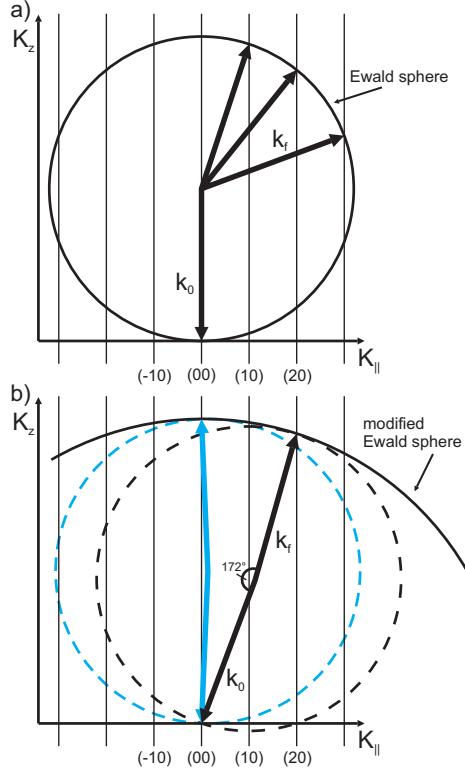


Figure 2.1: Ewald construction for visualization of the 2D scattering condition in a) conventional LEED and b) SPA-LEED. For wave vectors that end at intersection points of a lattice rod with the Ewald sphere, scattered intensity can be observed.

all electron energies in contrast to the case of bulk diffraction. If the energy is increased, the spots move inwards and more spots become visible. In the Ewald construction, this is visualized by an increase of the Ewald sphere radius.

In a conventional LEED system, electrons are emitted from an electron gun onto the sample under normal incidence. A grid system is used to reject most of the inelastically scattered electrons. The elastically scattered ones, which pass the grids, are reaccelerated and hit a half-spherical fluorescent screen. This way, a large part of the diffraction pattern can be observed immediately.

SPA-LEED

The LEED investigations described in this work were recorded by *Spot Profile Analysis LEED* (SPA-LEED) [14]. We will shortly introduce this technique

2.1 Low Energy Electron Diffraction

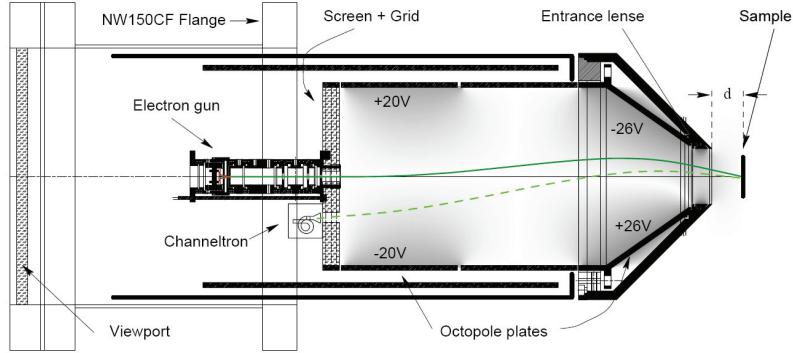


Figure 2.2: Setup of a SPA-LEED instrument, adapted from reference [13]

in the following. A more detailed review about SPA-LEED and many of its applications is given in reference [13]. The SPA-LEED instrument basically consists of a fine focus electron gun, an octopole deflection unit, an entrance lense and a single electron detector (channeltron) with a small aperture. A sketch of the setup is shown in Fig. 2.2. By using a channeltron detector it is not possible to record the LEED pattern in one shot, as in the conventional LEED unit. Instead it is recorded by scanning the reciprocal space. Therefore the octopole deflection plates are used to continuously vary the angle of incidence of the electrons while the beam position on the sample is kept constant. The channeltron detector, which is located close to the electron gun, records electrons whose path is almost the reversed path of the incident ones. During scanning, the angle of incidence and the exit angle, under which electrons are detected, change simultaneously, so that the angle between initial and final scattering vector stays constant at 8° . In an Ewald construction, this scanning mode results in a rotation of the Ewald sphere around the $(0,0)$ spot in reciprocal space as shown in Fig. 2.1 b). The recorded pattern thus represents a sphere ('modified Ewald sphere') with origin at $(0,0)$ and twice the diameter of the Ewald sphere.

Major advantages of SPA-LEED over the normal LEED system are

- better resolution in k -space ($\Delta k = 0.01 \text{ \AA}^{-1}$ in our measurements),
- lower electron beam intensity (only 0.1–10 nA are necessary because of the sensitive channeltron detector) and therefore less beam damage, which is a serious issue for organic layers,
- the simple fact, that the electron gun is not blocking the view on the LEED pattern.

The high resolution allows, e.g., a quantitative analysis of spot profiles, after which the instrument was originally named.

LEED spots are always instrumentally broadened, which limits the resolution. Furthermore, the average domain size or terrace width leads to an additional

2 Experimental methods

broadening. This is described by the transfer width T , which is defined as the width on the sample that causes the same spot broadening with a perfect electron gun as the actual electron gun causes on a perfect surface. Essentially, the transfer width can be interpreted as the maximum distance on the surface, from which electrons can interfere coherently. For the SPA-LEED instrument used in this work, a value of $T = 1138 \text{ \AA}$ was specified on an almost perfect silicon surface. On less perfect surfaces, the spot broadening due to the instrumental limitations is negligible compared to the contribution from the finite terrace width. Hence the transfer width can be interpreted as the average terrace width of the crystal. However, metal crystals like the Ag(111) crystal investigated here show considerable mosaicity which leads to a further broadening of the LEED spots and therefore reduces the *effective* transfer width T_{eff} and limits the resolution of the experiment. The broadening due to mosaicity scales with the electron energy [13], which is one reason why SPA-LEED scans are usually performed at low energies around 30 eV. From the FWHM of the (0,0)-spot, the effective transfer width can be estimated as

$$T_{\text{eff}} = \frac{2\pi}{\text{FWHM}}, \quad (2.2)$$

which typically results in $T_{\text{eff}} \approx 500 \text{ \AA}$ for our Ag(111) sample. This effective transfer width can not be easily deconvoluted into the contributions from mosaicity and terrace width. Therefore, it can only be concluded, that the average terrace width of our crystal is $\geq 500 \text{ \AA}$.

Typically, the electron beam hits an area of the order of mm^2 on the sample. Hence the LEED pattern represents a macroscopic average of the sample structure and is insensitive to local defects. Organic adsorbates often adopt a number of different rotational and mirror domains, depending on the symmetry of adsorbate and substrate and the relative positions of the according unit cells. The spot pattern will usually contain contributions from all these domains which has to be considered in the LEED modeling, done with the program *Spot-Plotter* [15]. Adsorbate structures are defined in the matrix notation by a superstructure matrix M , which relates the unit cell vectors of the adsorbate, \vec{A} and \vec{B} , to those of the substrate, \vec{a} and \vec{b} , as

$$\begin{pmatrix} \vec{A} \\ \vec{B} \end{pmatrix} = M \begin{pmatrix} \vec{a} \\ \vec{b} \end{pmatrix} = \begin{pmatrix} m_{11} & m_{12} \\ m_{21} & m_{22} \end{pmatrix} \begin{pmatrix} \vec{a} \\ \vec{b} \end{pmatrix}. \quad (2.3)$$

SPA-LEED images presented in this work are displayed by an inverted gray-scale, i.e. regions of higher (lower) intensity appear darker (brighter). To achieve a good resolution in a shorter time, only one quadrant in reciprocal space is measured in many cases, with the specular (0,0)-spot in the lower right corner, see e.g. Fig. 4.9 in chapter 4. Due to the symmetry of the pattern, this contains the same information as the complete space.

Initially, the scans are scaled in units of the deflection voltage. For calibration, a LEED pattern of a well known structure has to be measured. This calibration was done at different electron energies on the system PTCDA on Ag(111), since

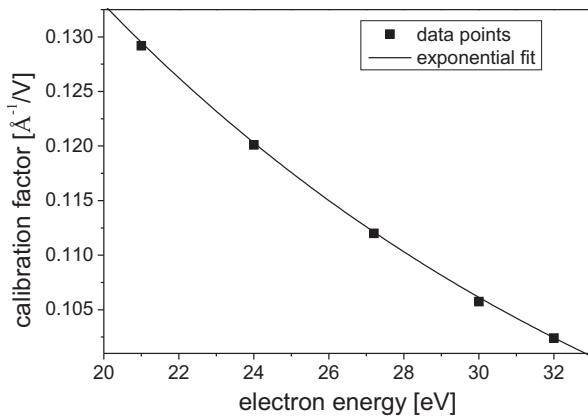


Figure 2.3: Calibration factors for SPA-LEED measurements on the Ag(111) crystal. The factors were estimated from the well known pattern of PTCDA on Ag(111).

PTCDA grows in islands of a well known, commensurate structure on this surface (cf. chapter 6). The resulting calibration factor decays exponentially with energy, as shown in Fig. 2.3.

It should be noted, that the images contain the typical SPA-LEED distortions at high k -values. The corresponding electron trajectories closely approach the octopole deflection plates of the SPA-LEED system. In this close vicinity, the electric field of the plates is not homogeneous, so that the electron paths of primary and scattered beams are differently influenced. As a consequence, the positions of the outer spots usually do not fit the positions of calculated spots from a LEED model. However, the positions of the inner spots as well as the number and qualitative arrangement of the outer spots are sufficient to find the right model.

2.2 Scanning Tunneling Microscopy

Demonstrated by Binnig and Rohrer in 1982 [16], the *Scanning Tunneling Microscope* (STM) is one of the most common members of the Scanning Probe Microscopy (SPM) family. Generally, these instruments consist of a tip that probes a local interaction with the surface of a sample. In the case of STM, a metal tip is placed in close proximity (a few Ångstroms) to a metal or semiconductor sample. A bias voltage V then induces a net tunneling current I between tip and sample. This way the two conductors, tip and sample, form a tunneling junction with vacuum as an insulating potential barrier in between. A schematical drawing of a tunneling junction is shown in Fig. 2.4. In the classically forbidden region within the barrier, the quantum mechanical wave

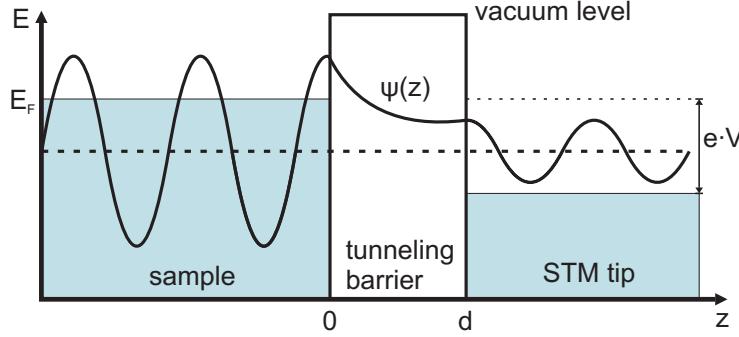


Figure 2.4: Schematic of a metal–vacuum–metal tunneling junction. The electron wave decreases exponentially within the classically forbidden potential barrier.

function $\Psi(d)$ of an electron is described by an exponential decay

$$\Psi(d) = \Psi(0) \cdot e^{-\kappa d} \quad (2.4)$$

with a decay constant κ [17] and d being the z -position in the barrier, i.e. along the surface normal. The probability to find an electron at a distance d is proportional to $|\Psi(0)|^2 \cdot e^{-2\kappa d}$, which is nonzero. Therefore an electron can cross the barrier (i.e. *tunnel*) in both directions. The applied bias voltage leads to a shift of $\Delta E = e \cdot V$ between the Fermi-levels of tip and sample, so that tunneling in one direction dominates and a net tunneling current can be measured. For achieving atomic resolution, the apex of the tip must be as small as possible, i.e. ideally a single atom. Due to the exponential decrease of the tunneling probability with increasing distance, the tunneling current changes by about one order of magnitude per Å. Therefore only the apex atom contributes significantly to I , which leads to very localized tunneling and enables high lateral resolution. The tip can be moved relative to the sample very precisely in all spatial directions by piezo electrics.

In the so-called constant current scanning mode, the topography of the sample surface can be measured by scanning the tip along the surface while keeping the measured tunneling current at a constant value (*setpoint*) by a feedback control. I can be controlled by adjusting the z position of the sample, since it depends exponentially on the distance $d = \Delta z$ between tip and sample. A constant current STM image is taken by recording the tip height as a function of lateral (x/y) position on the sample. A color code is applied to represent the different Δz values.

It is very tempting to interpret STM images as a pure geometrical topography, but the instrument actually measures something different. The tunneling current does not only depend on the distance, but also on the density of states (DOS) of the electrons in the sample and the tip. Usually, the DOS of the sample will vary as a function of x/y position, so that it is reasonable to define

2.2 Scanning Tunneling Microscopy

a local density of states (LDOS) $\rho_S(z, E)$. In the Tersoff-Hamann picture [18], the dependency of I on the LDOS at zero temperature is expressed in Eq. 2.5.

$$I \propto \sum_{E_n=E_F-eV}^{E_F} |\Psi_n(0)|^2 e^{-2\kappa d} = \rho_S(d, E_F) eV, \quad (2.5)$$

with d being the z -position of the tip surface, i.e. the tip-sample distance. Applying a specific bias voltage V between tip and sample, all electrons in states with energy levels E_n between the Fermi-level E_F and $E_F - e \cdot V$ are able to tunnel from tip to sample (or vice versa, depending on the sign of the bias voltage) and thus contribute to I . In other words, the tunneling current depends on the spatial distribution of the DOS, integrated over the electronic states in an energy range defined by the applied bias voltage. Therefore, any STM image represents a mixture of geometric and electronic structure of the surface, namely a contour of a constant Fermi-level LDOS of the sample. Certain adsorbate atoms or small molecules like He, O or CO can even make a negative contribution to the Fermi-level LDOS, causing them to appear like holes in a topographic image.

However, the states of the STM tip ρ_T play an equally important role for the tunneling, as $I \propto \rho_S \cdot \rho_T$. The tip contribution is e.g. necessary to understand, how atomic resolution is achieved in STM. A perturbative approach which treats sample and tip as isolated systems was developed by Bardeen [19]. Electronic states can be delocalized on a surface, which limits the achievable STM resolution. It was found that the high lateral resolution of the technique can be explained if the dominant contribution to the tunneling current stems from a d_z -like or p_z -like state near the Fermi-level, protruding from the apex atom of the tip. The tunneling current is then determined by a convolution of the tip state and the sample states. Bulk states or surface states [20, 21], which exist at energy levels in the gap of the bulk energy bands, may dominate the tunneling process, depending on the material. In general, tip states have a strong effect on atomic-size features, while STM images of large structures are essentially independent of them. In the latter case, the s-wave approximation by Tersoff and Hamann for the orbital of the tip apex atom is valid.

Establishing a quantitative description of the tunneling problem, the situation becomes more complicated due to interactions between tip and sample at small distances. The wave function of one part (tip or sample) is modified by the existence of the other. Also, forces between tip and sample occur, which can be repulsive or attractive, depending on the distance regime. The according corrections are established by perturbation theory in the *Modified Bardeen Approach* (MBA). A more detailed overview about the theory behind STM imaging can be found in literature, e.g. in reference [17].

The effect of forces in STM was recently used to achieve ultrahigh geometric resolution by introducing small molecules into the STM junction [22, 23, 24]. These molecules act as force sensors, sensing the Pauli repulsion from the total electron density of the surface and transduce this signal into a tunneling conductance change. The technique was called *Scanning tunneling hydrogen*

2 Experimental methods

microscopy (STHM), since it was first discovered using H₂ molecules [25].

In the case of organic semiconductor molecules adsorbed on a surface, the electronic states in the adsorbate are found at discrete energies (molecular orbitals). Depending on the voltage sign, electrons tunneling from occupied states or tunneling into unoccupied states of the adsorbate contribute to the STM contrast, respectively. Therefore, the geometrical distribution of all molecular orbitals contributing to the tunneling current at a specific bias voltage will influence the measured STM contrast. However the orbitals that are closest to the Fermi-level, HOMO and LUMO, clearly dominate this contribution.

STM images shown in this work have been measured in constant current mode, either with a liquid helium cooled Createc STM, operating at ≈ 5 K, or with an Omicron STM operating at RT and at a temperature of approx. 110 K, achieved by liquid nitrogen cooling. All STM images were processed with the WSXM program [26] in terms of background subtraction and optimizing contrast display, but not further filtered. However, when STM images are taken at RT and at liquid nitrogen temperature, a considerable drift due to thermal motion can usually be found in the images. In some cases (when mentioned), this drift was corrected using the program Gwyddion [27].

2.3 X-ray Standing Waves

X-ray Standing Waves (XSW) is an experimental technique capable of measuring adsorption heights of adsorbate films on crystalline substrates [28]. The basics of the technique will be summarized in the following, while a more detailed review can be found, e.g., in reference [29].

In an XSW experiment, a monochromatic photon beam is directed onto a single crystalline sample, whereby the energy of the incoming wave is chosen to fulfill the condition for a $H = (hkl)$ Bragg reflection. Therefore, photons with energies in the X-ray regime are necessary. In this work, we are interested in XSW on a Ag(111) crystal, for which the (111) Bragg condition of the Ag lattice must be fulfilled. A part of the wave is reflected at the (111) lattice planes in this case and forms a standing wave by interfering with the incident wave. This standing wave field extends also in a region above the sample surface and has a periodicity equal to the spacing of the lattice planes of the Bragg reflection d_{111} . Since the Bragg condition is in reality not sharply defined, as is assumed in the kinematic theory, reflected intensity can be measured in a certain small energy range around E_{Bragg} . Upon scanning the photon energy through the Bragg condition, a reflectivity profile is measured as exemplarily shown in the upper part of Fig. 2.5. The profile is asymmetric due to the photon absorption in the crystal. During the photon energy scan, the phase Φ of the standing wave changes by half of a wavelength, i.e. by π . At the onset of the Bragg condition, the Ag atoms lie on a minimum of the XSW field. Scanning through the Bragg energy, the maximum of the XSW field shifts towards the atoms so that these absorb a part of the photons, and the reflectivity decreases. The full width at

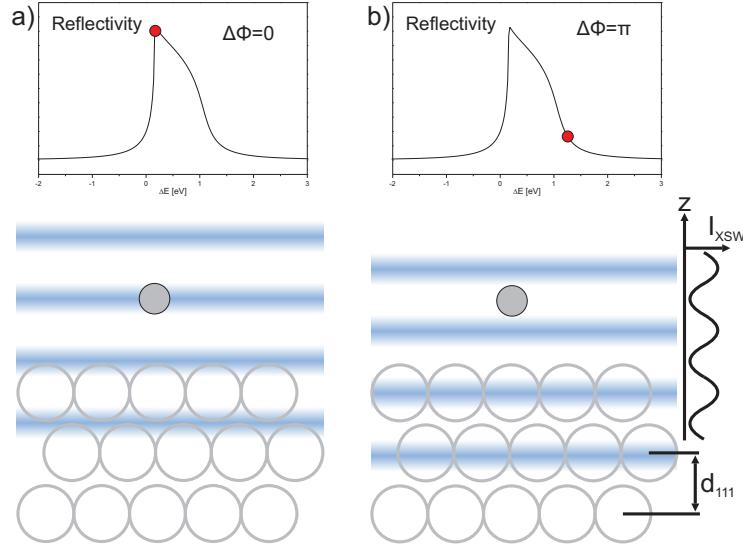


Figure 2.5: Principle of the XSW experiment. During the scan through the Bragg condition from a) to b), the phase of the standing wave shifts by π . Substrate and adsorbate atoms experience changing X-ray intensities depending on their position in the wave field.

half maximum of the reflectivity curve depends on the Bragg angle and is largest for 90° . Here, the reflection width seen in an experiment is often dominated by the intrinsic width of the Bragg reflection, not by the mosaicity of the sample. This is the main advantage of the *Normal Incidence XSW* (NIXSW) variant, which is used in this work.

The fact that the absorption of any bulk or surface atom depends on the phase shift of the standing wave can be used to extract informations about the adsorption height of adsorbate atoms or molecules on the surface. An adsorbate atom, that lies e.g. on an intensity maximum at the onset of the Bragg condition (see Fig. 2.5), will lie on a minimum at the end. Atoms on other adsorption heights will lie on maxima and minima at different energies, accordingly. Since the absorption of photons by the adsorbate atoms is proportional to the intensity of the standing wave I_{XSW} , the shape of an absorption vs E curve contains information about the adsorption height.

Experimentally, absorption curves are determined by measuring secondary signals like electrons, emitted due to the photoelectric effect. In this case, the absorption curve consists of the integrated *X-ray Photoelectron Spectroscopy* (XPS) intensity of a specific atomic species after background subtraction, i.e. the partial photoelectron yield Y , measured at different beam energies around E_{Bragg} . It will therefore be called (photo-)electron yield curve in the following.

Because of the different, well known binding energies of most atomic species, the technique is element specific. Therefore, the adsorption heights of different atomic species within an adsorbate molecule can be separately evaluated by measuring and integrating only the desired part of the photoelectron spectrum. This allows conclusions about a possible tilt or bending of a large molecule. However, one challenge is to separate the XPS signal of the adsorbate from contributions of satellites or surface plasmons, i.e. to find the best model for fitting the XPS data. In many cases even signals from the same atomic species can be separated, if the atoms have different chemical environments. Chemical bonds to different bonding partners typically lead to slightly different shifts of the core levels of an atom. A well known example is the case of PTCDA on the noble metal surface Ag(111), where carboxylic oxygens and anhydride oxygens could be analyzed separately [30].

Results of an XSW analysis

The electron yield curves obtained experimentally are fitted by the function

$$Y = 1 + R(\Delta E) + 2\sqrt{R(\Delta E)}F^H \cos(\Phi(\Delta E) - 2\pi P^H), \quad (2.6)$$

where R is the reflectivity, $\Delta E = E - E_{Bragg}$ is the energy difference to the Bragg energy and Φ is the phase shift of the wave field. Y is the (electron) yield, normalized to the intensity of the incident wave. Due to the interference of two beams (incident and reflected), the normalized electron yield can adopt amplitudes between $(1 \pm 1)^2$, i.e. 0 to 4. Formula 2.6 contains the two fitting parameters F^H and P^H , whose values range from 0 and 1.

- The *coherent position* P^H represents the average vertical position of the atomic species relative to the nearest Bragg plane. From this parameter, the adsorption height d^H can easily be calculated in many cases. However since e.g. two atoms sitting on different maxima of the standing wave field show the same adsorption signal, the result is sometimes ambiguous. Strictly speaking, P^H corresponds to all adsorption heights

$$d^H = P^H \cdot d_{\text{crystal}} + N \cdot d_{\text{crystal}} \quad (2.7)$$

with N being a natural number. Adsorption heights can still be specified in most cases, since typically only one of the possible values is physically reasonable. It should be noted, that the coherent position is related to the bulk lattice planes. The adsorption heights calculated from this, do not take adsorbate induced relaxations of the surface atoms into account. However, for organic molecules on Ag(111), such relaxations are typically negligible.

- F^H is an ordering parameter called *coherent fraction* and describes, how narrow the distribution of adsorption heights is. If all atoms of one species are on perfectly the same adsorption height d^H , F^H would be 1. A value of 0 on the other hand corresponds to complete disorder of adsorption heights. In reality, the coherent fraction will never be 1, but always be

decreased by e.g. the mosaicity of the crystal and thermal vibrations. A low coherent fraction can also result from multiple adsorption sites or of a tilt or bending of the adsorbate molecules.

The results of the XSW analysis are often plotted in a polar diagram, called *Argand diagram*, as vectors with a length of F^H and an angle of $2\pi P^H$ in radians. If the electron yield curve contains contributions from more than one prominent coherent position of the atomic species, the vector in the Argand diagram is given by the sum of the vectors of the single components (F_j^H, P_j^H) as

$$F_{total}^H \cdot \exp(2\pi i P_{total}^H) = \sum_j F_j^H \cdot \exp(2\pi i P_j^H). \quad (2.8)$$

Under special circumstances, this can be used to deconvolute a signal into its single components by a vector analysis, as will be shown in chapter 5.2.

The photoelectron yield is only proportional to the absorption yield if the dipole approximation for the angular distribution of the photoemission is valid. This is usually not the case for high photon energies as used here, so that quadrupole corrections to the electron yield equation would be necessary. However, it was shown that for a measuring geometry with an angle of 90° between the incident beam and the analyzer, multipole corrections can be neglected [31], so that Eq. 2.6 is valid.

Usually, XSW measurements are performed on (sub-)monolayer films, since molecules in different layers make the result impossible to interpret due to too many different adsorption heights. However, in case of only two layers, and if the coverage of molecules in the 2nd layer is known, the resulting coherent position can be interpreted. An analysis of stacked *hetero-organic* layers is possible, if the two types of molecules do not intermix and if they contain different atomic species. This will be shown for the system F₁₆CuPc on CuPc/Ag(111) discussed in chapter 5.2.

2.4 Pair potential calculations

Pair potential (or force field) calculations are a method for modeling intermolecular interactions. They will be used to explain the structure formation in organic thin films in many places throughout this work. The calculations are performed in a way introduced by Ingo Kröger et al. [32, 33] and by using a program developed by Benjamin Stadtmüller. The basics of the method will be explained in the following.

The pair potential Φ between a pair of molecules is defined as the sum of the interactions of all atoms i of molecule A with all atoms j of molecule B.

$$\Phi = \sum_i \sum_j (\varphi_{ij}^{vdW} + \varphi_{ij}^{El}) \quad (2.9)$$

For simplicity, we only take electrostatic potentials φ_{ij}^{El} and van-der-Waals (vdW) potentials φ_{ij}^{vdW} into account. The electrostatic potentials are given

2 Experimental methods

by the Coulomb potential between the partial charges Z_i and Z_j of the atoms as

$$\varphi_{ij}^{El} = \frac{Z_i Z_j}{4\pi\epsilon_0 r_{ij}}, \quad (2.10)$$

with the vacuum permittivity ϵ_0 and the distance r_{ij} between the atoms. To obtain these partial charges, a Natural Bonding Orbitals (NBO) [34] population analysis was done. The charges as well as the interatomic distances within the molecule were taken from DFT calculations using the Gaussian program [35] with the B3LYP functional and LANL2DZ basis set. These DFT calculations are performed for free molecules without considering interactions to other molecules or a substrate. Vertical distortions of the molecular geometry upon adsorption can be taken into account for the pair potential calculations, if according experimental data, e.g. from XSW, is available. Lateral distortions are usually not precisely known. However, for the π -conjugated molecule PTCDA on Ag(111) it was calculated that the lateral distortion upon adsorption is very small [36].

The vdW potential between atom i and atom j is calculated by

$$\varphi_{ij}^{vdW} = a_{ij} \cdot \exp(-b_{ij}r_{ij}) - c_{ij}/r_{ij}^6. \quad (2.11)$$

The first, exponential part describes the Pauli repulsion while the second part is an attractive London force for which 6-exp functions are used. φ_{ij}^{vdW} contains the three element specific non-bonding parameters a_{ij} , b_{ij} and c_{ij} . Parameters $b = b_{ii}$ and $c = c_{ii}$ for pairs of equal atoms were found in literature for H, C, N, O, F and Cu [37, 38, 39]. For Sn, b was taken from Scott et al. [38], while c was calculated via the Slater-Kirkwood equation 2.12

$$c_{ij}[\text{Hartree} \cdot a_0^6] = \frac{3}{2} \cdot \frac{\alpha_i \alpha_j}{\sqrt{\frac{\alpha_i}{N_{\text{eff},i}}} + \sqrt{\frac{\alpha_j}{N_{\text{eff},j}}}}. \quad (2.12)$$

Therefore, values for the effective number of electrons N_{eff} in the outer shell and for the atomic polarizability α were also taken from literature [38, 40].

The parameter a was determined for F and Sn in the same fashion as done by Kröger et al. [32, 33]. Its value was chosen so that the van-der-Waals potential (2.11) has its minimum at a distance R equal to the known sum of the van-der-Waals radii [41] of the atom pair. Resulting potential curves are shown in Fig. 2.6. For F and Sn values of $a = 2620$ eV and $a = 920$ eV are obtained, respectively. Parameters for the other elements were taken from Kröger et al [32]. All vdW parameters used in this work are summarized in Table 2.1. In case of potentials between different atomic species, the geometric means of the corresponding vdW parameters are used.

The pair potential calculations, as presented here, are of cause an oversimplification of the real physical situation. Only electrostatic and van-der-Waals interactions are taken into account. Interesting for this study is the situation when the molecules are adsorbed on a surface. Interactions between adsorbate and substrate like charge transfer are not accounted for. This means that in

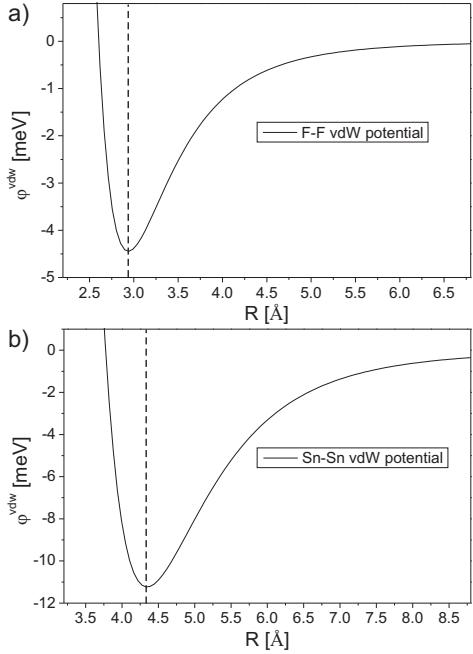


Figure 2.6: Van-der-Waals potentials for a) a pair of F atoms, and b) a pair of Sn atoms. The vdW parameter a is chosen so that the minimum matches the sum of van-der-Waals radii, indicated by the vertical slashed lines.

general, the pair potential calculations are the better, the weaker the interaction with the surface is. It has been shown, that the pair potentials describe the structure formation of physisorbed systems like phthalocyanines on Au(111) very well [32]. On a strongly interacting surface like Cu(111), the results will usually differ considerably from experimentally found structures. In this work, measurements were performed mostly on the Ag(111) surface, which is an intermediate situation between Au(111) and Cu(111). Phthalocyanines typically show weak chemisorption on this surface, which means that charge transfer between the molecules and the substrate is present. This has to be considered when correlating the calculation results to experimental findings.

More detailed theoretical considerations would require sophisticated *ab initio* calculations, which are not done in the context of this work.

element	$a[\text{eV}]$	$b[\text{\AA}^{-1}]$	$c[\text{eV}\cdot\text{\AA}^6]$
H	432 [39]	4.52 [39]	1.96 [39]
C	34000 [32]	4.59 [39]	15.7 [39]
N	9000 [32]	4.59 [38]	12.7 [32]
F	2620	4.6 [38]	5.135 [38, 40]
Cu	550 [32]	2.95 [38]	94.93 [32]
Sn	920	2.57 [38]	163.1 [38, 40]

Table 2.1: List of van-der-Waals coefficients for pairs of equal elements used in the pair potential calculations

2.5 Sample details and preparation

Measurements described in this work were mainly done on the (111) surface of an fcc Ag crystal. The unit cell vectors of this surface have a length of $|\vec{a}| = |\vec{b}| = a_{\text{bulk}}/\sqrt{2} = 2.889 \text{ \AA}$ and include an angle of 120° in real space, as sketched in Fig. 2.7 a). Three layers of a Ag(111) crystal are shown in topview

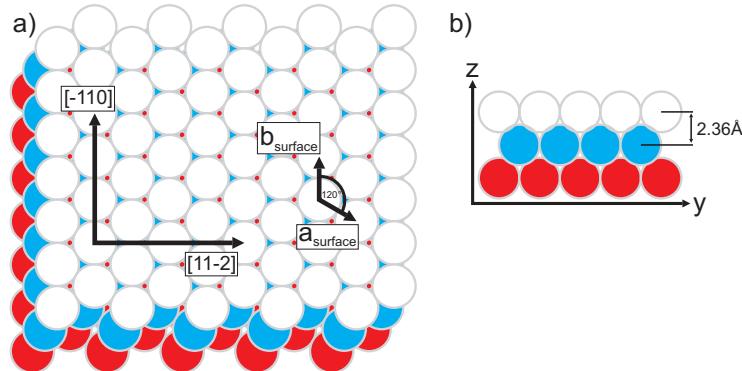


Figure 2.7: Ag(111) surface: a) Topview, showing the surface unit cell vectors and high symmetry directions. b) Sideview showing the layer distance

and sideview. The lateral high symmetry directions, expressed in bulk units, are $\langle 01\bar{1} \rangle$, which is along the connection between two nearest neighbors in the surface plane, and $\langle \bar{2}11 \rangle$ in the perpendicular direction. Orientations of unit cells and molecules will always be related to these directions throughout this work. In reciprocal space, distances are given in units of $[\text{\AA}^{-1}]$ or in percentages of the surface Brillouin Zone (BZ), whereby $2.175 \text{ \AA}^{-1} = 100\% \text{ BZ}$ for Ag(111). For XSW, the distance of the Bragg planes is of interest. In our case, this is the layer distance in $z=(111)$ direction, which is $d_{111} = \frac{1}{3}\sqrt{3} \cdot a_{\text{bulk}} = 2.36 \text{ \AA}$.

Preparation method

Before each experiment, a clean and smooth surface was prepared by a standard sputtering and annealing procedure. For sputtering, the sample was bombarded with Ar^+ ions to remove several layers of the sample surface, including contaminations. Afterwards the now rather rough surface was annealed at $T \geq 723$ K. Multiple cycles of this procedure result in a clean (111) surface with a large average terrace width, as can easily be judged by checking the specular spot and the 1st order silver spots in LEED.

The UHV chamber used for the SPA-LEED measurements had a base pressure of $\approx 3 \cdot 10^{-10}$ mbar, enabling the surface to stay clean for a sufficient amount of time after preparation.

On the freshly prepared sample, organic molecules were deposited by Organic Molecular Beam Epitaxy (OMBE) from a home built Knudsen cell. With a Quadrupole Mass Spectrometer (QMS), the Ion Current (IC) signal of a typical fragment of the according type of molecule was monitored during deposition. The integrated IC is taken as a measure for the deposited amount of molecules, which enables good control over the growth of specific, desired adsorbate coverages. Short 2D SPA-LEED scans were also recorded in-situ during deposition, when necessary.

Coverages of the organic adsorbates are given in fractions of a monolayer (ML) in this work. It should be noted, that a coverage of one monolayer corresponds to the maximum amount of adsorbate molecules in the first layer on the surface, i.e. to closest molecular packing. This definition is different from the classical definition of one monolayer being equal to one adsorbate molecule per surface atom. However, this is much more practical for (large) organic adsorbates.

3 SnPc on Ag(111)

Phthalocyanines are a family of large, π -conjugated organic molecules, consisting of four phenyl rings attached to a tetra-aza-porphyrin ring, with a molecular formula of $C_{32}H_{16}N_8R$. The center of the aza-porphyrin ring is occupied by a metal atom or a functional group (R), influencing the symmetry and the properties of the molecule. In the case of tin(II)-phthalocyanine (SnPc), the center contains a tin atom, which sticks out of the molecular frame due to its large diameter. Therefore the molecule is non-planar, so that it exhibits a permanent vertical dipole moment. Its structure, calculated from DFT, is shown in Fig. 3.1 b) in topview and sideview.

In this chapter, the adsorption of SnPc on the Ag(111) surface will be discussed in detail. A short introduction into the system will be given, focusing on the results of previous SPA-LEED [8, 9] and XSW [42] investigations. Afterwards, STM and STS measurements on SnPc structures in different surface phases are shown and analyzed. Finally, pair potential calculations have been performed to model the intermolecular interactions. It will be shown, that the measured molecular arrangements can widely be explained in the context of intermolecular potentials.

Structural phase diagram

On the Ag(111) surface, a number of different phases occur for different temperatures and (submonolayer) SnPc coverages, as was previously investigated by SPA-LEED [8, 9]. These results are summarized in the structural phase diagram in Fig. 3.1 a), showing phase boundaries and exemplary SPA-LEED images.

At room temperature, two rings of diffuse scattering intensity are visible in the LEED pattern around the (0,0)-spot for low sub-ML coverages. The outer ring is rather weak and does not change in size during further deposition. In contrast, the radius of the inner ring increases with coverage. The diffuse inner ring indicates that the molecules are disordered with respect to their orientation and the direction to their neighbors, but they adopt a preferred intermolecular distance. The increasing ring radius in k -space corresponds to a decreasing intermolecular distance. This can be interpreted as repulsion between the SnPc molecules or simply as an entropy effect, since a disordered phase has higher entropy than a phase with ordered island growth. Since the molecules essentially behave like a 2D-gas, this phase was named *gas-like phase* (g-phase). Once a critical coverage of 0.9 monolayers (ML) is exceeded, the molecules are sterically forced to arrange into an ordered structure. Upon increasing the coverage up

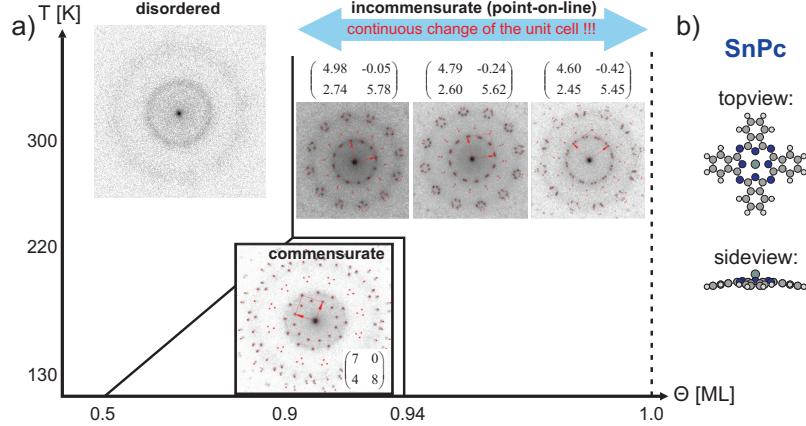


Figure 3.1: a) The structural phase diagram of SnPc on Ag(111) after SPA-LEED measurements from Stadler et al. [8, 9]: At RT, a ring structure occurs until a coverage of 0.9 ML is reached. Incommensurate phases with a continuously shrinking unit cell appear between 0.9 ML and 1 ML. At LT, a commensurate phase exists over a certain coverage region. b) The structure of the molecule as calculated from DFT is shown in topview and sideview, respectively.

to a complete monolayer, the adsorbate structure changes continuously. The unit cell is shrinking in such a way, that the molecules always maximize the distance to their neighbors. Thereby, the unit cell vectors move along lines of the substrate lattice. The registry with the substrate is therefore described by point-on-line (p.o.l.) [43] coincidence for this series of unit cells. Since the entropy argument is not valid for this long-range ordered phase, intermolecular repulsion must be the origin of this behavior.

Cooling the sample to temperatures below 220 K changes the structure formation considerably in a certain coverage range. For submonolayer coverages of at least ≈ 0.5 ML, the molecules form an ordered structure at LT with a commensurate unit cell that does not change up to 0.94 ML coverage (c-phase). This behavior can be attributed to 2-dimensional island formation, for which an overall attractive lateral intermolecular interaction is required. The size of the unit cell suggests that it now contains two non-equivalent molecules. Due to its non-planar geometry, SnPc can in principal adsorb in two non-equivalent ways on a surface. The central Sn atom can point either towards ("Sn-down") or away from ("Sn-up") the surface. The differently adsorbed molecules can easily be distinguished in STM by their center appearing as a bright protrusion for Sn-up or as a dark hole for Sn-down molecules, respectively, as was first shown by Lackinger et al. [44]. The occurrence of these two conformations was confirmed by XSW [42]. Considering this geometrical structure, it was further interpreted that one of the molecules in the c-phase unit cell is Sn-up and the

3.1 Scanning tunneling microscopy

other Sn-down. Above 0.94 ML, no phase transition is observed upon cooling, so that the p.o.l.-structure remains. Our interpretation is that the optimum adsorption geometry in the commensurate phase corresponds to a *local* coverage of 0.94 ML within the islands. When the *total* coverage rises above 0.94 ML, the molecules cannot adopt their favored, commensurate structure anymore and form a more densely packed, incommensurate structure.

This complex phase diagram is the result of the weak chemisorptive binding of SnPc to the Ag(111) surface. Since intermolecular interactions and molecule–substrate interactions are in the same order of magnitude, the fine balance of the different forces leads to the formation of many different structures for different values of the external parameters temperature and coverage. A very similar structural phase diagram was also obtained for CuPc on Ag(111) [45]. On the weaker interacting substrate Au(111) and the stronger interacting Cu(111) on the other hand, the resulting phase diagrams for CuPc are less complex [46].

The mere arrangement of LEED spots reveals the size and shape of a unit cell, but it does not contain information about the positions and orientations of the molecules inside the unit cell. For this purpose, the spot intensities would have to be analyzed in the framework of dynamical diffraction theory, as it is done in LEED-IV. However, such an analysis is difficult and was only performed very seldomly on organic adsorbate systems, e.g. on deuterated benzene (C_6D_6) on Ru(0001) [47] or on C_{60} /Cu(111) [48].

A real space imaging technique with sufficient resolution, like STM, is therefore necessary to complement the SPA-LEED measurements. The following section describes STM measurements that have been recorded in the context of this work for a number of different coverages and temperatures, covering all regions of the previously described structural phase diagram. The measurements in the first subsection were performed on the dilute g-phase at ≈ 5 K. In the following subsections, measurements on the commensurate LT phase and the p.o.l.-phase are reported. These were recorded at RT or temperatures of approx. 110 K, achieved by liquid nitrogen cooling.

3.1 Scanning tunneling microscopy

3.1.1 Disordered phase at low coverages

For low submonolayer coverages, SnPc molecules are free to move almost unhindered by each other on the Ag(111) surface. This is, e.g., indicated by the change of the average intermolecular distance as a function of coverage, as seen from the increase of the ring radius in LEED. Therefore, the disordered surface phase is 2D-gas-like and not a liquid phase, in which the molecules would arrange in more densely packed islands without long range order [49]. The diluted phase will be referred to as g-phase in the following. At room temperature, STM measurements are not possible in this phase because of the high mobility of the molecules due to their thermal energy. Cooling the sample down to

low cryogenic temperatures around 5 K reduces this mobility so far, that stable measurements are possible.

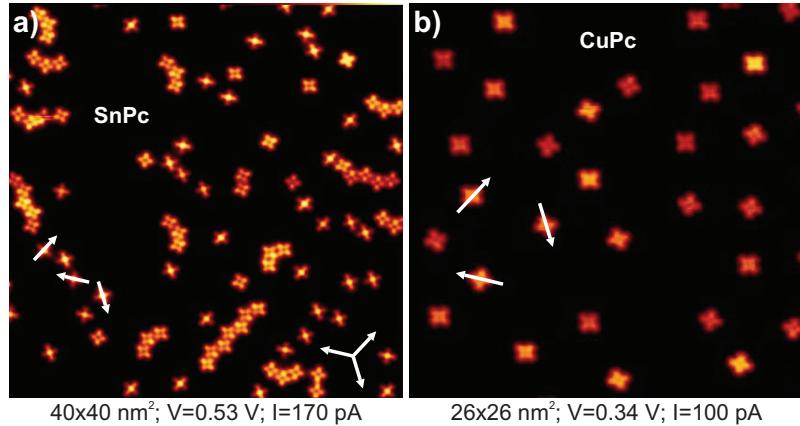


Figure 3.2: a) STM image of a low SnPc coverage on Ag(111) showing chains of Sn-down and isolated Sn-up molecules; b) CuPc on Ag(111) shows no chain formation at all (courtesy of G. Kichin). High symmetry substrate directions are marked by the white arrows in both images.

Figure 3.2 a) shows an STM image of SnPc molecules adsorbed on a single plain terrace of a Ag(111) crystal. As can be seen at first sight, the molecules are flat lying and appear in a cloverleaf-like shape, which is the typical STM contrast of phthalocyanines due to the four phenyl rings ("wings" of the molecule). The center of the molecules is either bright or dark, which is interpreted as adsorption in Sn-up or Sn-down geometry, respectively. Counting Sn-up and Sn-down molecules in different STM images reveals a stoichiometric ratio of $\approx 1:1$ between the two geometries. The SnPc coverage Θ can be determined from counting the molecules in STM images of known size to estimate the density ρ of molecules per area. Thereby the size A of one molecule is equal to the size of the unit cell for 1 ML coverage. This estimation leads to an average value of $\Theta = A \cdot \rho \approx 189 \text{ \AA}^2 \cdot 6.3 \cdot 10^{-4}/\text{\AA}^2 = 0.12 \text{ ML}$ in our preparation.

All molecules are oriented in the surface plane so that the molecular axis through one pair of opposite wings is aligned along one of the high symmetry substrate directions. Therefore only three stable molecular orientations exist, as can also be demonstrated by manipulating single molecules with the STM tip like in Fig. 3.3. Three subsequently recorded images of the same molecule are shown. By simply scanning over the molecule with a high current setpoint of 450 pA, an in-plane rotation could be induced in between the images. Only multiples of 30° occurred, so that one wing pair was always aligned with the atomic rows of the substrate. The different contrast of the molecule is due to different registries of the molecular wings with the substrate in the different images.

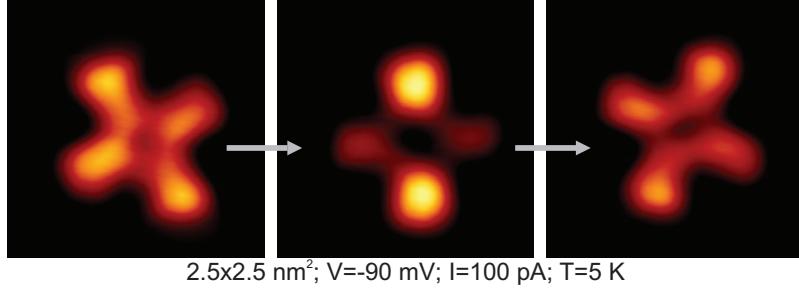


Figure 3.3: Manipulation of a single SnPc molecule: Scanning with a high current setpoint, as done in between the images, often results in an in-plane rotation of the molecule by a multiple of 30°.

Symmetry breaking

A striking observation, is that the Sn-up molecules are usually isolated from other molecules, while the Sn-down species tend to form close packed chains, see Fig. 3.2 a). The molecules within these chains are equally oriented with the molecular centers shifting in a zig-zag-like fashion around the chain axis. The chain axes are also aligned along the high symmetry Ag(111) directions. This behavior is in contrast to that of CuPc on Ag(111), shown in Fig. 3.2 b), which shows no signs of chain formation. On the other hand, CuPc molecules form chains when adsorbed on the stronger interacting Cu(111) surface, as shown by Karacuban et al. [50]. Hence the Sn-down molecules behave similar to CuPc/Cu(111), while the Sn-up molecules rather resemble the CuPc/Cu(111) case. In the following, we want to understand this different behavior.

For CuPc on Cu(111), a strong charge transfer between adsorbate and substrate was found [46]. This charge transfer lifts the degeneracy of the two LUMOs by filling one of these orbitals, which reduces the symmetry of the molecules from four-fold to two-fold. Hence a quadrupole moment is induced, so that the interaction of the molecules with their nearest neighbors is changed. For CuPc on Ag(111), such an effect was not found. The difference can be related to the strength of the substrate–adsorbate interaction, which is larger on the Cu(111) surface.

We can argue similarly for the SnPc/Ag(111) system. For Sn-down molecules, the adsorption height of the Sn atoms was found to be $\approx 2.3 \text{ \AA}$ in all phases by XSW [9]. Therefore a strong overlap of the wavefunction of the central Sn atom with the Ag substrate states can be presumed, leading to considerable charge transfer. Due to the different symmetries of substrate and adsorbate (six-fold vs. four-fold), only one wing pair can be well aligned with a high symmetry silver direction so that the two wing pairs can not have the same registry with the Ag lattice. This causes differences in the charge transfer between the surface and the wing pairs and therefore leads to a symmetry breaking of the molecules from four-fold to two-fold, which manifests itself in a different STM contrast

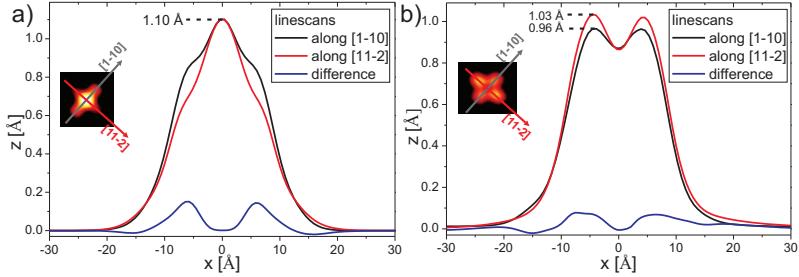


Figure 3.4: Profiles of a) Sn-up and b) Sn-down molecules, measured along $[1\bar{1}0]$ and $[11\bar{2}]$, respectively. Averaged curves of several linescans are shown. ($V = 0.53$ V, $I = 170$ pA)

of the opposing pairs of wings. To quantify this, average linescans across SnPc molecules are shown in Fig. 3.4, recorded along $[1\bar{1}0]$ and $[11\bar{2}]$, respectively. These scans have been performed at positive bias, showing empty states. Similar contrasts have been observed in filled state STM images as well, however imaging empty states was found to be generally more stable. Note that the apparent height of the SnPc molecules of ≈ 1 Å is rather small. However, since the STM contrast is a convolution of electronic and geometric structure, this does not represent the real geometrical height. The calibration of the z -piezo crystal was done in a standard procedure by checking steps between adjacent Ag terraces, which should be 2.36 Å high. For both Sn-up and Sn-down, the two scan directions yield different profiles. For the Sn-down molecules, the wings that are aligned along $[11\bar{2}]$ show a slightly larger apparent height in Fig. 3.4 b) than those aligned along $[1\bar{1}0]$. This resembles the two-fold symmetric contrast of CuPc on the strongly interacting Cu(111) surface [50]. In the Sn-up configuration, the Sn orbital overlap with the substrate is much smaller. Consequently, charge transfer should be less effective. In the linescan in Fig. 3.4 a), a symmetry breaking is also clearly visible, however. Comparing the difference spectra, it can be seen that the apparent height difference between the wing pairs appears equally strong for Sn-up and Sn-down molecules to our surprise. However, the fact that only the Sn-down molecules form chains still indicates that their intermolecular attraction must be stronger than for Sn-up. The absolute values of the apparent height are slightly smaller for the Sn-up wings than for the Sn-down wings. It could be speculated that this absolute apparent height difference is related to the electronic structure. Differences in the LDOS could cause a weaker attractive intermolecular interaction of Sn-up due to a smaller quadrupole moment. This might cause the Sn-up molecules to behave similar to CuPc on weaker interacting surfaces instead of clustering to chains like the Sn-down molecules.

Another interesting observation is that for Sn-up the wing pair along $[1\bar{1}0]$ appears higher, while for Sn-down it appears lower than the pair along $[11\bar{2}]$. This could be an indication for different adsorption sites of Sn-up and Sn-down, which

3.1 Scanning tunneling microscopy

would result in different registries of the wings with the substrate. A similar observation was made by Wang et al. [51]. By comparing STM measurements and calculations, the authors proposed that Sn-up is probably adsorbed with the Sn atom on top of a silver atom, while in Sn-down, the Sn atom occupies a bridge position. However, in a different calculation, Baran et al. [52] found the fcc and hcp hollows to be preferred adsorption sites for the Sn atoms. Thus, the SnPc adsorption sites on the Ag(111) surface are still not unambiguously determined.

Switching of SnPc molecules

The capacity of STM for manipulation of single SnPc molecules can be seen from the difference between Fig. 3.5 a) and b). Two closeups of a Sn-down

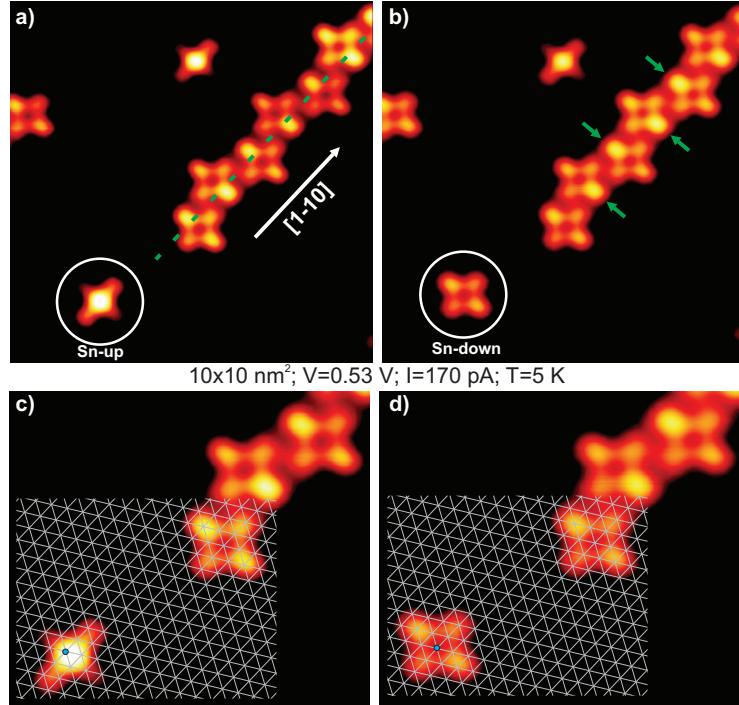


Figure 3.5: Closeup of a Sn-down chain surrounded by some single molecules. Especially bright molecular wings in the chain are marked by the green arrows. The switching possibility from a Sn-up molecule in a) to Sn-down in b) is demonstrated. The adsorption site of the molecule in the lower left changes during the switching, as shown by the blue circles in c) and d), which mark the same lattice point.

chain surrounded by some single molecules are shown. Between recording the

two images, a voltage pulse of -2 V has been applied to the center of the Sn-up molecule, which is marked by the white circle, with the STM tip. The effect was a switching of the conformation from Sn-up to Sn-down. The value of the applied pulse is in good agreement with the threshold of -1.9 V reported earlier for this switching process [53]. It can also be induced for molecules located within the commensurate islands discussed in the next section and is in general irreversible for molecules adsorbed in the first molecular layer. The irreversibility shows that the Sn-down state is a more stable configuration regarding interactions with the substrate. On the other hand, switching of molecules adsorbed in the 2nd layer *is* reversible, which further indicates the strong influence of the substrate. The switching mechanism has been explained by a transient oxidization of the central Sn atom from Sn^{2+} to the smaller Sn^{3+} which can travel through the molecular frame more easily. A similar switching process was also found on a graphite surface for chloraluminum phthalocyanine (ClAlPc) from a Cl-up to a Cl-down conformation [54]. On this weakly interacting surface the switching is reversible in the 1st layer. The switching process for different phthalocyanines has been investigated in more detail by Baran and Larsson [55].

Despite the higher stability of Sn-down, equal fractions of molecules were found in the Sn-up and Sn-down configuration at LT, as mentioned above. XSW measurements suggested, that both configurations also occur at RT in the g-phase [9]. For the conformational change to the more stable Sn-down configuration, an energy barrier has to be overcome, for which the thermal energy of the molecules is obviously not sufficient. Therefore the molecules stick like they hit the surface regarding their configuration.

Interestingly for Sn-down molecules in the middle of a chain, *one* especially bright wing is found, as indicated by the green arrows in Fig. 3.5 b). On the other hand, for single Sn-down molecules and molecules at the edges of the chains, *two* opposite wings are equally bright. This difference is probably the result of intermolecular interactions in the chain, since the single bright wing is very close to two other wings belonging to neighboring molecules. In contrast, the according wings of the molecules at the edges of the chain possess only one neighbor and the single molecules none.

In Fig. 3.5 c) and d), the substrate lattice is superimposed on a part of the images. It is revealed that the adsorption site of the molecule in the lower left has changed during the switching process from Sn-up to Sn-down. To visualize this, one of the lattice points is marked by a blue circle in both images. We have observed this behavior frequently. This further indicates, that different adsorption sites are favorable for the two different SnPc conformations. Therefore, the switching process for free standing molecules is accompanied by a movement of the molecules by $\approx 1/2$ of the row distance of the Ag surface lattice. This finding also agrees with the arrangement of the SnPc molecules within the commensurate c-phase, which will be discussed in the next subsection. Note that the preferred adsorbate site could not be identified unambiguously.

3.1.2 Commensurate low temperature phase

When the SnPc coverage is increased, a commensurate phase (c-phase) can be observed at LT over a certain coverage regime. A minimum total coverage of ≈ 0.5 ML is necessary to observe the formation of this phase in LEED at liquid nitrogen temperature. For coverages below, only small chains of Sn-down and single Sn-up molecules are found on the surface as discussed before. Once the critical coverage is reached, island formation starts on the surface upon cooling to LT, while at RT still only diffuse intensity is observed in LEED. In contrast to the measurements described in the last subsection, the STM tip was biased in these measurements, so that negative bias voltages correspond to tunneling into empty states of the sample.

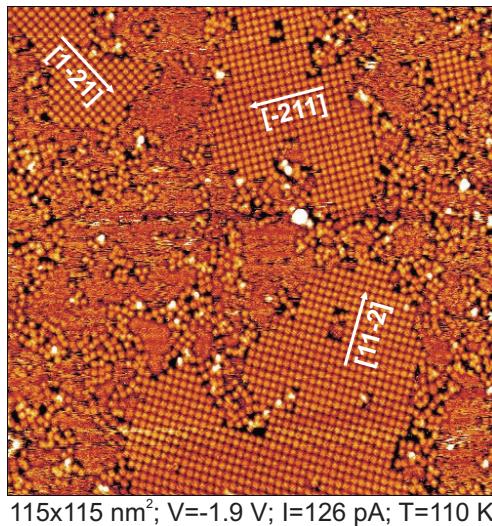


Figure 3.6: STM image of 0.7 ML SnPc on Ag(111) at 110 K. Islands of different rotational domains can be seen as well as disordered regions in between. The white arrows mark high symmetry silver directions.

Figure 3.6 shows an STM image of a large Ag terrace covered with (0.7 ± 0.1) ML SnPc at LT. Islands of different sizes and rather arbitrary shapes can be found coexisting with disordered regions in between them. The molecules in the islands are packed in rows aligned with the Ag substrate, so that three rotational domains can be found. This is visualized by the white arrows in the figure, which show the $\langle 1\bar{2}1 \rangle$ directions of the substrate. One row direction of the molecules is always found to be aligned exactly along one of these high symmetry substrate directions.

A closer look at the structure of a single island is shown in Fig. 3.7. As can be seen, the SnPc islands consist of both Sn-down and Sn-up molecules. Each island can also be described by rows parallel to one of the high symmetry

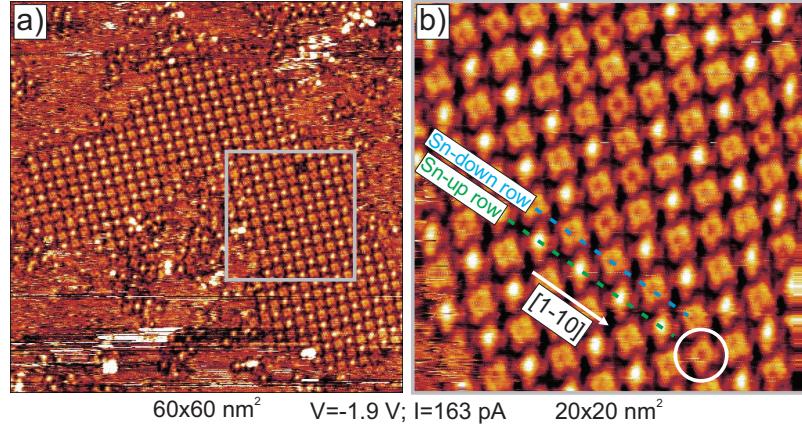


Figure 3.7: a) STM image showing a single island of SnPc. A zoom of the region marked by the gray square is shown in b). Sn-up and Sn-down species can be identified within the islands. The dashed lines indicate rows of Sn-up and Sn-down. Sn-down molecules occur as defects in Sn-up rows (white circle) in some places.

$\langle 1\bar{1}0 \rangle$ directions, along which the longer unit cell vector $\vec{A} = \begin{pmatrix} 7 \\ 0 \end{pmatrix} \begin{pmatrix} \vec{a} \\ \vec{b} \end{pmatrix}$ found in SPA-LEED is oriented. Rows of Sn-up molecules alternate with rows of Sn-down perpendicular to the row directions as indicated by the dashed lines. The order of this up-down pattern is not perfect, however. In some cases, Sn-down molecules can be found as ‘defects’ in Sn-up rows (see e.g. the molecule marked by the circle in the figure), but not vice versa. Counting the molecules in different images results in $\approx 38\%$ showing the Sn-up conformation, which further confirms that the adsorption with the Sn atom pointing down is more stable. This is in agreement with the irreversibility of the switching discussed for the g-phase above. In contrast, the stoichiometric ratio of Sn-down to Sn-up molecules was found to be $\approx 1:1$ in the gas-like phase. However, the two phases were investigated at different temperatures. A temperature dependence of the Sn-up ratio is possible, since different thermal energies can effect the probability to overcome the energy barrier for the conformational change from Sn-up to Sn-down. Alternatively, the Sn-down conformation might be more favorable in close packed structures.

Sn-up and Sn-down molecules adopt different in-plane orientations. However, the Sn-down defect molecules in the Sn-up rows are oriented in the same way as the Sn-up ones. Defect-free regions are described by a chessboard-like pattern with a unit cell containing one Sn-up and one Sn-down molecule, which qualitatively fits to the area of the unit cell found in SPA-LEED [8] and also agrees with the findings from XSW [42]. The knowledge of the unit cell from LEED can be used to correct the distortions in the STM images and measure the angular orientations of the two species relative to the substrate. Results are

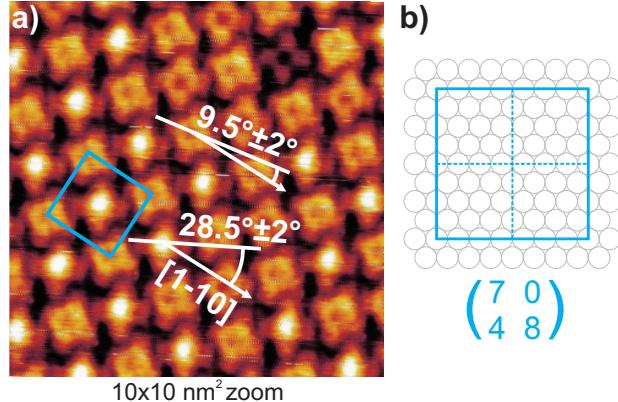


Figure 3.8: a) Zoom of an STM image of the SnPc c-phase. The distortion is corrected, so that the image fits the dimensions of the LEED unit cell drawn in blue. The unit cell is also sketched in b), where the dashed lines visualize, that the adsorption site in the center is different from that in the corners.

shown in Fig. 3.8 a), where angles of $(28.5\pm 2)^\circ$ and $(9.5\pm 2)^\circ$ are found between $\langle 1\bar{1}0 \rangle$ and the diagonal axis of the Sn-up and Sn-down molecules, respectively. Therefore the Sn-up molecules in this phase are well aligned with the substrate like in the g-phase, while the Sn-down molecules are clearly misaligned.

Note that the island formation is not simply an aggregation of the chains found in the g-phase, which consisted of Sn-down only. A transition from g-phase to c-phase by depositing additional molecules onto a cooled substrate will probably not work, since a considerable activation barrier can be expected for the island formation. In our experiments, the deposition was always performed at RT and followed by an annealing of the adsorbate film. The c-phase was then found after cooling down the sample.

The structural motif in the c-phase is also quite different from the packing in the Sn-down chains found for the disordered g-phase. In the g-phase, all molecules show the same in-plane rotation and are oriented with one pair of wings being perfectly aligned along a $\langle 1\bar{1}0 \rangle$ direction of the substrate. This is probably the result of the different coordination of the molecules. In the g-phase, each molecule has at maximum two direct neighbors. In contrast, the molecules in the c-phase islands are surrounded by eight neighbors. Hence, the total intermolecular potentials will be quite different. These different arrangements of the molecules can be explained by pair potential calculations as will be shown at the end of the chapter.

If we define the unit cell such that the centers of the Sn-down molecules lie on its corners, the Sn-up molecules will most probably be located in the middle of the cell due to symmetry reasons. In these positions, Sn-up and Sn-down

molecules occupy different adsorption sites with respect to the substrate lattice (e.g. one top-site and one bridge-site), as can be seen in Fig. 3.8 b). This further supports the indications found before in the g-phase (change of adsorption site upon switching and different symmetry breaking of the molecules). Our findings clearly show the relation between molecular geometry (Sn atom pointing up or down) and adsorption site, caused by different molecule–substrate interactions. The adsorption site preferences in turn influences the favored structural arrangement, i.e. the size and shape of the unit cell.

3.1.3 Point-on-line phase at high coverages

Upon increasing the coverage at RT, a phase transition from the g-phase to a point-on-line phase takes place at approx. 0.9 ML, as was shown in the structural phase diagram in Fig. 3.1. The unit cell of this p.o.l.-phase continuously changes between 0.9 ML and 1 ML, as the repulsing molecules are forced to come closer together. In a very small region between 0.90 ML and 0.94 ML, a transition to the c-phase can be observed upon cooling the sample. Above 0.94 ML, the same LEED pattern is observed at RT and at LT.

STM images from two different preparations of SnPc submonolayers in the p.o.l.-phase will be discussed in this subsection. The coverage in the two measurements was ≈ 0.9 ML and ≈ 0.95 ML, respectively, as determined from the unit cell size obtained by LEED measurements taken after the deposition.

P.o.l.-phase at 0.9 ML coverage

The first preparation showed the known LEED pattern of approx. 0.9 ML SnPc at RT [8]. STM images confirmed this by showing only one type of structure with one molecule per unit cell. However for this preparation, an interesting observation was made upon cooling the sample. The spots of the 0.9 ML phase remained while new spots, described by the unit cell of the c-phase, appeared. This means that only a part of the adsorbate film transformed to the c-phase, while the 0.9 ML p.o.l.-phase still coexisted. Indeed, both phases could also be found in the STM images.

Figure 3.9 shows a drift corrected STM image of the 0.9 ML p.o.l.-phase at LT. One type of domain (A) and a second domain (B), mirrored by $[1\bar{1}0]$, can be found in the image. As before, the distortions in the raw STM image have been corrected, so that the structure matches the according SPA-LEED unit cell, drawn in blue. This SPA-LEED cell has a superstructure matrix of $\begin{pmatrix} 4.98 & -0.05 \\ 2.74 & 5.78 \end{pmatrix}$, taken from reference [9], and is large enough to contain one molecule. Some regions (C) between the ordered domains are covered with disordered molecules. The adsorbate film is therefore not perfectly ordered at this temperature.

All molecules within an ordered domain adopt the same orientation with a small angle of $(2 \pm 2)^\circ$ between their diagonal axis and one of the $\langle 1\bar{1}0 \rangle$

3.1 Scanning tunneling microscopy

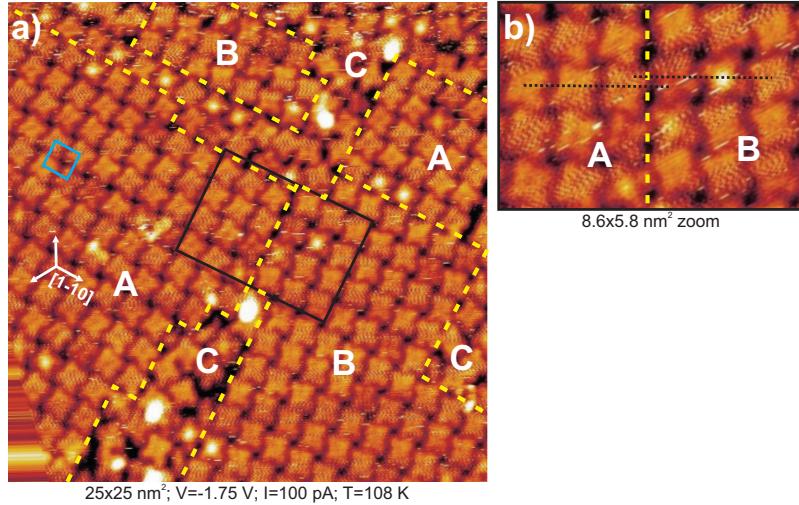


Figure 3.9: Drift corrected STM image of ≈ 0.9 ML SnPc on Ag(111). a) One type of rotational domain (A), as well as its mirror domain (B) can be seen. Areas in between (C) are filled with disordered molecules, demonstrating that the adsorbate film is not perfectly ordered at this temperature. Domain boundaries are illustrated by the yellow dashed lines and the unit cell is shown in blue. A closeup of the region marked by the black rectangle is shown in b), revealing a translational shift between the two domains.

directions. Most molecules have adopted the Sn-down configuration, but some Sn-up molecules can still be found.

The domain boundaries follow rather arbitrary paths. In most cases, a different intermolecular distance (dislocation line) is observed where two domains meet. In the example of the domain boundary between (A) and (B), shown in the closeup in Fig. 3.9 b), the two domains also show a small translational shift along the boundary, as visualized by the black dotted lines.

On other parts of the sample, c-phase domains were found, as already seen in LEED. An exemplary STM image is shown in Fig. 3.10 a). Two islands of different rotational domains can be seen, again coexisting with disordered regions. In contrast to the measurements on the 0.7 ML film, almost all molecules were adsorbed in the Sn-down configuration. When counting molecules in different images, we found only $\approx 9\%$ of the molecules left in the Sn-up geometry in this phase. The dominant structural motif is therefore not described by a chessboard-like alternation of Sn-up and Sn-down here. However, the molecules possess two alternating in-plane orientations, so that the structure is still described by the c-phase unit cell discussed in the last section. The angular difference between the two orientations is $\Delta\theta = (10.6 \pm 2)^\circ$, as shown in Fig. 3.10 b). This is smaller

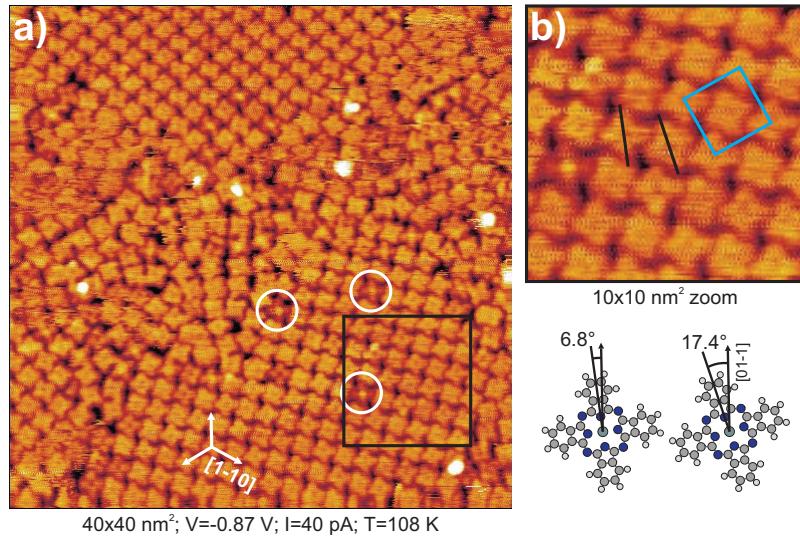


Figure 3.10: a) STM image of a c-phase originating from a phase transition from an 0.9 ML p.o.l.-phase upon cooling. In contrast to the measurements in the last section, almost all molecules are Sn-down species. Some single Sn-up molecules are marked by white circles. b) Closeup of the region marked with the black rectangle. The unit cell (blue) contains two molecules with different molecular orientations.

than the difference found in the 0.7 ML structure, which might be correlated to different intermolecular interactions due to the low Sn-up fraction. It seems that the percentage of Sn-up molecules decreases within the c-phase with increasing coverage. Such a coverage dependence of the fraction of Sn-up molecules indicates that the energy barrier for the switching from Sn-up to Sn-down might be lowered at higher coverages by some unknown mechanism, possibly related to the surface tension in the film.

P.o.l.-phase at 0.95 ML coverages

The second preparation in the p.o.l. regime had a slightly larger coverage of approx. 0.95 ML, as again judged from LEED images. At this coverage, no phase transition occurred upon cooling, which was confirmed in both LEED and STM.

Figure 3.11 a) shows a representative STM image of this preparation. At this high coverage, the mobility of the molecules is sterically so far reduced, that nicely resolved imaging is possible even at RT. Only one structure was found at both RT and LT, containing very closely packed and equally oriented molecules.

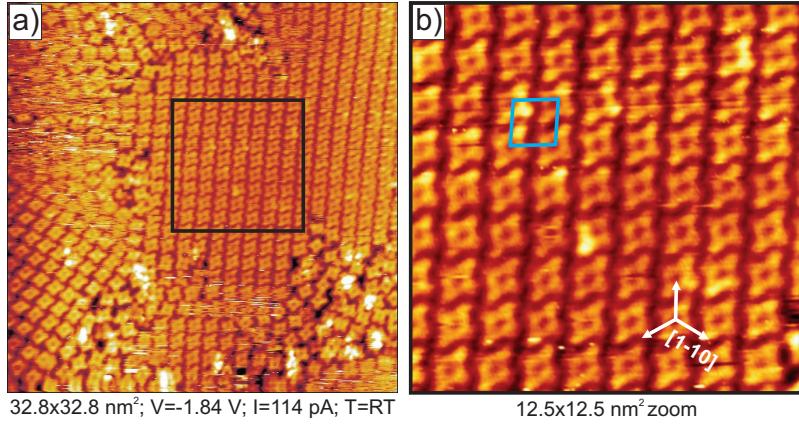


Figure 3.11: a) Image of a SnPc p.o.l.-phase at 0.95 ML coverage at RT. The molecules in the islands are very closely packed and equally oriented. A closeup of the region marked by the black rectangle is shown in b). The image was corrected, so that the structure matches the unit cell drawn in blue, which is known from SPA-LEED.

Fig. 3.11 b) shows a closeup of the region marked with the black rectangle. Different in-plane orientations are not possible since the molecules do not have any margin for rotation anymore. Similar to the measurements discussed above, the image was corrected to fit the unit cell found in SPA-LEED for 0.95 ML, which has a matrix of $\begin{pmatrix} 4.79 & -0.24 \\ 2.60 & 5.62 \end{pmatrix}$. From the corrected image, the average angle between the diagonal molecular axis and the [1̄10] direction of the substrate was found to be $(0.4 \pm 1.1)^\circ$. Again, the molecules are almost perfectly aligned along the substrate. This shows that the molecules try to optimize their interactions with the substrate even in these closely packed incommensurate structures. At this high coverage all molecules adopt the Sn-down geometry, which confirms the tendency for decreasing Sn-up fractions mentioned before. Apparently the Sn-up geometry becomes more unfavorable with increasing coverage. This could be related to intermolecular interactions, since the density in the adsorbate film increases in the p.o.l.-phase. Alternatively, the Sn-up geometry might only be stable in its favored (high symmetry) adsorption sites, which can not be sustained when the layer is closed.

3.2 Scanning tunneling spectroscopy

Scanning Tunneling Spectroscopy (STS) measurements have been performed on molecules in the g-phase and p.o.l.-phase to investigate the local electronic structure of the sample. For SnPc in the g-phase, STS was only performed on

Sn-down molecules at T=5 K. Spectroscopy on Sn-up molecules results in a switching of the molecules to Sn-down, as discussed in section 3.1.1. Before and after each scan, a short STM image was taken to ensure that the molecule, on which the spectroscopy was done, did not drift during scanning. For the STS scans, the tip was placed at the desired location above the molecule in a fixed z -distance. The bias voltage was then changed continuously from -2 V to 2 V and back. Forward path and return path were compared to further ensure, that no changes occurred in between. STS scans are plotted as differential conductance (dI/dV) vs. bias voltage, so that electronic states appear as peaks in the spectra.

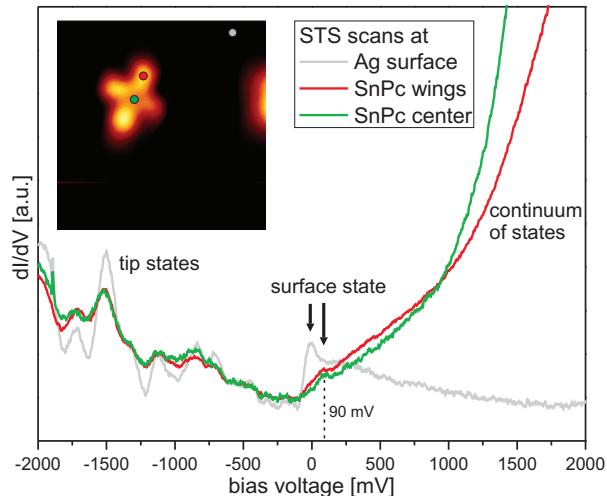


Figure 3.12: STS scans on an isolated Sn-down molecule in the g-phase at a current setpoint of 0.18 nA. The scans were performed on the center (green) and on the wings (red) of the molecule and are compared to a scan on the bare silver surface (gray), as shown in the inset.

Figure 3.12 shows an example for STS scans on an isolated Sn-down molecule. The green curve shows a scan taken above the center of the molecule, as indicated in the STM image in the inset. The red curve is an average of four scans taken at the centers of each of the four wings. Another scan, shown in gray, was done on the bare substrate surface for comparison. It can be seen that some states were measured on the negative bias side (occupied states) of the gray curve. As was already mentioned in section 2.2, the tunneling current is a convolution of sample DOS and tip DOS. Since the silver surface should appear rather featureless, the observed states are assigned to the tip. If and how intense tip states appear generally depends on the shape of the STM tip. An ideal tip for STS would be a rather broad tip with a single protruding apex atom, for which tip states should not be visible. Obviously our tip was not perfectly

3.2 Scanning tunneling spectroscopy

shaped in these measurements. Occupied states also appeared in the scans on the molecule at the same energetic positions, but they were clearly damped. We can conclude that these are also tip states. The Shockley surface state of the metal substrate is visible at the Fermi-level as expected. In the red and green curves, a small peak is present at ≈ 90 meV. This state might be the strongly damped and slightly shifted (depopulated) surface state. A shift of the surface state due to the interaction with an adsorbed molecule has been reported e.g. for tetracene on Ag(111) [56]. Interestingly, both the red and green curve are almost identical and appear completely featureless apart from the mentioned tip and surface states. No molecular states close to the Fermi-level can be identified, although the voltage range should be sufficient. For high positive bias, the differential conductance increases strongly due to the presence of a continuum of energetically higher unoccupied states.

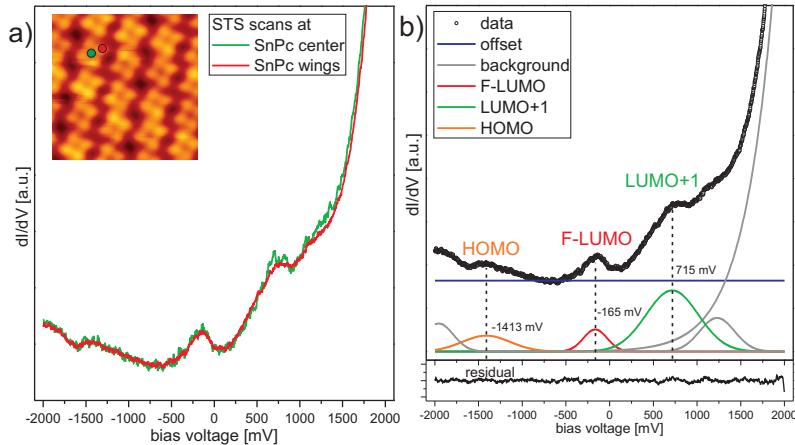


Figure 3.13: a) STS scans on a Sn-down molecule in a p.o.l.-phase monolayer at a current setpoint of 0.14 nA. Center and wings of the molecule have been probed, as before. b) Fit model for the determination of the peak positions.

Furthermore, STS measurements have been performed on a monolayer structure, which was prepared by depositing a multilayer and thermally desorbing all but the first layer of molecules. STS scans were performed on this film to compare them with the scans from the g-phase. The result is visualized in Fig. 3.13 a). In the p.o.l.-phase, no regions of bare silver can be found, so that no according STS scans could be performed on the substrate for comparison. Scans on the molecule have been taken above the center and above the wings, as before. As for the g-phase, the scans at both positions yielded almost exactly the same curves. However, compared to the g-phase scans, the scans of the p.o.l.-phase look completely different. While no surface state or tip states were visible, molecular states clearly appeared. The peak positions have been estimated by fitting the spectrum with a constant offset and a number of Gaus-

sian functions, as seen in Fig. 3.13 b). One peak is located at approx. -165 mV on the occupied states side close to the Fermi-level. In UPS measurements, a similar peak showed up at approximately the same energy position [57]. This peak was found to be cut by the Fermi-level and thus partially filled. Therefore, the peak corresponds to the SnPc LUMO, which is partially filled upon charge transfer from the substrate and then named *former* LUMO (F-LUMO). Another peak on the occupied side can be identified as the SnPc HOMO, although its intensity is very low. Its position at ≈ -1413 mV also corresponds well to the results of two independent UPS measurements [57, 58]. The third feature is an unoccupied state appearing at ≈ 715 mV. This state most probably represents the second to lowest unoccupied state (LUMO+1).

An STS study on the c-phase has not been done in the context of this work. However such a study was reported by Toader et al. [58]. On the unoccupied binding side, their results are comparable to the findings for the p.o.l.-phase described above. One state could be clearly resolved at a position between 0.5 and 0.75 V, comparable to the LUMO+1 position in the p.o.l.-phase. The exact position was found to depend on the tip-sample distance. The authors call this state the LUMO, however the same molecular orbital is meant. A small peak close to the Fermi-level on the occupied side can be found in their spectra as well, which could be the F-LUMO mentioned above. On the occupied side, a remarkable difference occurs. In the c-phase spectra, a large peak is observed at ≈ -0.75 V, which is not visible in our p.o.l.-phase spectra.

STS probes the local electronic structure, as given by the molecular orbitals. However, we only know the shape of the orbitals from DFT calculations representing molecules in the gas phase, without considering interactions to each other or to the substrate. For molecules that are adsorbed on a metal surface, the orbitals do not necessarily look the same. Charge transfer from the silver surface was already discussed and also shows up in the dI/dV spectra, manifesting in the LUMO shifted to the occupied states side. The differences between the spectra might be the result of different adsorption sites or of intermolecular interactions. The molecular environment is considerably different for the three SnPc phases studied. In the g-phase an isolated molecule was investigated, while the molecules in the c-phase and p.o.l.-phase are surrounded by eight neighbors. The type of neighbors (four Sn-up plus four Sn-down or eight Sn-down, respectively) is in turn different for c-phase and p.o.l.-phase. Our results thus show the importance of the intermolecular environment for the electronic structure of a molecule, which can in turn influence the geometric structure formation.

3.3 Pair potential calculations for SnPc

The experimental finding that the phthalocyanine molecules show intermolecular repulsion on Ag(111) at RT was supported by pair potential calculations from Kröger et al. [32, 33] for the interaction between two CuPc molecules. The authors calculated the intermolecular potential considering electrostatic and van-der-Waals forces in a similar way as described in chapter 2.4. In the resulting

3.3 Pair potential calculations for SnPc

potential map, small attractive potential minima occur, representing favorable locations for the second molecule. These local minima are shallow and therefore can be overcome easily by the molecules at RT, which explains that no ordered structure is found on the Ag(111) surface at this temperature. The molecules are not trapped in local potential minima, but can always reach the total minimum when their distances are maximized. However, when the temperature is reduced, the molecules "freeze" in the local minima, which leads to island formation when the coverage is high enough. These simple calculations explain the adsorption behavior on Ag(111), but they do not explain the tendency for chain formation of CuPc on Cu(111), since they do not take interactions with the substrate into account. Kröger et al. modified their calculations and accounted for charge donation and backdonation between the Cu(111) substrate and a CuPc molecule by modifying the partial charges within the adsorbate. This simulates the charge transfer between molecules and surface. As a consequence, two attractive minima appeared on opposing sides of the CuPc molecule, which explains qualitatively why chain formation is favored over island formation for CuPc on this substrate [32].

As mentioned before, the adsorption behavior of the Sn-up molecules on Ag(111) resembles the CuPc on Ag(111) case, while the Sn-down molecules behave similar to CuPc on Cu(111). Therefore, similar pair potential calculations have been performed in this work to model the adsorption of SnPc on Ag(111). Charge transfer between the Ag(111) surface and SnPc (sub-)monolayer films has been observed in UPS measurements by Häming et al. [57]. The LUMO of SnPc was found to be partially filled as a consequence of the adsorption on the silver surface. For the following calculation we assumed that all atoms within a Sn-down molecule, which have a significant overlap of wave functions with the substrate, donate an equal amount of charge. Therefore, the partial charges of all except the hydrogen atoms were lowered by $\Delta q = 1.5e^-/41=0.037e^-$. The total amount of $1.5e^-$ was chosen because the LUMO is not completely filled in the UPS measurements in contrast to CuPc on Cu(111). A backdonation of an equal amount of charge was further applied, so that the sum of all partial charges remains zero. However, it can be assumed that charge is not donated

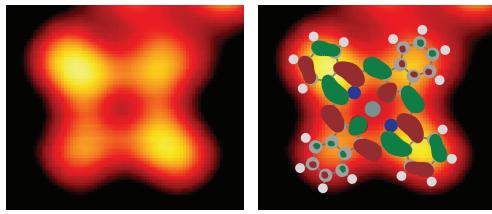


Figure 3.14: The STM contrast of the Sn-down molecules, showing two brighter wings, is assumed to be the result of charge transfer into one of the degenerate LUMOs. On the right, a ball-and-stick model is superimposed together with the geometrical distribution of this LUMO.

back to all atoms, but only to those that contribute to the SnPc LUMO. This

is justified by looking at the appearance of the Sn-down molecules in the STM images, see Fig. 3.14. One pair of opposite wings of the Sn-down molecules was always found to appear brighter than the other pair. The reason for this must be related to the different registry of the two wing pairs with the substrate. We assume that the different contrasts of these wings in the STM images is caused by backdonation of charge from the substrate. From DFT calculations for SnPc in the gas phase, it can be seen that the two lowest unoccupied orbitals are at the same energy position. The LUMO is hence degenerate. Since each of the two LUMOs is mainly located on one pair of wings, we assume that backdonation only occurs from the substrate into the atoms contributing to one of these orbitals. The partial charges of the corresponding 26 atoms were therefore increased by $\Delta q = 1.5e^-/26=0.058e^-$. This redistribution of charge inside the molecule reproduces the symmetry breaking and influences the intermolecular potentials considerably.

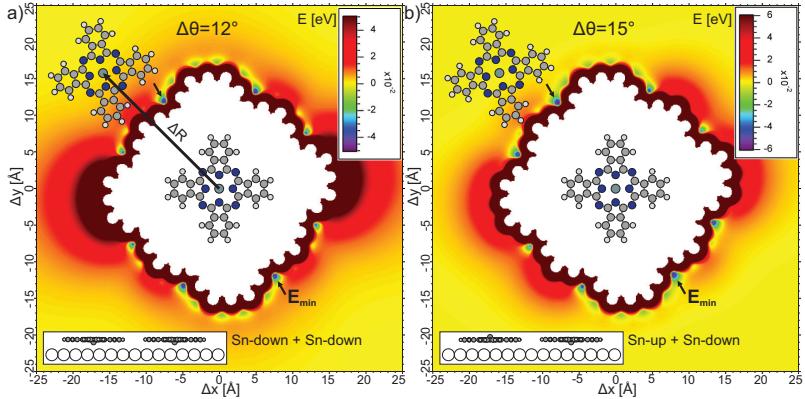


Figure 3.15: Pair potential maps for a) two laterally displaced Sn-down molecules and b) for one Sn-up and one Sn-down molecule. Charge transfer between Sn-down and the substrate was simulated, as described in the text.

The intramolecular structure of SnPc was adopted from DFT calculations, optimizing the geometry. However, DFT describes free molecules in the gas phase, where SnPc is considerably bent. When adsorbed on a Ag(111) surface on the other hand, the molecules are rather flat except for the central Sn atom, as shown by XSW [42]. The DFT geometry was modified to account for this fact in the pair potential calculations.

Figure 3.15 a) shows a resulting map of pair potentials for the interaction between two laterally displaced Sn-down molecules. The potential energy for different lateral arrangements of the molecules was calculated as described in section 2.4. While one molecule was placed in the center of the image, the position of the other molecule was repeatedly changed in steps of 0.1 Å along x and y . For each distance vector $\Delta R = (\Delta x, \Delta y)$ between the centers of

3.3 Pair potential calculations for SnPc

the two molecules, the potential energy was calculated and is displayed by the applied color code. Blue shades represent negative potentials, while yellow to red regions are positive. Hence, distance vectors ΔR ending in blue regions of the figure represent molecular arrangements which are energetically favorable and therefore stable. Configurations in which two involved atoms would be closer than 0.8 Å have not been calculated. This is the case for the white regions around the middle of each potential map. The same calculation was repeated for different relative in-plane angles between the two Sn-down molecules from 0° to 90° in steps of 1°, yielding a set of potential maps. In Fig. 3.15 a), the map with a relative angle of $\Delta\theta = 12^\circ$ is shown, which contains the deepest energy minima of all relative orientations. As can be seen, most intermolecular configurations are energetically unfavorable. The strong repulsive regions on the left and right are the result of the charge redistribution described above. Some rather localized potential minima can be found in the map. The two deepest are located at $\Delta x = -7.5$ Å (7.5 Å) and $\Delta y = 11.9$ Å (-11.9 Å) with an energy of $E_{\min} = -0.048$ eV. These positions correspond to an intermolecular distance of $|\Delta R| = 14.07$ Å.

The intermolecular potential is slightly different for the interaction between one Sn-up and one Sn-down molecule, as shown in Fig. 3.15 b). In this case, a relative rotation of $\Delta\theta = 15^\circ$ yields the potential map with the deepest minima, which are located at $\Delta x = -7.9$ Å (7.9 Å) and $\Delta y = 11.7$ Å (-11.7 Å). The energy minimum of $E_{\min} = -0.059$ eV is smaller than the one for two Sn-down molecules, while the optimum binding distance of $|\Delta R| = 14.12$ Å is comparable.

These calculations yield favorable relative arrangements of two SnPc molecules. They are therefore independent of a certain structure formation. In the following, the structures found experimentally for the different phases will be compared to the according intermolecular potential maps.

g-phase

For the g-phase at low coverages and low temperatures, chains of equally oriented Sn-down molecules were found. Therefore, the structure within the chains will be discussed in terms of the pair potential between two Sn-down molecules with a relative orientation angle of $\Delta\theta = 0^\circ$ as shown in Fig. 3.16 b). The distance vector between two molecules in the chain was measured from STM images and can be expressed by polar coordinates $(R, \alpha) = (14.3\text{\AA}, 27.8^\circ)$, as shown in Fig. 3.16 a). In the corresponding pair potential map, this vector ends very close to one of the potential minima. Therefore, pure intermolecular interactions describe the relative arrangement of two molecules quite well. However, the calculation can not explain the observed alternation of distance vectors in the chain. Two successive distance vectors are always mirrored by the chain axis $(R, \alpha) \leftrightarrow (R, 360^\circ - \alpha)$, so that the molecules follow a zig-zag pattern. This is not reproduced by the calculations, since a linear chain with identical ΔR vectors between all molecules would be equivalent. This also holds when the

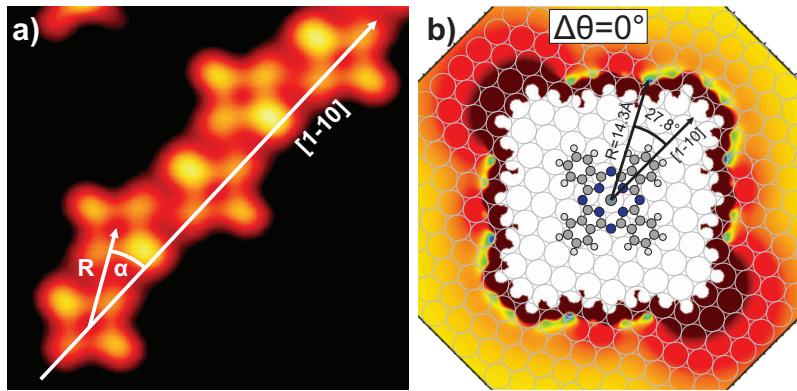


Figure 3.16: The relative orientation between neighboring molecules within a g-phase chain is described by polar coordinates R and α , as shown in a). In b) the pair potential map for two equally oriented Sn-down molecules is shown. The measured distance vector of the g-phase fits well to one of the potential minima.

potential map between a third molecule and two molecules fixed in the optimum arrangement is calculated. An explanation is offered by the appearance of the molecules in the STM image. As already mentioned before, for molecules within the chains one wing appears brighter than the three others. This indicates an unequal charge distribution in the four molecular wings, which implies a deformation of the LUMO orbitals. That LUMO state containing the brighter wing has lost its 2-fold symmetry due to the interaction with the substrate and the neighboring molecules, an effect which is not considered in the calculations. This induced asymmetry obviously favors (and hence causes) the zig-zag chain formation.

The pair potential calculation in Fig. 3.15 above yielded an optimum angle of 12° between two Sn-down molecules, in contrast to the equal orientation found in the chains. The reason for this difference is probably the optimization of the interaction with the substrate by aligning the pairs of wings along high symmetry directions.

c-phase

In the c-phase of SnPc/Ag(111), an alternating sequence of Sn-up and Sn-down molecules was found within the islands. This can be explained by the smaller intermolecular potential energy of Sn-down–Sn-up compared to Sn-down–Sn-down. However, an effect of different adsorption sites might also play a role, as discussed above. The calculated optimum angle of $\Delta\theta = 15^\circ$ between molecules in the two geometries fits well to the experimentally found value of 19° shown above in Fig. 3.8.

3.3 Pair potential calculations for SnPc

In a more sophisticated pair potential calculation, the optimum position and orientation of a Sn-up molecule inside of a $\begin{pmatrix} 7 & 0 \\ 4 & 8 \end{pmatrix}$ unit cell was determined, as shown in Fig. 3.17. Intermolecular interactions between a Sn-up molecule and

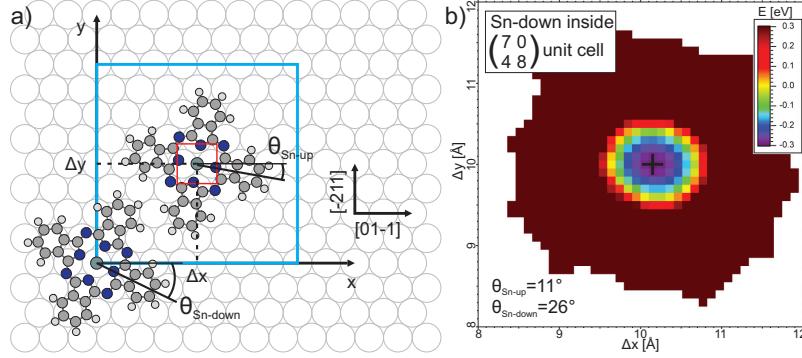


Figure 3.17: Pair potential calculation for a Sn-up molecule inside the c-phase unit cell (blue rectangle): a) shows the nomenclature and results for the used distances and angles. A detailed calculation was done only for a small region (marked by the red square); b) shows the according potential map for the optimum in-plane rotations of both types of molecules. The position of the absolute minimum is marked by a black cross.

its eight nearest neighbors (four Sn-down molecules in the corners of the unit cell and the four nearest Sn-up molecules) have been accounted for. In this way, the effect of the substrate is partially taken into account in terms of the unit cell found experimentally, which is the result of *all* interactions within the system. At first a fast calculation was done to narrow down the region in which the minimum is found. Attractive potentials are only found around the center of the unit cell, since only in this region the molecule does not overlap with the corner molecules. In a more detailed calculation, the position (Δx , Δy) of the grid of Sn-up molecules was scanned in steps of 0.1 \AA while the Sn-down molecules remained on fixed positions. This calculation was repeated for in-plane angles $\theta_{\text{Sn-up}}$ from 0° to 90° between the diagonal axis of Sn-up and the $[01\bar{1}]$ direction, and for $\theta_{\text{Sn-down}}$ from 0° to 180° for the Sn-down molecules in steps of 1° each. In Fig. 3.17 b) the map for the set of angles containing the deepest energy minimum of all maps is shown. Optimum angles of $\theta_{\text{Sn-up}} = 11^\circ$ and $\theta_{\text{Sn-down}} = 26^\circ$ to $[01\bar{1}]$ have been found, which agree well with the angles of 9.5° and 28.5° found experimentally for the two species. The total energy minimum is located exactly in the center of the unit cell, which is expected due to the symmetry of the coordination. This good qualitative agreement demonstrates the predictive power of our calculations. The optimum angular difference of $\Delta\theta = 15^\circ$ between the molecules is the same as found before for the interaction between only two molecules.

The reason for the structure formation in the c-phase can be nicely visualized further by a pair potential calculation without unit cell constraints shown in Fig. 3.18. The pair potential map between one Sn-up and one Sn-down is

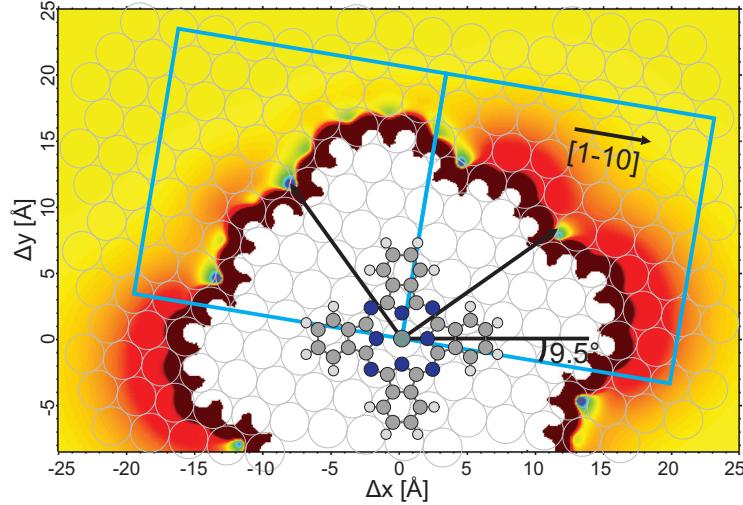


Figure 3.18: Potential map for the optimum geometry found experimentally for the c-phase, regarding the orientation of the central Sn-up molecule relative to Sn-down and to the substrate. The adsorption sites of the nearest Sn-down molecules in the c-phase unit cell match well to the locations of potential minima.

shown again for a relative rotation of $\Delta\theta = 15^\circ$ between the molecules, as this was the optimum found for the c-phase. The substrate lattice is superimposed on the image, so that the in-plane orientation of the Sn-up molecule matches the observed angle of 9.5° to a high symmetry direction of the substrate. In this model, the Sn-up molecules are located at the corners of the $\begin{pmatrix} 7 & 0 \\ 4 & 8 \end{pmatrix}$ unit cell, which is drawn in blue, while the Sn-down molecules are located at the center. Due to the commensurate registry, high symmetry adsorption sites are likely. If the Sn-up molecules are, e.g., placed on top-sites, then the nearest Sn-down neighbors are on bridge sites. However the locations of both species could also be exchanged. A hollow site for the corner molecules is less likely, because the center of the cell would not lie on a high symmetry site in this case. Either way, the adsorption sites of the unit cell centers match the positions of local intermolecular potential minima quite well. Therefore, the structure in the c-phase represents an optimum compromise between a minimized intermolecular potential and an adsorption on high symmetry adsorption sites (probably top and bridge) along with a commensurate registry, which is favorable for the adsorbate–substrate interaction. The mismatch between a favorable adsorbate lattice, expressed by the positions of potential minima, and a lattice commensurate to the substrate is small, so that only a relatively small elastic strain has to

3.3 Pair potential calculations for SnPc

be induced in the adsorbate film for matching the lattices. This is also supported by the finding, that no regular dislocations are found within the SnPc domains. If a lattice mismatch is high (above a *critical* value), dislocations can become favorable over a purely strained layer, since they reduce the elastic stress [49].

p.o.l.-phase

A similar comparison between experiment and theory can be made for the molecular arrangements in the p.o.l.-phase. Within this phase, the main part of the surface is covered by Sn-down molecules only. A series of incommensurate unit cells with point-on-line coincidence was found, containing one molecule each. The measured arrangements are therefore compared to the potential map between two equally oriented Sn-down molecules, as done for the g-phase before.

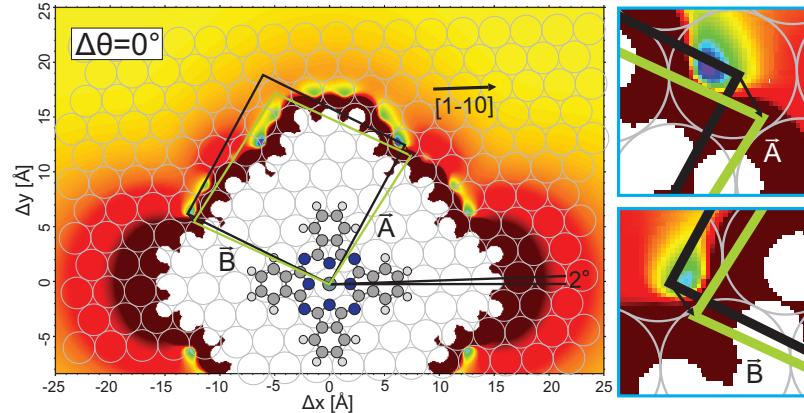


Figure 3.19: Potential map for two equally oriented Sn-down molecules. Unit cells for 0.9 ML and 1.0 ML coverage are drawn in black and green, respectively. The center molecule was rotated by 2° relative to the substrate, as measured in STM. Two closeups are shown on the right.

Figure 3.19 shows that in the unit cell for 0.9 ML SnPc on Ag(111) (drawn in black), the two nearest neighbor molecules in the edges of the cell are located close to potential minima. If the coverage is increased, the unit cell changes continuously with the unit cell vectors moving along substrate lines until the 1.0 ML cell is reached (drawn in green). It can be seen that the intermolecular interactions become more and more unfavorable with increasing coverage until both vectors end in rather strong repulsive regions (see closeups on the right side of Fig. 3.19). This explains, why the structures found for higher coverages (close to 1 ML) are not stable at lower coverages, i.e. that no island formation occurs for these structures. The energy penalty stemming from this unfavorable arrangement is obviously compensated by a higher number of molecules per surface area and the adsorption energy involved. This is valid for a certain coverage

range up to 1 ML and explains, why this unit cell describes the maximum reachable molecular density on the surface. The movement of the unit cell vectors into the positive potential regime expresses the increasing repulsion and stress in the adsorbate film as more molecules are deposited on the surface. At some point, the repulsive interaction is so strong, that it becomes more favorable for additional molecules to start forming a second layer.

3.4 Conclusion

The adsorption of SnPc on Ag(111) has been investigated by STM in order to complement previous SPA-LEED and XSW results [8]. For different coverages and temperatures, structures were found which are compatible with the phases observed in LEED. Pair potential calculations have been performed to investigate the contribution of the intermolecular interactions to the structure formation in each phase.

In the g-phase at low coverages, two adsorption geometries (Sn-up and Sn-down) of the SnPc molecules were found. A chain formation of the Sn-down molecules was observed and further investigated. It could be explained qualitatively by considering asymmetric charge transfer into the LUMO of Sn-down molecules which also causes a symmetry breaking of the molecules and a deformation of at least one of the LUMOs. Sn-up and Sn-down molecules were found to prefer nonequivalent adsorption sites, which differ by half of a substrate row distance.

For the commensurate c-phase, which is only stable at LT, the unit cell was found to contain one Sn-up and one Sn-down molecule as expected. Pair potential calculations revealed a deeper energetic minimum for the interaction between Sn-up and Sn-down compared to that between two Sn-down molecules, if charge transfer with the substrate is included. A substrate mediated interaction based on donation and backdonation of charge was proposed before as a possible driving force for the structure formation in the c-phase islands [8]. The charge accumulation in the substrate upon donation from the Sn-down molecules was assumed to be responsible for the intermolecular repulsion, which is dominant in the p.o.l-phase. This repulsion is minimized in the c-phase, since the charge transfer between Sn-up and the substrate is expected to be considerably weaker. The orientations of the molecules relative to the substrate could be determined from STM as well. These angles are well reproduced by the pair potential calculations, which shows that the structure is quite favorable in terms of the intermolecular potentials. The commensurability of the unit cell on the other hand shows that the interaction with the substrate is simultaneously optimized in this phase.

For higher (sub-)monolayer coverages in the p.o.l-phase, the commensurability can not be sustained due to sterical reasons. This behavior could be visualized in terms of the intermolecular potentials, which were found to become gradually more unfavorable when approaching the monolayer coverage.

3.4 Conclusion

Hence the molecular density in the first adsorbate layer can only be increased as long as the energy gain for the total system through the increasing adsorption energy compensates for this effect. Not being able to remain in their preferred (c-phase) adsorption sites, the molecules align with the substrate as well as they can regarding their in-plane orientation and registry with the Ag lattice. This results in the series of point-on-line structures, in which one diagonal axis of the molecules is well aligned along the high symmetry directions of the substrate. Almost all molecules were found to be adsorbed in the Sn-down geometry. The Sn-up geometry is obviously not stable due to the high molecular density and/or unfavorable adsorption sites in this phase.

It can be concluded, that the structure formation of SnPc on Ag(111) is largely understood in terms of the interplay between molecule–molecule and molecule–substrate interactions. It has been demonstrated that the intermolecular interactions strongly influence the adsorbate structures formed on the Ag(111) surface.

4 F₁₆CuPc on Ag(111)

Previous investigations in our group focused on the study of phthalocyanines that differ by the choice of the central metal atom (or group). Another possibility to modify the electronic properties of a molecule is to exchange its end groups or terminating atoms. An interesting example is perfluorinated copper-phthalocyanine (F₁₆CuPc), in which the outer hydrogen atoms in a CuPc molecule are replaced by fluorine atoms. Apart from this, the structures of both species are very similar. However, due to the high electronegativity of the fluorine atoms, a considerably different intermolecular interaction can be expected for F₁₆CuPc.

Before turning towards the investigation of CuPc/F₁₆CuPc organic heterosystems in chapter 5, the adsorption of each single component should be understood. Therefore this chapter deals with the adsorption behavior of F₁₆CuPc on the Ag(111) surface.

Previously, the system has been investigated with STM by Huang et al. [59, 60]. Their results showed that F₁₆CuPc tends to form chains of identically rotated, flat lying molecules in the first monolayer. Two different orientations with respect to the substrate occur. Also, neighboring chains are usually shifted against each other. An XSW study has been performed by Gerlach et al. [61], which yielded information about the adsorption height of the molecules. The authors showed that F₁₆CuPc is probably rather physisorbed on the Ag(111) surface considering the adsorption heights of 3.25 Å for the carbon atoms and 3.45 Å for the fluorine atoms. These values are comparable to the adsorption height of CuPc/Au(111) [62], which is also physisorbed as confirmed by UPS [46]. The adsorbed F₁₆CuPc molecules are bent with the fluorine atoms pointing away from the surface.

This can be compared with the molecular geometry for a free molecule, as shown in Fig. 4.1. The optimized geometrical structure and the electronic structure were calculated with the program Gaussian [35], using the B3-LYP functional and LANL2DZ basis set. A ball-and-stick model as well as some of the resulting molecular orbitals are shown in Fig. 4.1. While the HOMO-1 is located in and around the center of the molecule, the HOMO is mainly distributed at the carbon atoms. Two degenerate LUMO orbitals exist, which are mainly located at carbon and nitrogen atoms. The molecule is perfectly flat in the gas phase and has a diameter of 15.6 Å along its diagonal.

In the following sections, the (sub-)monolayer growth of F₁₆CuPc on Ag(111) is investigated by analyzing SPA-LEED measurements at room temperature and at a low sample temperature of approx. 100 K. Additionally, STM measurements have been performed and related to the LEED results.

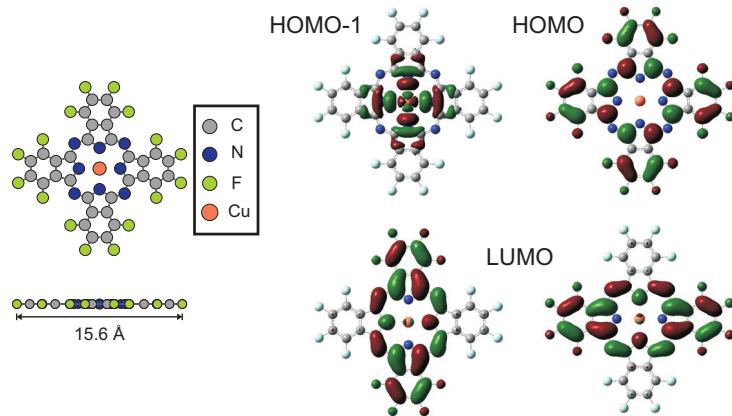


Figure 4.1: Optimized geometrical structure of $F_{16}CuPc$ and four exemplary molecular orbitals calculated from DFT (B3-LYP functional, LANL2DZ basis set) representing molecules in the gas phase. The first two unoccupied orbitals are located at the same energy, i.e. the LUMO consists of two degenerate orbitals.

4.1 Structural phase diagram

SPA-LEED measurements have been performed on many different (sub-)monolayer films and some multilayer films. The sample preparation will be shortly described in the following. During the deposition of $F_{16}CuPc$ films by OMBe from a Knudsen cell, rather short SPA-LEED scans (45 s) were repeated at intervals of 1 min. This enabled a very good control over the adsorbate growth, as the formation of phases, and in particular phase changes, could be observed *in situ*. Simultaneously, the ion current signal at $m/z = 200$ amu was monitored by a Quadrupole Mass Spectrometer (QMS) to control the incident molecular flux. This mass corresponds to one $C_8N_2F_4$ fragment of the molecule in analogy to the well known fragment at 128 amu found for non-fluorinated phthalocyanines, e.g. CuPc [63]. The mass signal of the intact molecules could not be monitored, since it is outside the measuring range of our QMS. Keeping the ion current at a fixed level, a constant deposition rate of typically ≈ 0.1 ML/min was ensured.

The results of the SPA-LEED study are summarized in the structural phase diagram in Figure 4.2. Two different phases could be distinguished. At room temperature, diffuse, disk-like or ring-like scattering intensity around the $(0,0)$ -spot was observed for submonolayer coverages, indicating a disordered phase. When a certain critical coverage was exceeded, spots and streaks appeared quite abruptly in the LEED image, while the diffuse intensity disappeared. Further increasing the coverage Θ into the multilayer regime only resulted in a higher background intensity while the spot pattern remained the same. Another phase transition to the same ordered pattern occurred, when the disordered phase

4.1 Structural phase diagram

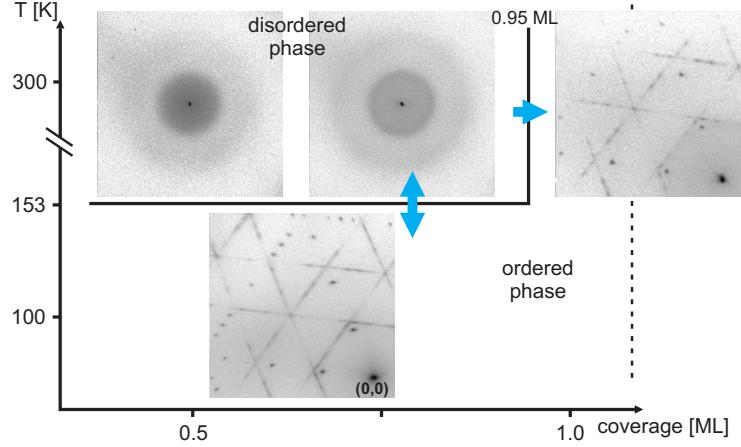


Figure 4.2: Structural phase diagram of F_{16}CuPc on $\text{Ag}(111)$, showing two phases at different coverages and temperatures as well as representative SPA-LEED images. The phase transitions occur at a coverage of ≈ 0.95 ML at RT, and at smaller coverages upon cooling to L-N₂ temperature.

was cooled down. This transition occurred for sub-ML coverages as low as 0.3 ML, whereby a transition temperature of $T_{\text{trans}} = (153 \pm 10)$ K was found at a coverage of ≈ 0.4 ML. The only difference to the ordered RT phase is the better signal-to-background ratio of the spot intensities, which is expected due to the temperature dependence of phonon scattering [13]. The disorder-to-order phase transition induced by cooling is reversible, i.e. the system can be switched back to disorder by warming the sample up again. This behavior is similar to that of other, non-fluorinated phthalocyanine molecules on $\text{Ag}(111)$ [8, 45, 64]. Obviously, the reduced mobility of the molecules when cooled down leads to a change in balance of molecule–molecule and molecule–substrate interactions. As a consequence, ordered 2D-islands are formed at LT, while a dilute film is formed at RT. This structure formation will be discussed in a subsequent section, considering the intermolecular potentials.

Different temperatures of the sample can have a significant effect on the initial structure formation. A prominent example is the adsorption of PTCDA on $\text{Ag}(111)$ [65], where no LEED spots were observed for a deposition temperature of 110 K. Deposition between 147 K and 250 K resulted in the same pattern as for RT deposition, but with elongated spots. Figure 4.3 a) shows the effect of F_{16}CuPc deposition onto a substrate at 100 K. Considerably more molecules had to be deposited than at RT until LEED spots appeared. Even then the image still showed a very high diffuse background. This behavior is considerably different to the deposition at RT, where even submonolayers showed ordered structures when subsequently cooled down. Obviously, the adsorbate molecules do not have the possibility to diffuse on the surface at 100 K, or at least not

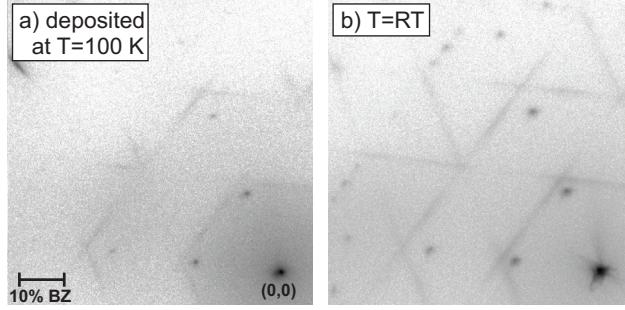


Figure 4.3: a) SPA-LEED image of $F_{16}CuPc$ after deposition onto a $Ag(111)$ crystal held at $T=100$ K and b) the same deposition after warming the sample up to RT. ($E = 30$ eV)

on the timescale of the experiment. Instead, they rather stick where they hit the crystal. This leads to large surface areas covered by disordered islands. The fact, that more molecules had to be deposited to observe LEED spots suggests that the adsorbate does not grow in a perfect layer-by-layer mode at this low deposition temperature. The reduced thermal energy of the molecules at LT seems to be insufficient to easily overcome the Ehrlich-Schwoebel barrier for diffusion across the island edges. Warming up the crystal to RT as seen in Fig. 4.3 b) results in a better ordered pattern resembling the normal monolayer pattern. The enhanced mobility enables the molecules to diffuse into a more favorable arrangement. Still the spots appear broader than those of a direct RT preparation, which could be a sign for smaller domain sizes of the superstructure.

In the following sections, the two different regions of the structural phase diagram will be analyzed in more detail.

4.2 Disordered submonolayer regime at RT

In this section, we will have a closer look at the regime of the disordered phase. Figure 4.4 shows a series of SPA-LEED images recorded during deposition of $F_{16}CuPc$ onto the bare Ag substrate at RT. The specular spot can be seen in the lower right corner. The first striking observation is, that the $(0,0)$ -spot intensity oscillates with coverage. The reason for this is the destructive interference in the two-layer system of substrate and adsorbate, which is strongest when both layers expose the same area to the electron beam, i.e. at a coverage of 0.5 ML. Constructive interference can only be observed if the wavelength of the electrons equals twice the step height d between the two layers, i.e. the adsorption height of the adsorbate molecules. The interference condition can be expressed by introducing the scattering phase S , which describes the phase difference in numbers of the electron wavelength λ_e as

$$S = 2d \cdot \cos(\varphi)/\lambda_e = 2d \cdot \cos(\varphi)\sqrt{E[eV]/150.4}. \quad (4.1)$$

4.2 Disordered submonolayer regime at RT

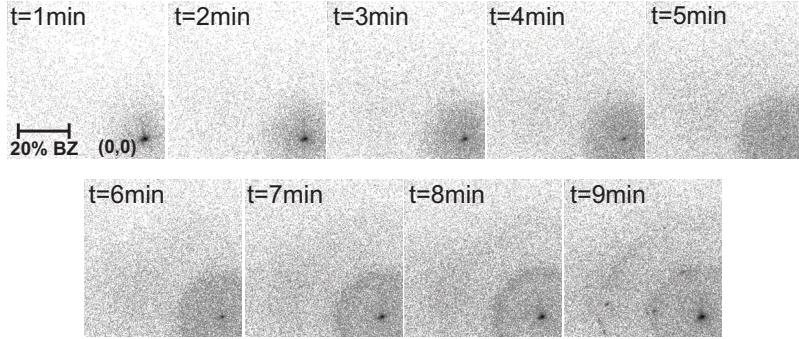


Figure 4.4: Sequence of SPA-LEED images recorded in-situ during deposition of $F_{16}CuPc$. ($E = 27.2$ eV)

Here, φ is the angle between the propagation direction of the incident electrons and the surface normal. For non-integer values of S , the interference will be at least partially destructive, like in the example shown here. The phenomenon of the $(0,0)$ -spot intensity dependence on coverage is equivalent to the well known *RHEED oscillations* [66]. The intensity of the $(0,0)$ spike can easily be observed already during deposition, which gives a first hint for the evaluation of the exact coverage. In the example in Fig. 4.4 the intensity of the specular spot was almost vanished after 5 minutes deposition, meaning that the coverage was close to 0.5 ML at this time. Superstructure spots appeared after 9 minutes, when the $(0,0)$ -spot intensity had almost reached a new maximum. Hence, the corresponding coverage must have been close to one monolayer. This coverage calibration is in agreement with STM measurements which show almost closed layers if the deposition is stopped just after the phase transition has been observed. Therefore we conclude that the disordered phase is formed for submonolayer coverages at RT. The critical coverage, for which the phase transition from the disordered to the ordered phase at RT occurs, is at $\Theta = (0.95 \pm 0.05)$ ML. With this knowledge, the deposited flux of molecules as given by the integrated ion current (IC) signal from the QMS, can be used to deposit any desired coverage in the (sub-)monolayer regime with rather high precision. The fact that for a coverage of 0.5 ML, approx. half of the amount of molecules have to be deposited than for the monolayer, shows that the sticking coefficient of $F_{16}CuPc$ on the Ag(111) surface does not change significantly during the growth of the 1st layer. This leads to the assumption that an $F_{16}CuPc$ molecule, impinging on an island or cluster of previously adsorbed $F_{16}CuPc$ molecules, is not more likely to desorb than a molecule which landed on the clean Ag surface. At RT, those molecules that initially arrive on top of islands can easily diffuse across the island step edges and enter the 1st layer. They hence have a similar probability to remain on the sample than molecules directly arriving on the Ag surface.

Intermolecular distances

The appearance and evolution of diffuse scattering intensity around the (0,0)-spot could be observed from the sequence of images in Fig. 4.4. This ring-like or disk-like intensity stems from the $F_{16}CuPc$ molecules and can be attributed to the absence of long-range ordered adsorbate structures. Since the intensity is uniform along the contour of the ring feature, the molecules do not adopt a preferred orientation for submonolayer coverages at RT. Instead, randomly oriented molecules are present on the surface, forming a dilute film. To quantify this finding, linescans through the (0,0)-spot and the rings have been recorded in Fig. 4.5 a) during deposition of $F_{16}CuPc$ on a freshly prepared surface.

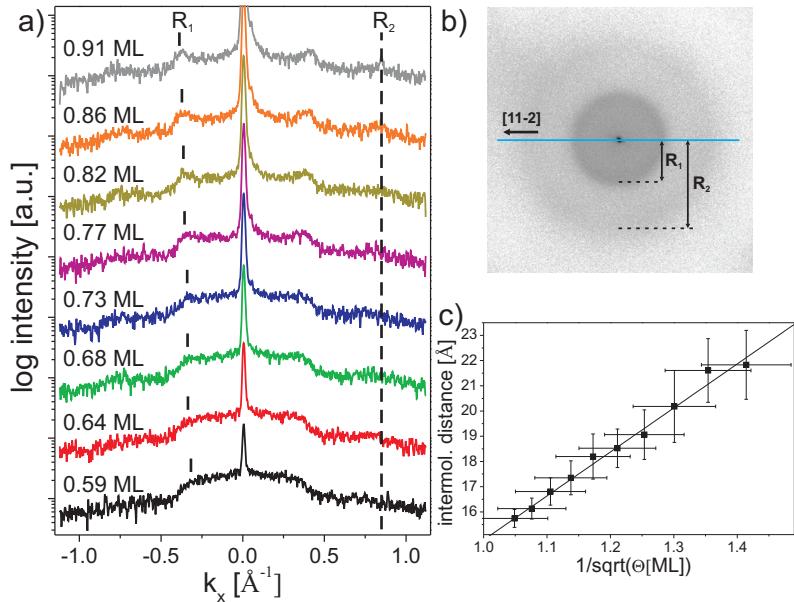


Figure 4.5: a) In-situ linescans recorded during deposition of $F_{16}CuPc$ along the direction indicated by the blue line in b). c) Dependence of the inner ring radius on $1/\sqrt{\Theta}$

For coverages below 0.55 ML the profile of the disk-like, diffuse intensity could be well fitted by a single Gaussian function. This scattering intensity is the result of a distribution of different intermolecular distances on the surface. The half width at half maximum (HWHM) of the Gaussian fitting the disk-like intensity can be related to a characteristic real space distance \bar{R} via

$$\bar{R} = \frac{2\pi}{\text{HWHM}}. \quad (4.2)$$

As the radius of the disk increased, the according real space distance $\bar{d} = 2\pi/\bar{R}$

4.3 Structural investigation of the ordered phase

decreased from $\approx 26.6 \text{ \AA}$ to $\approx 21 \text{ \AA}$ between 0.14 ML and 0.55 ML. Intermolecular distances around these values occurred without specific cumulation.

When the coverage was increased to values above 0.55 ML, the diffuse intensity gradually became more ring-like. In the linescans, this ring manifested as two peaks, one on each side of the (0,0)-spot. The ring radius R_1 was evaluated by fitting the according peak positions. Generally such a feature represents a prominent distance in reciprocal space which can be attributed to a frequent real space distance [67]. When the ring-like diffraction feature appeared, a preferred intermolecular distance

$$d_1 = 2\pi/R_1 \quad (4.3)$$

between the adsorbate molecules had developed, while there was still rotational disorder. The increase in radius can be explained by a decrease of this distance as the surface was filled with more and more molecules. Between 0.59 ML and 0.91 ML, d_1 decreased from $(20.2 \pm 1.4) \text{ \AA}$ to $(15.7 \pm 0.4) \text{ \AA}$. The peak width decreased with increasing coverage, which shows that the preferred distance becomes better defined as the molecules have less space to diffuse on the surface. As a result, the error bar for d_1 also decreased. These results indicate that F₁₆CuPc forms a dilute film covering the complete Ag(111) surface. Instead of clustering to islands, the molecules maximize their distance as far as sterically possible. Figure 4.5 c) illustrates, that the intermolecular distance is proportional to $1/\sqrt{\Theta}$. This is expected since for adsorbate films which cover the whole surface, the inverse coverage corresponds to the area per molecule, which is in turn proportional to R_1^2 .

The second, outer ring is less intense and does not represent the second order of the first ring, since its radius R_2 does not depend on the coverage within the limits of measurement accuracy. The corresponding real space distance is $d_2 = 8.3 \pm 0.4 \text{ \AA}$ and might be attributed to intramolecular scattering.

A disordered phase with a decreasing intermolecular distance upon coverage increase is a typical feature for phthalocyanines on noble metal fcc surfaces. Similar features have been found for CuPc [45], SnPc [8], TiOPc [33], H₂Pc [64] and FePc [68] on Ag(111), as well as for CuPc on Au(111) and on Cu(111) [46].

Only for coverages $\Theta > 0.9 \text{ ML}$, the F₁₆CuPc molecules start to arrange into ordered structures when their movements are restricted due to sterical reasons. The preference for disordered arrangements can either be an entropical effect or a sign for a weak repulsive intermolecular interaction, as it is also the case for other phthalocyanines. In the case of F₁₆CuPc, an intermolecular repulsion might be expected due to the negative partial charges at the terminating fluorine atoms.

4.3 Structural investigation of the ordered phase

SPA-LEED images of the ordered F₁₆CuPc phase on the Ag(111) surface consist of spots arising from three rotational domains and possibly from mirror domains. Intensities of equivalent spots from different domains are comparable, indicating

that none of the domains is preferred. The shape of superstructure spots generally allows first conclusions about the adsorbate layer. Here, the superstructure

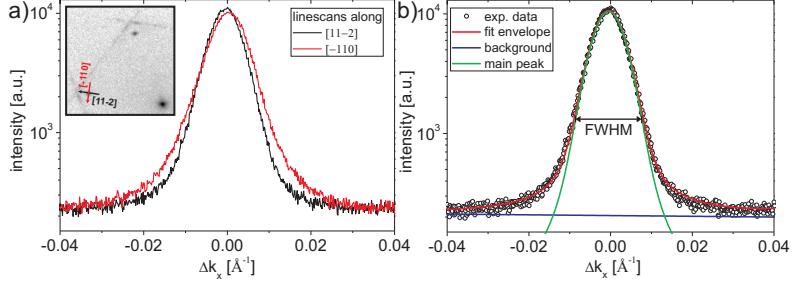


Figure 4.6: a) Linescans through a spot of the $F_{16}CuPc$ superstructure at two different angles showing a slight asymmetry. b) Fit model for the linescans using a Voigt function for modeling the superstructure peak

domains are rather large and the density of domain boundaries is only slightly anisotropic. This could be extracted from the peak widths determined from linescans through the superstructure spots. A representative example is shown in Fig. 4.6 at $E = 30$ eV. As indicated in the inset of the figure, two linescans, perpendicular to each other, have been recorded to reveal a slight asymmetry of one of the hexagonal superstructure spots. Generally, superstructure LEED spots are broadened due to finite domain sizes D , which can be estimated from the FWHM of the peaks via

$$D = \frac{2\pi}{\text{FWHM}}. \quad (4.4)$$

For the example in Fig. 4.6, the peaks were modeled by a Voigt function and yielded an average domain size of 700 Å for the linescan along $[11\bar{2}]$ and 624 Å along $[\bar{1}10]$, respectively. Both values are above the effective transfer width of the SPA-LEED instrument, which was specified as $T_{\text{eff}} \approx 500$ Å in section 2.1. This shows, that the superstructure is not or at least not strongly affected by the mosaicity of the sample, which limits T_{eff} . Typically, adsorbate domains in the 1st molecular layer are not expected to grow over step edges and are thus not larger than the terrace size. We can conclude that only one $F_{16}CuPc$ superstructure domain is formed on each Ag terrace.

Annealing effect

In many cases, the ordering of adsorbate molecules on a substrate can be improved by annealing the sample. The increased mobility due to thermal energy enables the molecules to overcome smaller potential barriers and find a global adsorption minimum. Different annealing temperatures have been tried for $F_{16}CuPc$, as visualized by the exemplary SPA-LEED images in Fig. 4.7. It

4.3 Structural investigation of the ordered phase

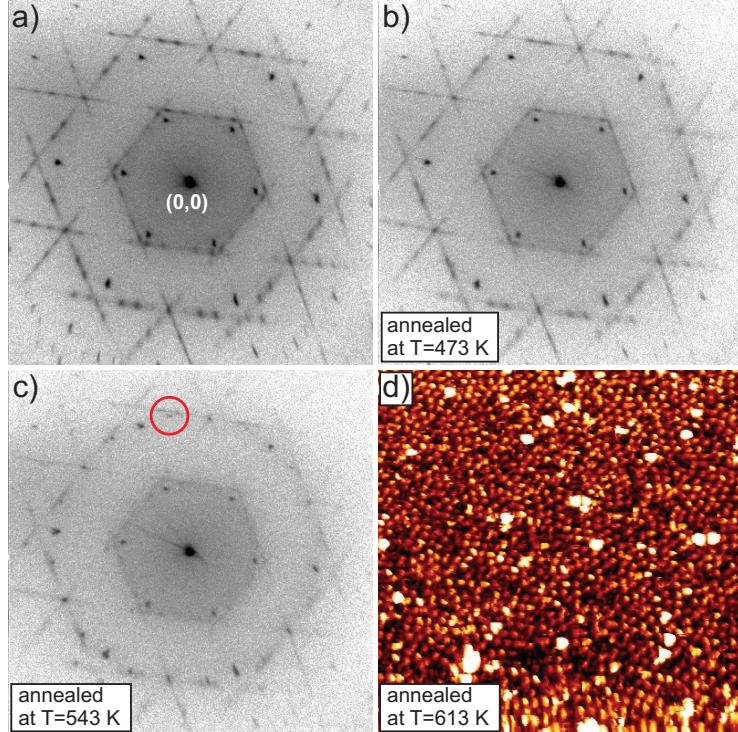


Figure 4.7: Effect of annealing on a monolayer of $F_{16}CuPc$ on $Ag(111)$: LEED patterns were taken at RT a) as prepared, b) after annealing at $T = 473$ K and c) after annealing at $T = 543$ K. d) An STM image after annealing at $T=613$ K shows that the surface is still covered by a disordered layer.

was found that annealing up to a temperature of $T = 473$ K has no significant impact on the structure formation. Annealing at even higher temperatures resulted in a less ordered structure. In Fig. 4.7 c), the sample was heated up to 543 K. This resulted in a superposition of the ordered monolayer LEED pattern with a diffuse intensity that was somewhat similar to the rings seen at lower coverages. Two faint rings could be observed with radii almost equal to the distance between the specular spot and the 1st and 2nd of the intense spots of the hexagonal superstructure. The intensity of these rings was not uniform as some new spots along the ring could be found (e.g. red circle in Fig. 4.7 c)). This means that a part of the surface had become rotationally disordered as an effect of the annealing, but some preferred angles existed.

Gradually increasing the temperature further lead to a complete loss of order in the adsorbate layer. As no QMS signal was observed for annealing a monolayer structure up to 673 K, this can not be due to a reduction of the coverage

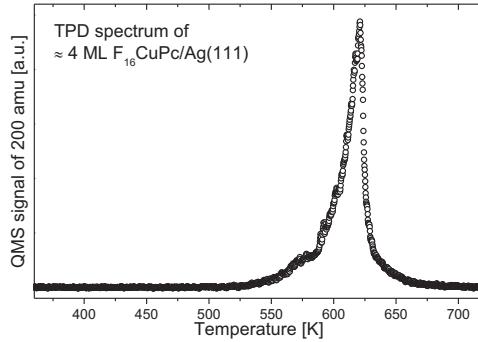


Figure 4.8: TPD spectrum showing the signal of 200 amu at a heating rate of 1 K/s. The sample was covered by ≈ 4 ML $F_{16}CuPc$.

caused by thermal desorption of molecules. On the other hand when annealing a multilayer film, QMS intensity was found for $T > 523$ K, as shown in the TPD spectrum in Fig. 4.8. This indicates that higher layers are more weakly bonded and can be thermally desorbed. The spectrum dropped rapidly beyond the peak temperature of $T \approx 620$ K. However it did not completely drop to background but ended in an exponentially decreasing tail. Therefore the total desorption process is not simply described by zero-order or first-order kinetics. Instead, the shape of the curve might be explained by components from higher layers, following zero-order kinetics, and from the 2nd layer with a higher desorption energy, following higher order kinetics. The first layer does not desorb at $T < 673$ K, but becomes disordered. The STM image in Fig. 4.7 d) shows such an $F_{16}CuPc$ film after annealing up to $T = 613$ K. Depositing additional molecules on top of a disordered monolayer did not restore the order, neither did cooling. These results indicate that the molecules in the 1st layer are probably destroyed rather than desorbed by annealing.

A gradual loss of order in the $F_{16}CuPc$ film could also be clearly observed when the sample was scanned by SPA-LEED for ≥ 2 h. Obviously beam damage is considerably strong for $F_{16}CuPc$ on $Ag(111)$, even at the rather low electron beam intensities used in SPA-LEED. 2D diffractograms shown in this chapter were therefore typically scanned over ≈ 1 h.

4.3.1 LEED model

From the arrangement of LEED spots, the structure of an adsorbate can be evaluated. Therefore, LEED spots for different structural models have been calculated and compared to the measured pattern, until a satisfying agreement was achieved. The left side of Fig. 4.9 shows a SPA-LEED image of the ordered phase at LT. Single SPA-LEED scans have been summed up for ≈ 1 h to achieve good statistics. On the right side, the same image is shown superimposed with

4.3 Structural investigation of the ordered phase

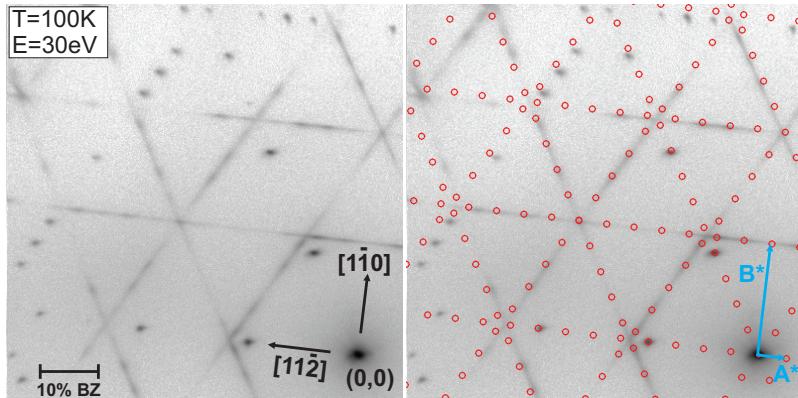


Figure 4.9: a) Ordered $F_{16}CuPc$ structure at $T=100$ K; Crystallographic directions of the Ag substrate are indicated. b) shows the same image including calculated spots from a structural model (red circles). Reciprocal unit cell vectors are indicated by the blue arrows.

spots calculated for our final unit cell model. This unit cell is rectangular and well oriented along the substrate, with the smaller unit cell vector in reciprocal space A^* being aligned along one of the Ag $\langle 11\bar{2} \rangle$ high symmetry directions. Two facts can be observed from the inspection of the image:

- Spots located on lines parallel to A^* and passing through the $(0,1)$ and $(0,2)$ superstructure spots are smeared out to streaks, so that the three rotational domains together form two hexagon-like features. However, maxima can clearly be seen within the streaks.
- Only every 4th spot of the LEED model along the vector A^* is visible in the measured image.

The LEED model describes the positions of the strong hexagonal spots as well as the spots (maxima) within the streaks. Whether the unit cell is commensurate or incommensurate could not be definitely distinguished. In Fig. 4.9, a commensurate unit cell described by the matrix

$$M = \begin{pmatrix} m_{11} & m_{12} \\ m_{21} & m_{22} \end{pmatrix} = \begin{pmatrix} 21 & 0 \\ 3 & 6 \end{pmatrix} \quad (4.5)$$

was applied and will be used in the following. In real space, the length of the unit cell vectors are $|\vec{A}| = 60.69 \text{ \AA}$ and $|\vec{B}| = 15.02 \text{ \AA}$, and the unit cell area is 911.37 \AA^2 . However, due to the large size and the streaky as well as the extinguished spots, unusually high error bars of $\Delta m_{11} = 0.5$ and $\Delta m_{21} = \Delta m_{22} = 0.2$ must be taken into account for the matrix elements. One argument for a commensurate structure is that LEED spots are visible up to rather high orders, which is usually not the case for incommensurate structures. The occurrence of the zero matrix element $m_{12} = 0$ means that unit cell vector \vec{A} is aligned

along an $\langle 01\bar{1} \rangle$ direction, and consequently, that the unit cells of mirror domains coincide with rotational domains for this structure. We have further set $m_{21} = 2 \cdot m_{22}$, ensuring that \vec{B} is along a $\langle 11\bar{2} \rangle$ direction. These two criteria have to be met also if an incommensurate unit cell is applied to the structure. The observed streaks are not described by the LEED model, but the positions of maxima along the streaks agree well with spot positions in the model.

4.3.2 STM measurements

To explain the two striking observations from the LEED pattern (spot extinctions and streaks), STM measurements have been performed and will be discussed in the following. At room temperature, the molecules were too mobile to be imaged with STM, when the coverage was still in the disordered submonolayer regime. In LT images like Fig. 4.10 a) on the other hand, the predicted

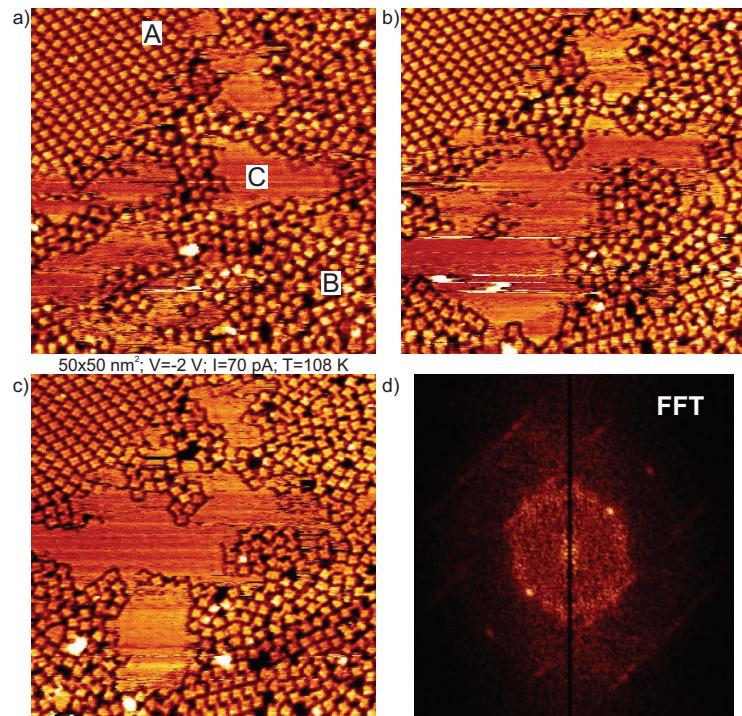


Figure 4.10: a–c) Subsequently recorded STM images (not distortion corrected) of $F_{16}CuPc$ /Ag(111) at submonolayer coverage and $T=108$ K. Disordered regions and islands coexist on the surface. d) A 2D-FFT of the image mainly resembles the diffuse ring-like intensity already seen in LEED.

4.3 Structural investigation of the ordered phase

islands (marked with "A") could clearly be seen at submonolayer coverages. The adsorbate film was not perfectly ordered, since a large part of the surface was still covered with disordered molecule clusters (region "B") that aggregated to ordered islands in some regions. The areas in between (region "C") appeared empty, but probably contained a low density of very mobile molecules that were moved by the tip during scanning. This can be judged by the apparent height in this region which was the same as the height of the molecules in the ordered areas. As a consequence of the mobility of the molecules, which was still considerably high, the disordered regions changed continuously during scanning. This could easily be seen by scanning the same region multiple times as done in Fig. 4.10 a)–c). A two-dimensional fast Fourier transform (2D-FFT) of the first image is dominated by a ring-like feature representing the disordered regions, as shown in Fig. 4.10 d). The molecules are rotationally disordered, but their intermolecular distance is rather well defined. Hence the FFT resembles the diffuse LEED images of the submonolayer phase at RT. The FFT is slightly distorted, since the distortion in the STM image has not been corrected. Some spots and faint streaks are also present in the FFT, originating from the island in the upper left of the STM image. These features are similar to the ordered SPA-LEED image, if one considers that only one of the three rotational domains is present in the imaged surface area.

If more molecules were deposited onto the crystal, the fraction of ordered regions at LT increased, until the layer was closed. When the coverage was close to one monolayer, the same ordered structure could also be imaged at RT. Figure 4.11 shows three equivalent domains, located on different terraces and

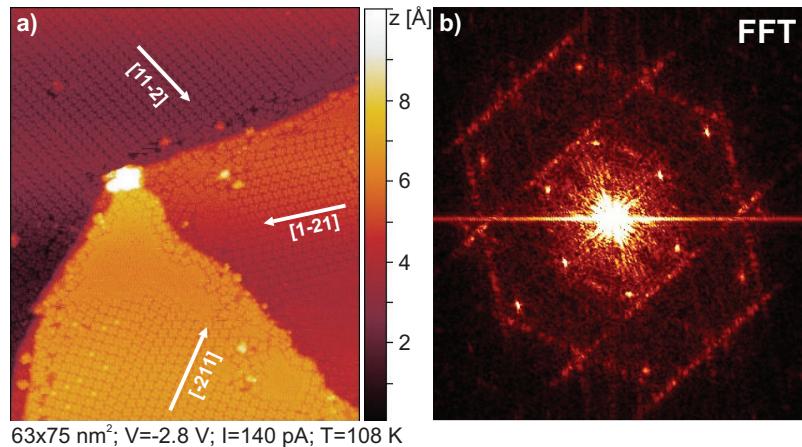


Figure 4.11: a) Islands of three rotational $F_{16}CuPc$ domains, located on different terraces, demonstrate the influence of the hexagonal substrate symmetry. b) A 2D-FFT of the image is in excellent agreement with the SPA-LEED results.

rotated against each other by 120° . Thus, the formation of ordered adsorbate structures is influenced by the three-fold substrate symmetry. Again, STM image and its 2D-FFT are slightly distorted. Nevertheless, the FFT agrees very well with the SPA-LEED data of the ordered phase. This confirms that the STM images are representative of the typical adsorbate structure.

The degree of accordance between the SPA-LEED and the STM results could be quantified further by comparing linescans through the LEED pattern and FFT of STM images. Figure 4.12 shows linescans (black curves in c) and d)),

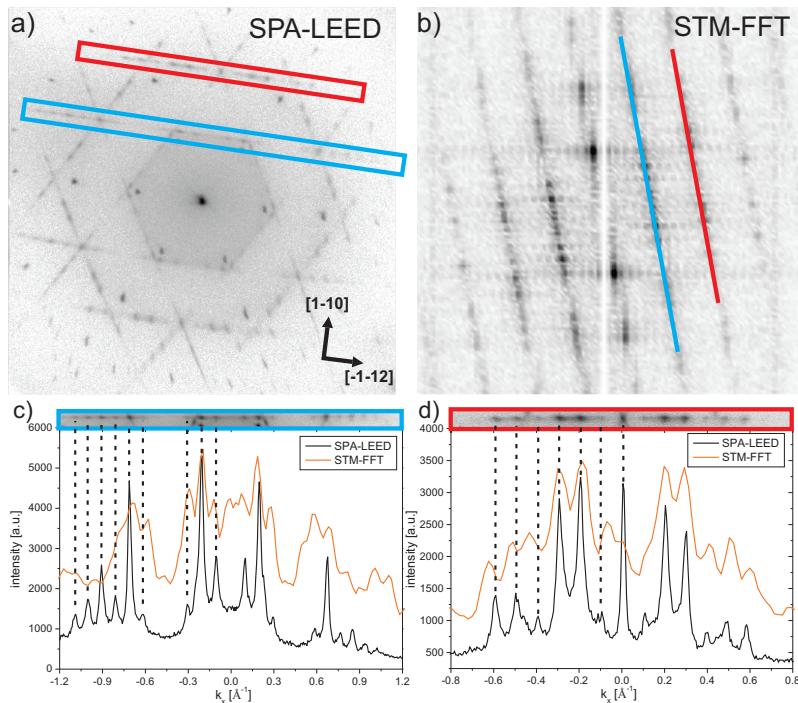


Figure 4.12: Comparison of a) SPA-LEED and b) STM-FFT results. In the regions marked in blue and red, linescans along the streaks have been recorded for both methods, as shown in c) and d).

recorded along the streaks through the $(0,1)$ and $(0,2)$ spots of the superstructure as marked by the red and blue rectangles in a). The better statistics in the linescans helps to identify the rather weak spots. Also, it is confirmed that some spots are extinguished and not just weak, as can be seen for example in the 1st order scan around $k_x = \pm 0.45 \text{ \AA}^{-1}$. These linescans are compared with linescans through the according regions of an FFT of an STM image (orange curves). A good qualitative agreement between SPA-LEED and STM-FFT is found in most cases in particular regarding the peak positions.

4.3 Structural investigation of the ordered phase

The structure formation of the molecules was further analyzed by STM as discussed in the following. An image of a single rotational F_{16}CuPc domain is shown in Fig. 4.13. It can be seen, that the domain consists of molecular rows

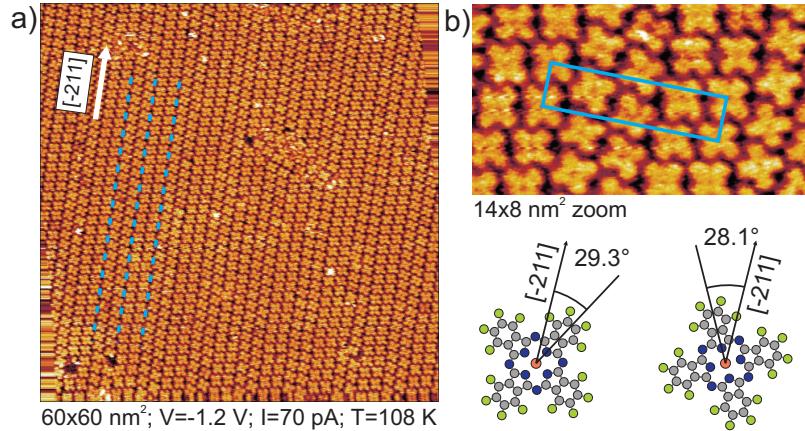


Figure 4.13: a) Drift corrected STM image of a large F_{16}CuPc island showing rows of well ordered molecules that are aligned with the silver substrate. Domain walls, indicated by the dashed lines, are found every second row. b) shows a closeup including the proposed unit cell drawn in blue. The measured in-plane angles within the two types of rows (domains) are given below.

along which all molecules adopt the same in-plane rotation angle and a well defined intermolecular distance. Except for some point defects or small defect regions, the molecular layer was well ordered. The cloverleaf-like shape of the molecules was nicely resolved with the center of the molecules appearing as a depression for both imaging at positive and at negative bias voltages. The reason is that the the molecular orbitals close to the Fermi-level, which dominate the LDOS contrast, have no significant occupation probability at the central copper atom. This can be seen from the DFT calculations for free molecules in the gas phase, shown in Fig. 4.1. Hence, the apparent height in the STM images does not represent the topology of the molecules. Apparent depressions at the molecular center are also commonly found for other planar phthalocyanine molecules on metal substrates (e.g. $\text{ZnPc}/\text{Ag}(111)$ [69], $\text{NiPc}/\text{Au}(111)$ [70]), for which there is also no considerable occupation probability of electrons in molecular states near the Fermi-level at the metal atom.

Neighboring rows of F_{16}CuPc were always glided against each other along a $\langle\bar{2}11\rangle$ direction of the substrate and two different molecular orientations appeared within an island as shown in Fig. 4.13. In most cases, the in-plane angle changed every second row, so that a pair of rows will be called a row domain in the following with domain walls (marked by the dashed lines) where the in-plane angle changes. A segment of four rows can be described by a glide mirror sym-

metry with a domain wall acting as the symmetry axis. Therefore, a repeating unit that describes most of the surface expands over one molecule along the rows and over four molecules in the perpendicular direction, i.e. $\langle 01\bar{1} \rangle$. This fits nicely to the dimensions found for the LEED unit cell (see discussion of the adsorption model below).

The dislocations and different rotations of the molecules within the rows are probably induced by a mismatch between the substrate lattice and the favored intermolecular arrangement, given by intermolecular potential minima. If the molecules are forced to arrange in formations that are unfavorable with respect to their intermolecular interactions, the adsorbate layer is stressed. As a consequence, regular dislocations may appear, which minimize the surface tension of the film. In other systems, this results in defect lines, i.e. an increased distance between two rows. If such regular dislocations are not found, it might be that one of the two interactions (molecule–substrate or intermolecular) is very dominant, or that the optimum intermolecular geometry matches a commensurate surface registry by chance. In the case of $F_{16}CuPc$ on Ag(111), the molecule–substrate interaction is physisorptive or weakly chemisorptive, so that the molecule–molecule interaction strength could be in the same order of magnitude. However, the high density of domain walls observed in STM indicates a considerable mismatch to the substrate lattice.

Spot extinctions

The structure found here, which consists of a repeating unit of four rows, is the reason for the spot extinctions in LEED as will be discussed in the following. The structure factor F of the unit cell can be calculated as the sum of the scattering factors of the four molecules inside the cell. The nomenclature is explained in Fig. 4.14, the calculation is performed in equation 4.6.

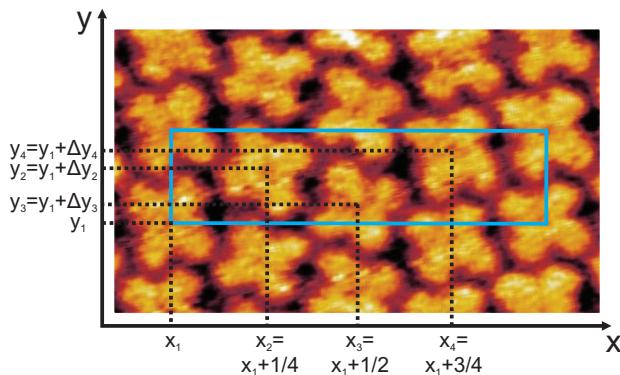


Figure 4.14: Nomenclature for the structure factor calculations. Equal distances of the four molecules inside the unit cell are assumed.

4.3 Structural investigation of the ordered phase

$$\begin{aligned}
F &= \sum_j f_j \cdot e^{-2\pi i G r_j} = \sum_j f_j \cdot e^{-2\pi i (hx_j + ky_j + lz_j)} \\
&\approx f \cdot e^{-2\pi i l z} \left[e^{-2\pi i (hx_1 + ky_1)} + e^{-2\pi i (h(x_1 + 1/4) + k(y_1 + \Delta y_2))} \right. \\
&\quad \left. + e^{-2\pi i (h(x_1 + 1/2) + k(y_1 + \Delta y_3))} + e^{-2\pi i (h(x_1 + 3/4) + k(y_1 + \Delta y_4))} \right] \quad (4.6) \\
&= f \cdot e^{-2\pi i (hx_1 + ky_1 + lz)} \left[1 + e^{-2\pi i (1/4h + \Delta y_2 k)} \right. \\
&\quad \left. + e^{-2\pi i (1/2h + \Delta y_3 k)} + e^{-2\pi i (3/4h + \Delta y_4 k)} \right]
\end{aligned}$$

Here $G = (h, k, l)$ is the reciprocal lattice vector and $r_j = (x_j, y_j, z_j)$ is the position vector of the molecule j within the unit cell. $\Delta y_j = y_j - y_1$ describes the dislocation of the molecule $j = 2\dots4$ in the y -direction (i.e. one of the $\langle\bar{2}11\rangle$ directions) compared to molecule 1. In x -direction (i.e. $\langle01\bar{1}\rangle$), a perfect periodicity with equal distances of $1/4$ of the unit cell length between neighboring molecules is assumed. The form factors f_j of the molecules are further assumed to be equal, which is not exactly true, since e.g. the molecules have different in-plane orientations. Nevertheless this should be a valid approximation considering that the F₁₆CuPc molecules are rather symmetric, flat lying objects. The spots along the direction of A^* are reflected by the case of $k = 0$, i.e. zero order of B^* . Structure factors for some exemplary values of h are calculated in equation 4.7.

$$\begin{aligned}
k = 0, h = 0 : [...] &= 1 + e^{-2\pi i \cdot 1/4h} + e^{-2\pi i \cdot 1/2h} + e^{-2\pi i \cdot 3/4h} = 4 \\
k = 0, h = 1 : [...] &= 1 + e^{-1/2\pi i} + e^{-\pi i} + e^{-3/2\pi i} = 0 \\
k = 0, h = 2 : [...] &= 1 + e^{-\pi i} + e^{-2\pi i} + e^{-3\pi i} = 0 \quad (4.7) \\
k = 0, h = 3 : [...] &= 1 + e^{-3/2\pi i} + e^{-3\pi i} + e^{-9/2\pi i} = 0 \\
k = 0, h = 4 : [...] &= 1 + e^{-2\pi i} + e^{-4\pi i} + e^{-6\pi i} = 4
\end{aligned}$$

As can be seen, the structure factor is zero for $h = 1$, $h = 2$ and $h = 3$ and non-zero for multiples of 4. This explains why only every fourth spot along A^* is not extinguished. Hence the extinctions are a result of the well defined, equidistant intermolecular separations in x -direction, representing the inter-row distance. For the higher orders of B^* , i.e. for $k = 1$, $k = 2$ etc., the calculations are more complicated, especially since the values of the dislocations Δy_j are not so well defined. The shifts between neighboring rows are not always the same in every four-row-segment. Hence, the proposed unit cell does not describe the structure perfectly. The less well defined periodicity along the high symmetry directions $\langle01\bar{1}\rangle$ qualitatively explains that many LEED spots are smeared out to streaks, which is not represented by a single unit cell. Still, our proposed unit cell describes the *dominant* part of the structure, since the LEED model spots fit to the positions of the maxima along the streaks.

Real space model

The spot extinctions described above and the sharpness and intensity of the hexagonal spots indicate that the inter-row distance is well defined despite of

any dislocations or different angular orientations. Therefore, we know from the SPA-LEED results that

- the intermolecular distance along the rows is $d_y = |\vec{B}| = 15.02 \text{ \AA}$, while
- the inter-row distance is $d_x = |\vec{A}|/4 = 15.17 \text{ \AA}$.

These very accurate numbers can be used to correct the distortions in the STM images due to thermal drift, imperfect piezo settings etc. From the corrected images, the in-plane orientations of the $F_{16}CuPc$ molecules in the two different row domains can be quantified. The results are angles of $(28.1 \pm 3)^\circ$ and $(29.3 \pm 3)^\circ$ between the axis along opposite wings of the respective molecule and the $\langle\bar{2}11\rangle$ substrate directions as illustrated in Fig. 4.13. These numbers indicate that within error bars, the wings are aligned along high symmetry substrate directions.

Combining the results from SPA-LEED and STM, we arrive at an adsorption model as presented in Figure 4.15. The rectangular unit cell is drawn in blue

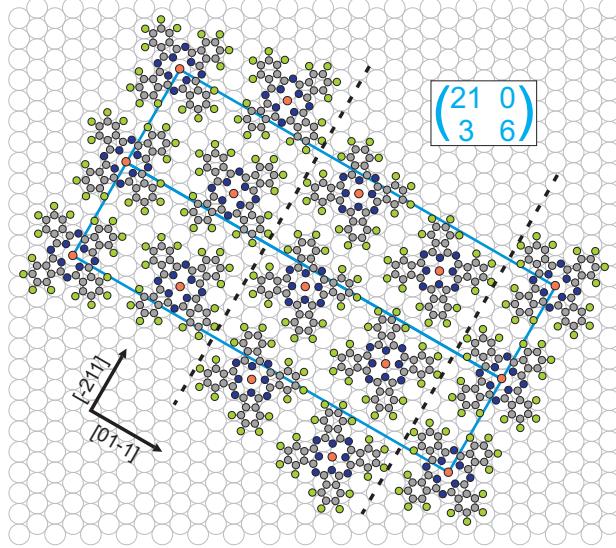


Figure 4.15: Real space model for the monolayer structure of $F_{16}CuPc$ on $Ag(111)$. The unit cell (blue rectangle) is known from the LEED results while the in-plane rotations and relative orientations of the molecules have been estimated from STM experiments. Domain walls are indicated by the black dashed lines. The adsorption sites of the molecules are arbitrarily chosen.

on the lattice of the Ag surface. Four $F_{16}CuPc$, visualized by ball-and-stick models, are placed in the unit cell at relative positions according to the STM results with domain walls given by the black dashed lines. While the in-plane angles of the molecules relative to the substrate are also known from STM,

4.3 Structural investigation of the ordered phase

the exact adsorption sites are unknown and have been chosen arbitrarily in the model. This model represents the predominant structure for the adsorption of F₁₆CuPc islands on Ag(111), although units of different periodicity along $\langle 01\bar{1} \rangle$ also occur, as described above.

The structure found here is essentially the same as reported previously by Huang et al. [59]. However, these authors proposed a unit cell with a superstructure matrix of $\begin{pmatrix} 20 & 0 \\ 3 & 6 \end{pmatrix}$ based on STM and LEED. The discrepancy to our results is easily explained, since SPA-LEED allows measuring unit cells with a much higher precision than a conventional LEED or an STM.

4.3.3 Origin of the structure formation

Pair potential calculations have been performed to model the intermolecular interactions between two F₁₆CuPc molecules, similar to the calculations for SnPc described in chapter 3. The results can easily explain the intermolecular repulsion observed for the submonolayer RT phase, as seen in Fig. 4.16 a). The

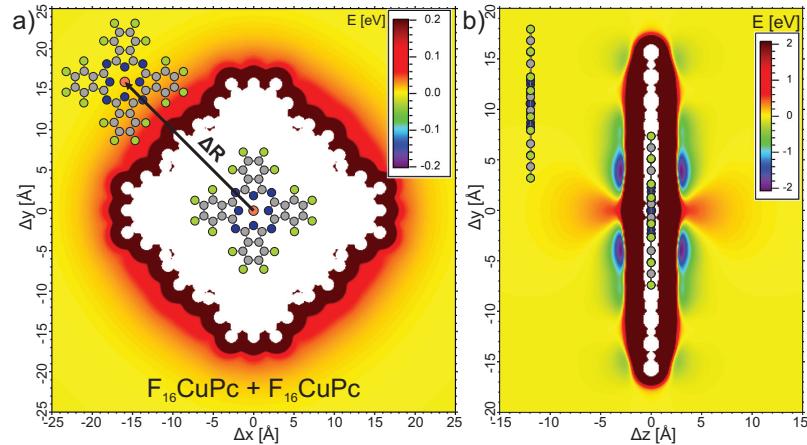


Figure 4.16: Pair potential calculations for two F₁₆CuPc molecules in a) lateral and b) stacked geometry. Attractive and repulsive regions are represented by the blue and red colored regions, respectively.

map shows the pair potential for two identically oriented and laterally displaced molecules on the same height ($\Delta z = 0$). While the first molecule was fixed in position, the second one was scanned across the x/y plane with a step size of 0.1 Å. The color code displays the resulting potential energy at each point as seen in the legend of the figure. Only regions of positive potential are found, representing energetically unfavorable geometries. Different relative in-plane angles of the molecules from 0° to 90° in steps of 1° were tried but also yielded strictly repulsive results. The potential approaches its minimum of zero as the intermolecular distance increases. This qualitatively explains the observations

for the low coverage regime at RT described above. Due to the intermolecular interactions considered in the calculations, the molecules do not cluster to ordered structures but tend to distribute evenly across the sample surface to maximize their distance. This manifests in the ring structure observed in LEED. When the coverage increases, the average intermolecular distance decreases. Above a certain critical coverage, the rotations and movements of the molecules are sterically hindered, forcing them to arrange in ordered structures. Each additional molecule that adsorbs in the first layer results in a more unfavorable situation regarding the intermolecular potentials as the average intermolecular distance decreases, leading to stronger repulsion. The energy gain for the total substrate/adsorbate system must therefore be the result of molecule–substrate interactions, described by the adsorption energy of the molecules. When the maximum coverage in the first layer is reached, it becomes more favorable for additional molecules to adsorb in the 2nd molecular layer. The same mechanism is true for other phthalocyanines showing repulsion at RT. Compared to CuPc, an $F_{16}CuPc$ film can reach a lower critical molecular density on Ag(111) before adsorption in the 2nd layer starts. This is apparent from the area per molecule of the corresponding monolayer unit cells, which is 191.6 \AA^2 for CuPc [45] and 227.8 \AA^2 for $F_{16}CuPc$, respectively.

A repulsive intermolecular interaction dominates the adsorbate arrangement at RT. When the system is cooled down on the other hand, the molecules form ordered structures already in the submonolayer regime. This means that the molecules cluster to islands, as was confirmed by STM. Hence, their total interaction must be switched to attraction. Obviously a new balance of forces has arisen as a consequence of the reduced temperature.

A similar behavior was found by Kröger et al. [45] for the structure formation of CuPc on Ag(111). The CuPc molecules also show repulsion at RT and attractive interaction at LT leading to island formation. In contrast to $F_{16}CuPc$, the pair potential map of two CuPc molecules shows small attractive regions [32, 33]. Kröger et al. explained that these minima represent shallow local potential minima. At RT, the thermal energy of the CuPc molecules is high enough to overcome the diffusion barriers and cross the potential wall in the direction of increasing distances. At LT on the other hand, the molecules can become trapped in the local minima, resulting in island formation.

In case of $F_{16}CuPc$ on Ag(111) the situation is different. The pair potential map shows only strictly repulsive regions, so that no attractive local minima exist due to intermolecular interactions considered in our calculation. However, the fact that the structure formation behavior is rather similar to CuPc/Ag(111) suggests that the energy environment of the $F_{16}CuPc$ molecules should also be similar.

An idea to explain this problem was found by calculating the pair potential maps separately for electrostatic potential and van-der-Waals potential. Fig. 4.17 a) shows a map of the electrostatic potential between two equally oriented $F_{16}CuPc$ molecules. The arrows indicate distance vectors to the nearest neighbors along the row direction, i.e. $\langle\bar{2}11\rangle$ as they were found in the experi-

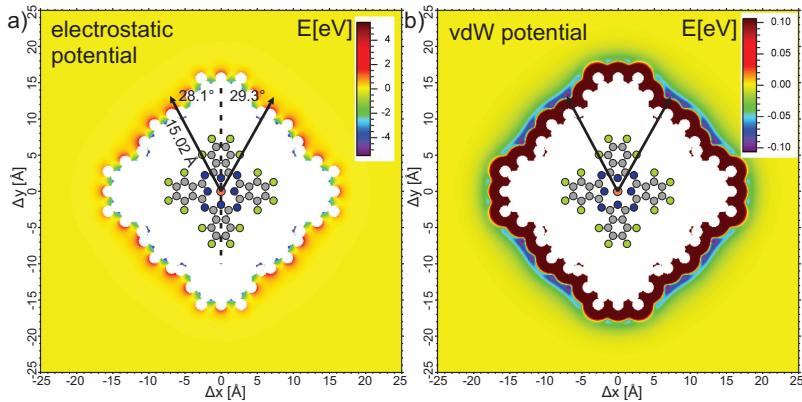


Figure 4.17: Pair potential calculation for two F_{16}CuPc molecules, considering a) only electrostatic and b) only van-der-Waals interactions. The arrows indicate distance vectors to the nearest neighbors along the rows.

ment. The absolute value of the vectors of 15.02 \AA was taken from SPA-LEED as described above, while the angles between the molecular diagonal and $\langle\bar{2}11\rangle$ were measured in Fig. 4.13 b). It can be seen that the vectors clearly end in repulsive electrostatic potential regions. The electrostatic interaction becomes attractive only for rather small intermolecular distances, for which in turn the van-der-Waals potential is strongly repulsive due to the Pauli repulsion, as seen in Fig. 4.17 b). Therefore, the total potential of electrostatics + van-der-Waals, which was already shown in Fig. 4.16, does not contain any attractive regions. However, in Fig. 4.17 b) it is striking, that the distance vectors end almost exactly in local minima of the van-der-Waals potential. It is unlikely that this is mere coincidence. It seems that the actual potential landscape at LT is rather well described by the van-der-Waals potential minima.

Possible explanations would be that either

- the electrostatic repulsion is decreased at LT, or
- an additional attractive interaction exists, which is not included in the calculations, or
- the used vdW parameters (see Table 2.1) are not correct.

In the first two cases, the effect (additional interaction or weakened electrostatic interaction) does not necessarily occur at LT only. It can also be present at RT, where the thermal energy of the molecules is too high for a trapping of the molecules in potential minima in analogy to the argumentation for CuPc.

Charge transfer between adsorbate and substrate is a common phenomenon that can lead to different distributions of partial charges in the molecules and considerably alter the electrostatic interactions. This is a possible reason for the

discrepancy between the experiment and our calculations. However, the adsorption heights of carbon (3.25 Å) and fluorine (3.45 Å) atoms in F₁₆CuPc/Ag(111) measured by Gerlach et al. via XSW [61] rather indicate physisorption than chemisorption. Hence, a large overlap of van-der-Waals radii with the substrate atoms appears unlikely.

On the other hand, the same authors report a strong upward bending of the fluorine atoms in the molecule, based on different coherent positions and a small coherent fraction of the C atoms of $F^H(C) = 0.41$. These results point to a bending of the adsorbed molecules that is not the case for free F₁₆CuPc molecules. Such a strong deformation is usually only observed on strongly interacting surfaces. For F₁₆CuPc on Cu(111) [61], an even stronger bending of the molecules was found, while the molecules remain flat on Au(111) [71]. As the degree of bending scales with the adsorbate–substrate interaction strength (increasing from Au to Ag to Cu), the reason seems to be either a direct interaction between the fluorine atoms and the substrate or a substrate mediated interaction. Gerlach et al. proposed that the upward bending of the fluorines could be due to partial rehybridization of the carbon atoms from sp^2 to sp^3 upon adsorption, which would change the C-F bonding angle. Since adsorption heights for nitrogen and copper are not available, a reasonable pair potential calculation for a bent geometry similar to the SnPc calculation in chapter 3 could not be done. However, it is obvious that rehybridization as well as a strong bending of the molecule can have a significant influence on the electrostatic and van-der-Waals interaction, which might explain the observed contradiction of experimental and theoretical finding. Most likely it is not only a mere upward bending of the fluorine atoms, since this would only induce a small vertical dipole moment, which in turn adds an additional repulsive contribution to the intermolecular potential.

It can be speculated further about another effect explaining the molecular bending. In an LDA-DFT study on atomic fluorine adsorption on metal surfaces [72], it was found that a positively charged F⁺ ion will be bound more weakly and with a larger equilibrium distance to the surface than an F⁻ ion, which is the typical adsorption state. This was found to be the result of a reduced image charge attraction due to screening and of an increased Pauli repulsion. These results should be transferable to some degree to molecular adsorbates containing fluorine atoms. A charge transfer from the fluorine end groups to other parts of the molecule or to the substrate could explain the bent geometry with the F atoms pointing away from the surface due to similar mechanisms. Such a charge transfer might be responsible for a change of the interaction potential landscape, leading to lateral attraction between F₁₆CuPc molecules.

The 3rd possible reason for the discrepancy between experiment and calculations could simply be a wrong set of vdW parameters. These parameters were mainly taken from literature, as described in chapter 2.4. Typically, these parameters are derived for small molecules like F₂. Using these parameters for larger molecules is an approximation that could lead to considerable systematic errors.

4.3 Structural investigation of the ordered phase

As a consequence, the vdW potential could, e.g., be underestimated compared to the electrostatics. Since the pair potential calculations were found to produce satisfying results for the interactions of PTCDA, CuPc [32], tetracene [56] and SnPc, this error would probably be found in the vdW parameters for fluorine.

Figure 4.16 b) shows the pair potential map for two $F_{16}\text{CuPc}$ molecules in a stacked geometry. This time the position of the second molecule is changed in the y/z plane while the x position of both molecules as well as their rotation in the x/y plane is equal. It can be seen that the interaction is repulsive, if the y position of both molecules is similar. This is easily explained, since atoms with equal partial charges oppose each other in such a configuration. The situation is different when the shift between the molecules is $\Delta y = \pm 3.9 \text{ \AA}$. At these positions, energy minima of $E_{pot} = -2.02 \text{ eV}$ are found. The reason is that now mostly oppositely charged atoms face each other, leading to an attractive Coulomb interaction between the molecules. The positions of the minima correspond to an ideal layer distance of $|\Delta z| \approx 3.0 \text{ \AA}$ if the molecules are interpreted as being adsorbed in different layers.

4.3.4 Growth of the 2nd layer

$F_{16}\text{CuPc}$ grows in a layer-by-layer mode (Frank-van der Merwe) on Ag(111) at least up to the 3rd layer. This means that the Ehrlich-Schwoebel barrier for diffusion across $F_{16}\text{CuPc}$ island edges must be rather small. An STM image of a preparation with an $F_{16}\text{CuPc}$ coverage between 1 ML and 2 ML is shown in Fig. 4.18. The surface is covered with a close packed first layer of $F_{16}\text{CuPc}$, except for some holes and disordered regions as seen in the image. In the 2nd layer, $F_{16}\text{CuPc}$ also tends to form rows of flat lying molecules, aligned along the same substrate directions than the first layer rows. If the coverage of the 2nd layer is not too high, an intermolecular distance along the rows, which is twice as large as that in the close packed rows of the 1st layer, is preferred. It turned out to be impossible to record higher resolved images of multilayer films, since the molecules are too weakly bound and are easily moved by the STM tip. However, the 2nd layer has been analyzed in more detail in reference [59]. The authors showed that $F_{16}\text{CuPc}$ molecules adsorb on top of 1st layer molecules with a relative rotation of $\approx 45^\circ$ within the limits of measurement accuracy.

Since the interaction between the 1st and 2nd organic layer should be rather physisorptive, this adsorption model can be tested by calculating the pair potential between two vertically displaced $F_{16}\text{CuPc}$ molecules. For this calculation, an out-of-plane separation of $\Delta z = 3 \text{ \AA}$, which was the optimum stacking distance found in Fig. 4.16 b), was applied between the two molecules. Apart from this, the calculation was done in the same way as in Fig. 4.16 a); i.e. the second molecule was scanned across the x/y plane for relative in-plane angles from 0° to 90° . Two of the resulting potential maps are shown in Fig. 4.19. For equal orientation of the molecules $\Delta\theta = 0^\circ$, the potential is strongly repulsive if the 2nd molecule is located on top of the other. This changes when the 2nd molecule is rotated stepwise. The absolute minimum is found for $\Delta\theta = 45^\circ$ with the sec-

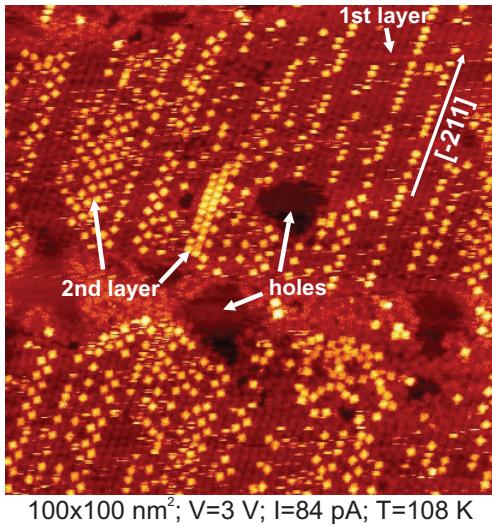


Figure 4.18: STM image of an $F_{16}CuPc$ coverage >1 ML. Molecules in the 2nd layer are found to adsorb with the same alignment to the substrate than those in the first layer. Some holes and disordered regions in the first layer are visible.

ond molecule located at the center of the map. This finding agrees very well with the STM results mentioned before, even though only the interaction with one of the molecules in the first layer has been taken into account. For a more realistic analysis, interactions with the neighboring molecules in the first layer would have to be calculated in addition, which is too time consuming for our purposes. Nevertheless, the result already confirms that the $F_{16}CuPc$ molecules preferably adsorb on top of first layer molecules and are rotated by 45° to reduce repulsion. This kind of geometry resembles the configuration typically adopted by "double-decker" phthalocyaninato (Pc_2) molecules [73, 74].

Adsorption of $F_{16}CuPc$ on $Au(111)$ and $Cu(111)$

A very similar structure compared to that on $Ag(111)$ was reported for the adsorption of monolayer films of $F_{16}CuPc$ on the $Cu(111)$ surface [75] from STM measurements. Molecular rows with two different in-plane orientations were also found. One difference is that in this system, the orientation often changes from row to row instead of every second row. Therefore, the domain wall periodicity is less well defined than on $Ag(111)$.

On the $Au(111)$ substrate on the other hand, results for two different phases have been published. While Chen et al. [76] have reported a row structure similar to that on $Ag(111)$ and $Cu(111)$, de Oteyza et al. [71] have found the molecules to agglomerate with a higher degree of order. All molecules showed the same

4.3 Structural investigation of the ordered phase

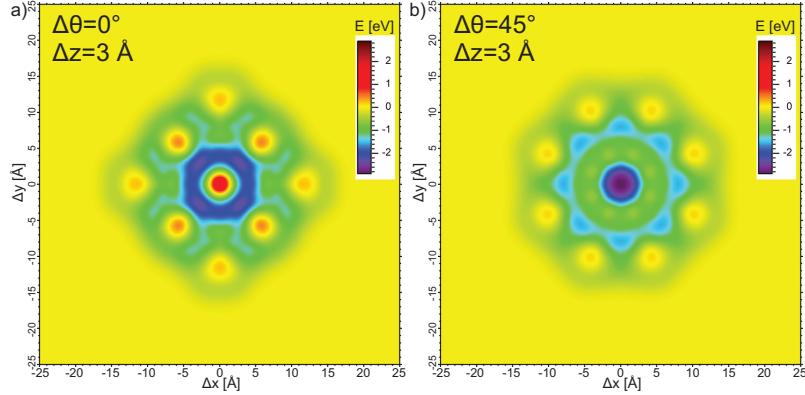


Figure 4.19: Pair potential map for the interaction of two F_{16}CuPc molecules with a separation of $\Delta z = 3 \text{ \AA}$: a) For equal orientation of the molecules, a repulsive region occurs at the center of the map. b) The absolute minimum is found for both molecules lying on top of each other with a relative angle of 45° .

orientation and similar dislocations between all rows could be seen in their STM measurements. However, the discrepancy could simply be the result of different sample temperatures, since the former measurements were done at $T=77 \text{ K}$ while the latter were performed at RT. A phase transition from one ordered phase to another upon cooling would explain the different results. Considering the structure formation tendency of F_{16}CuPc , the reported RT phase might also be the structural motif within a larger row domain. The average size of row domains might change drastically upon cooling as a consequence of the reduced thermal mobility accompanied by a change in the force balance. A coexistence of two different phases is another possibility, especially since STM measurements are very localized. Different phases do not necessarily occupy similar parts of the surface, so that minority phases can easily be missed by STM. Images from the publications of Wakayama, Chen et al. and of de Oteyza et al. are shown in Fig. 4.20.

We have recorded a SPA-LEED image of $\approx 1 \text{ ML} \text{ F}_{16}\text{CuPc}$ on $\text{Cu}(111)$ shown in Fig. 4.21, which is consistent with the STM results by Wakayama. The observed LEED pattern resembles that on $\text{Ag}(111)$, since a similar set of strong hexagonal spots and streaks shows up at the same positions in k -space. The major difference is that the streaks are much more smeared out, so that no maxima are visible along the streaks. This can be understood from the STM image in Fig. 4.20 a). On the $\text{Cu}(111)$ surface, the four row segment that describes the unit cell well for F_{16}CuPc on $\text{Ag}(111)$ appears less frequently, since the periodicity along the $\langle 01\bar{1} \rangle$ directions of the substrate is even more undefined. As hardly any periodicity is preferred, the diffracted intensity is almost completely smeared out in these directions.

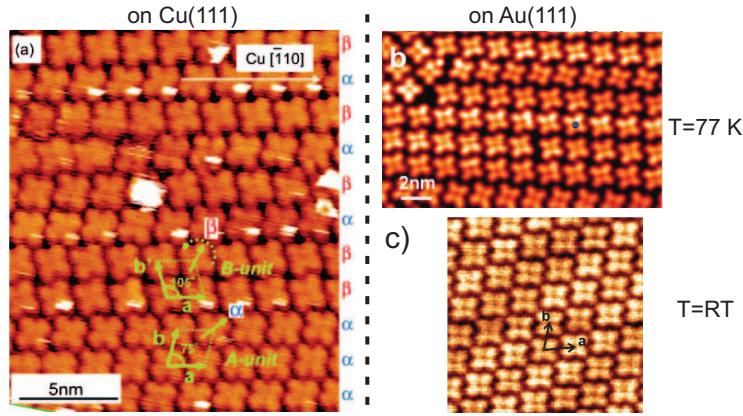


Figure 4.20: STM images of the $F_{16}CuPc$ monolayer structure a) on $Cu(111)$ from Wakayama [75], b) on $Au(111)$ at $T=77\text{ K}$ from Chen et al. [76] and c) a different structure on $Au(111)$ at $T=RT$ from de Oteyza et al. [71].

A comparison of the adsorption behaviors on $Au(111)$, $Ag(111)$ and $Cu(111)$ emphasizes that the strength of the molecule-substrate interaction is the key for the different structure formations. On the weakly interacting Au substrate, the molecules adopt a structure that is dominated by the intermolecular interactions, possibly resulting in larger row domains. For the stronger interacting substrates $Ag(111)$ and $Cu(111)$, different rotations and dislocations are regularly induced in order to reduce the total surface energy of the system.

Comparison with other adsorbate systems

LEED patterns showing well defined streaks have also been found for other molecules on metal or semiconductor surfaces. Murphy et al. [77] investigated Ni(II)diphenylporphyrin (NiDPP) on a substrate of silver evaporated onto $Si(111)$. The authors found a dimer row structure in STM and streaks in LEED consistent with FFT of their STM images. These streaks were attributed to disorder along the molecular rows due to non-equivalent rotations or bending of phenyl rings. Another example is the adsorption of calcium fluoride (CaF_2) on $Si(001)$ studied by Suturin et al. [78]. The authors also find streaky LEED patterns that are explained by a low correlation between adjacent chains of molecules.

It can be concluded that streaks in a LEED pattern of a surface structure are typically the result of a more or less undefined periodicity in one dimension. In the direction perpendicular to the streaks, the periodicity is well defined. This is the case for chains or rows of molecules, as they are usually well ordered along the chain or row, but do not necessarily show a good inter-row correlation.

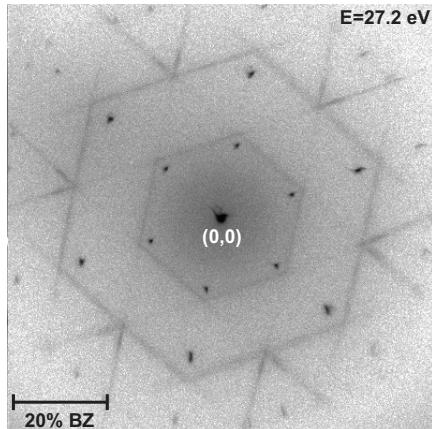


Figure 4.21: SPA-LEED image of ≈ 1 ML $F_{16}CuPc$ on $Cu(111)$. The pattern is similar to that on $Ag(111)$, but the streaks are more smeared out.

The occurrence of dislocations between adjacent rows along or perpendicular to the row direction is usually a result of the molecule-substrate interactions. On stronger interacting substrates misfits occur more frequently, because it is energetically favorable for the molecules to adsorb on specific adsorption sites. These sites are in general not compatible with the periodicity of the adsorbate lattice that is favored due to intermolecular interactions. As a compromise, more or less regular dislocations or other misfits occur to relax the strain in the system. On weakly interacting substrates, the adsorbate-substrate interactions are often not dominant. In this case, the molecules rather arrange in structures that represent a minimum of their intermolecular interaction potential.

4.4 Conclusion

In summary, the adsorption of (sub-)monolayers of $F_{16}CuPc$ on $Ag(111)$ has been investigated for different coverages at RT and at LT to study the effects of fluorination on the adsorption behavior of phthalocyanine molecules. Two distinct phases have been found and discussed. A phase transition between a disordered and an ordered phase occurs at a critical coverage of $\Theta \approx 0.95$ ML or upon cooling a submonolayer film below ≈ 153 K. The disordered phase at RT is the result of the repulsive intermolecular interactions as confirmed by pair potential calculations. The transition to the ordered phase on the other hand is the result of the molecules being sterically forced into ordered arrays upon increasing the coverage or of a change in the total force balance of the system upon cooling.

The structure of the ordered phase was investigated in detail by SPA-LEED and STM. A unit cell with the epitaxy matrix $\begin{pmatrix} 21 & 0 \\ 3 & 6 \end{pmatrix}$ was found to describe

the dominant spot pattern in LEED. This unit cell contains four non-equivalent molecules, which is the result of the row structure in the islands found in STM. Neighboring rows are displaced along their chain direction, which is $[\bar{2}11]$, $[11\bar{2}]$ or $[1\bar{2}1]$ in the respective rotational domains. Two different in-plane orientations of the molecules within the rows were found, so that the dominant structure could be described by row domains with domain walls between every second row and a glide mirror symmetry. The axis through one pair of opposite wings encloses an angle of $\approx \pm 30^\circ$ with the row direction and thus is aligned with one of the high symmetry $\langle 01\bar{1} \rangle$ directions of the substrate. The streaky part of the LEED image, which is not explained by the unit cell, was found to be the result of the poorly defined periodicity perpendicular to the row directions. Missing spots in the LEED pattern have been explained by extinctions caused by the four molecules in the unit cell.

Compared to the non-fluorinated CuPc, the structural motif found here is more complicated. In CuPc films on $Ag(111)$, all molecules are equally oriented, resulting in unit cells containing only one molecule. This is true for the p.o.l.-phase as well as for the commensurate c-phase [45]. The $F_{16}CuPc$ molecules experience a rather strong electrostatic repulsion when they are forced to come closely together. Therefore a close packed $F_{16}CuPc$ film is more stressed than an according CuPc film. This probably causes the observed dislocations and different orientations of the $F_{16}CuPc$ molecules in order to reduce the stress. Consequently, $F_{16}CuPc$ orders in a more complicated epitaxy than CuPc.

The results presented have been compared to the adsorption behavior of $F_{16}CuPc$ on other surfaces and also to different molecules on metal substrates. This leads to a general qualitative understanding of the structure formation of $F_{16}CuPc$ on $Ag(111)$, also in the context of intermolecular (pair-)potential calculations. However, compared to the results for SnPc, the intermolecular forces are not as dominant in $F_{16}CuPc/Ag(111)$, since a substrate induced weakening of the electrostatic interaction between the molecules had to be considered for explaining the structure formation at LT.

5 CuPc/ $F_{16}CuPc$ hetero-organic interfaces on Ag(111)

In this chapter, the co-adsorption of the two organic semiconductors CuPc and $F_{16}CuPc$ on the Ag(111) surface will be examined. CuPc was chosen, since its exclusive adsorption on this surface is already well studied with SPA-LEED, PES and XSW [45]. Also, it has been successfully used in different organic electronic devices [3, 79, 80]. CuPc molecules show intermolecular repulsion on Ag(111) at RT leading to dilute phases, but form commensurate sub-ML islands at LT, which requires an overall attractive interaction. This behavior as well as the resulting structural phase diagram is very similar to SnPc/Ag(111) [8]. The only major difference is that the LT phase contains just one CuPc molecule per unit cell. This is due to the fact that CuPc is a flat molecule, even when adsorbed on the Ag(111) surface as can easily be seen in STM [81]. SnPc on the other hand is non-planar and can be adsorbed in two different geometries as was shown in chapter 3.

The exclusive adsorption of the other component, $F_{16}CuPc$, has been discussed in detail in chapter 4. In the following, the focus will be on hetero-organic systems composed of these two types of molecules. Laterally mixed layers, i.e. mixtures of both molecules within the first monolayer, are analyzed by SPA-LEED in the first section. Afterwards, stacked systems of $F_{16}CuPc$ on closed monolayers of CuPc on Ag(111) will be discussed, considering SPA-LEED and XSW results.

Predictions from pair potential calculations

We will start our investigations with pair potential calculations for the interaction of CuPc and $F_{16}CuPc$ molecules in order to make predictions about the structure formation. In the later sections, the experimental results will be compared to the calculations described here.

The geometrical structures of both molecules are rather similar. Both are planar in the gas phase and only differ in the type of terminating atoms bonded to the four phenyl rings (fluorine vs hydrogen). This leads to a slightly larger diameter of $F_{16}CuPc$ compared to CuPc. However, the main difference is in the electronic structure. Due to fluorination, the molecular orbitals close to the Fermi-level are lowered, which leads to an increased electron affinity [82, 83, 71]. Consequently, $F_{16}CuPc$ is an n-type semiconductor (acceptor) while CuPc is p-type (donor).

The different electronic structures lead to different distributions of partial charges within the two types of molecules, which considerably influences the intermolecular interactions. Figure 5.1 a) shows a map of pair potentials for one

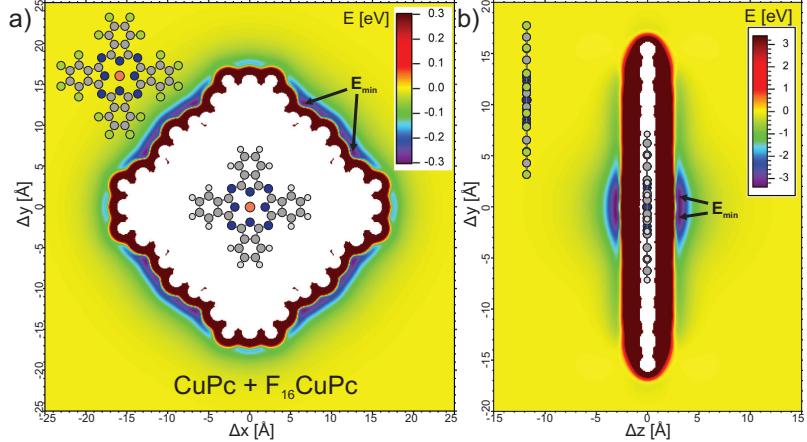


Figure 5.1: Pair potential calculations for CuPc (center of image) and F_{16} CuPc in a) laterally and b) vertically stacked geometry. Blue colors represent attractive regions of the intermolecular potential as given by the color code in the legend.

CuPc with one laterally displaced F_{16} CuPc molecule. The pair potential was calculated for different lateral arrangements of the molecules in analogy to the calculations for SnPc shown in Fig. 3.15. Here, the CuPc molecule was placed in the center of the image, while the position of the F_{16} CuPc molecule was scanned in steps of 0.1 \AA along x and y . This calculation was done for relative in-plane angles of the F_{16} CuPc molecule to the CuPc molecule from 0° to 90° in steps of 1° . It can be seen that the intermolecular potential is strictly attractive, which is mainly caused by the electrostatic attraction between the terminating atoms in the acceptor–donor pair. Only when the molecules get too close, the potential becomes strongly positive due to the Pauli repulsion. The absolute minimum of all calculations can be found for equal in-plane angles of the molecules as shown in Fig. 5.1 a). Eight equivalent minima due to symmetry reasons are found with a depth of $E_{pot} = -0.294 \text{ eV}$. The distance of $|\Delta R| = 14.31 \text{ \AA}$ between the CuPc center and the minima corresponds to the optimum binding distance with respect to the intermolecular interactions considered in the calculations. These energy minima are considerably deeper than the minimum of $E \approx 30 \text{ meV}$ found for the interaction of two CuPc molecules [32]. The potential map of two F_{16} CuPc molecules on the other hand shows no attractive regions at all, as could be seen in Fig. 4.16 a). Therefore, it can be expected that mixed structures of both types of molecules will be favored over a phase separation into pure CuPc and F_{16} CuPc islands.

Figure 5.1 b) shows a similar calculation for CuPc and F_{16} CuPc in a stacked

5.1 Laterally mixed layers of $F_{16}CuPc$ and $CuPc$

geometry. A fixed value of $\Delta x = 0$ as well as equal rotation in the x/y plane was assumed and the position of the $F_{16}CuPc$ molecule was scanned in the y/z plane instead. The resulting intermolecular potential is attractive except for the weakly repulsive corners of the image. Four deep energy minima of $E_{pot} = -3.34$ eV can be found at slight shifts of ± 0.7 Å between the molecules along the y -axis. This suggests that $F_{16}CuPc$ molecules will adsorb flat-lying rather than tilted when deposited on a $CuPc$ monolayer, since a π -stacking of two $F_{16}CuPc$ molecules, as would be found in a tilted geometry, was found to result in shallower energy minima in Fig. 4.16 b) and hence should be less favorable. The positions of the potential minima correspond to a preferred layer distance of $\Delta z \approx 3.1$ Å, which will be compared to experimental results later.

5.1 Laterally mixed layers of $F_{16}CuPc$ and $CuPc$

Laterally mixing two (or more) types of molecules in different ratios is a potential method for producing layers with customized structural or electronic properties. As an example for the investigation of lateral co-adsorption, we mixed $CuPc$ with $F_{16}CuPc$ on the Ag(111) surface. Closed (mono-)layers of mixed films were investigated for many different stoichiometries of $CuPc$ and $F_{16}CuPc$, so that $\Theta_{CuPc} + \Theta_{F_{16}CuPc} \approx 1$ ML. It should be noted that due to the slightly different sizes of the two types of molecules and the different final structures, closing the 1st layer will result in different molecular densities of the film depending on the stoichiometry. The closest packed layer is called a monolayer structure in each case. In all measurements, the molecules were deposited subsequently onto the Ag(111) surface. Deposition was monitored by short 2D in-situ SPA-LEED scans similar to the procedure described for $F_{16}CuPc/Ag(111)$. Also the QMS signals of the molecular fragments at $m/z = 128$ amu for $CuPc$ and 200 amu for $F_{16}CuPc$ were recorded, respectively.

The results are summarized in a rather complex diagram of structural phases, depending on the exact stoichiometry (coverages of both molecules) and on temperature as shown in Fig. 5.2. The sample temperature is plotted versus coverage, whereby both the $CuPc$ and the $F_{16}CuPc$ partial coverages are given in fractions of the total coverage on the x -axis. By varying these parameters, different regions were found, which can be roughly divided into

- an $F_{16}CuPc$ -rich region for $\Theta_{CuPc}/\Theta_{total} \leq 27\%$,
- a $CuPc$ -rich region for $\Theta_{CuPc}/\Theta_{total} \geq 55\%$, and
- an intermediate region in between.

For each region, a number of different measurements has been done at RT and at low temperature around 100 K. In each case, the LEED pattern did not change fundamentally upon cooling, although in most cases more spots were visible at LT. This is due to the reduced mobility of the molecules leading to better ordered layers, and due to the increased Debye Waller factor and the reduced thermal scattering background [13]. In all regions the influence of the deposition sequence was also checked by depositing either $CuPc$ or $F_{16}CuPc$ first, but no

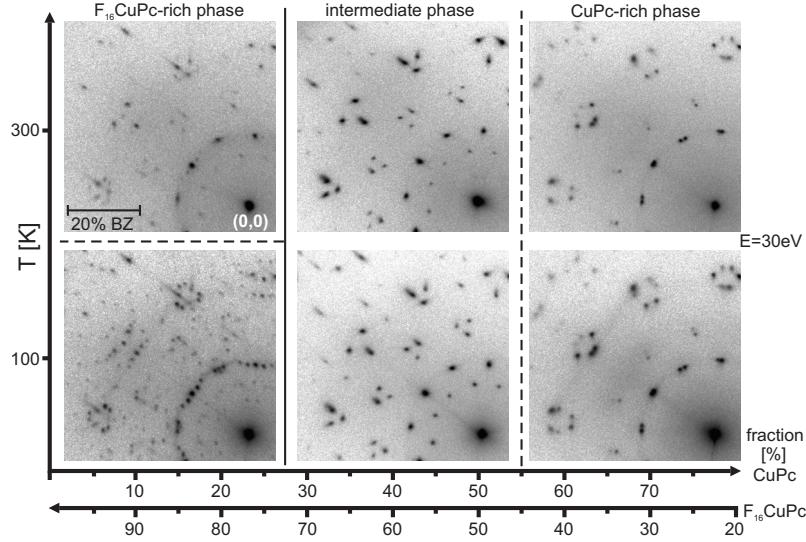


Figure 5.2: Structural phase diagram of mixtures of $F_{16}\text{CuPc}$ and CuPc with a total coverage of $\Theta_{\text{CuPc}} + \Theta_{F_{16}\text{CuPc}} \approx 1 \text{ ML}$. Different stoichiometries have been investigated at RT and at LT. The phase diagram can be roughly divided into three regions.

considerable effect was found.

Integrated ion current signals from the QMS during deposition were used for determination of the coverage of each compound. For calibration of the deposition rate, the integrated ion current from deposition of a known coverage was used. For CuPc , such a reference coverage could be determined very precisely ($\pm 0.02 \text{ ML}$), because CuPc passes through a series of well defined, distinguishable, point-on-line structures between 0.89 ML and 1 ML coverage on $\text{Ag}(111)$ [45]. For $F_{16}\text{CuPc}$, the only possible reference point is the coverage at which LEED spots appear at RT. This transition was ascribed to a coverage of $\approx 0.95 \text{ ML}$ in chapter 4, but with a larger uncertainty.

5.1.1 Intermediate phase

We start with an analysis of the intermediate region of the structural phase diagram, since it is the easiest to describe. Furthermore, the structural motif described here can be found to some degree in the other regions as well. The phase formation behavior was analyzed by in-situ SPA-LEED measurements, as shown in the following.

Fig. 5.3 shows a series of SPA-LEED images recorded at intervals of 1 min during the deposition of CuPc onto a sample covered by 0.23 ML $F_{16}\text{CuPc}$. The formation and transition of phases can be followed in the images. Before

5.1 Laterally mixed layers of $F_{16}CuPc$ and $CuPc$

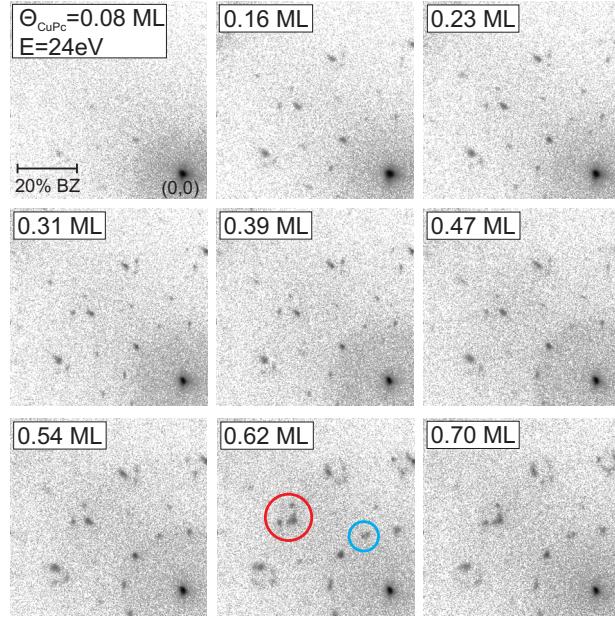


Figure 5.3: Sequence of short 2D SPA-LEED scans monitoring the deposition of 0.7 ML CuPc onto a sample initially covered by 0.23 ML of $F_{16}CuPc$. The circles mark spot groups that change during the phase transition.

depositing CuPc, only diffuse intensity from the dilute $F_{16}CuPc$ film was visible as described in chapter 4. The first important observation is that rather intense LEED spots appeared already after deposition of small amounts of CuPc between 0.08 ML and 0.16 ML. The total coverage $\Theta_{CuPc} + \Theta_{F_{16}CuPc}$ was still far from a closed layer at this point. This shows that ordered hetero-organic islands were formed already at submonolayer coverages (and at RT), which can only be expected when the intermolecular interaction between the different molecular species is attractive. Repulsion, as it is observed for both species when adsorbed without the other at RT, would lead to a phase separation or to a disordered dilute mixed film. The adsorption behavior of the single species was discussed for $F_{16}CuPc$ in chapter 4 and for CuPc in Ref. [45]. Hence, the intermolecular potential considerably influences the growth mode in the submonolayer regime. The LEED pattern remained the same from 0.16 ML to 0.54 ML in the example in Fig. 5.3. At $\Theta_{CuPc} \approx 0.62$ ML, the spot pattern started to change quite abruptly, indicating a phase transition when the total coverage approaches a closed layer. Some of the changed spot groups are marked in Fig. 5.3. In the following discussion, we will concentrate on the sub-ML phase first.

Submonolayer coverages

The LEED pattern that forms in the submonolayer regime (of total coverage) has been analyzed in detail. Generally, most LEED spots of the superstructure in this phase are very intense already at RT, as seen in Fig. 5.2. Only some spots, including the twelve innermost spots around the (0,0)-reflex, are rather faint and can be seen more clearly when the sample is cooled down. No further change in the LEED pattern can be observed at LT. The high spot intensity compared to the background indicates that the adsorbate film is highly ordered. Typically, ordered phthalocyanine domains are often separated by coexisting disordered regions, as was e.g. observed for SnPc/Ag(111) in chapter 3. Such disordered regions reduce the signal-to-background intensity ratio of the superstructure spots. Therefore, we expect that only few disordered regions exist in the intermediate region discussed here, which would further confirm the rather strong intermolecular interactions between CuPc and F_{16} CuPc, favoring the growth of ordered islands.

LEED model

Some of the superstructure LEED spots appeared elongated in many preparations. However, we will postpone the discussion of this observation until the closed monolayer films are analyzed. If the elongations are neglected, the whole LEED pattern can be described by a single unit cell, as shown in Fig. 5.4. The

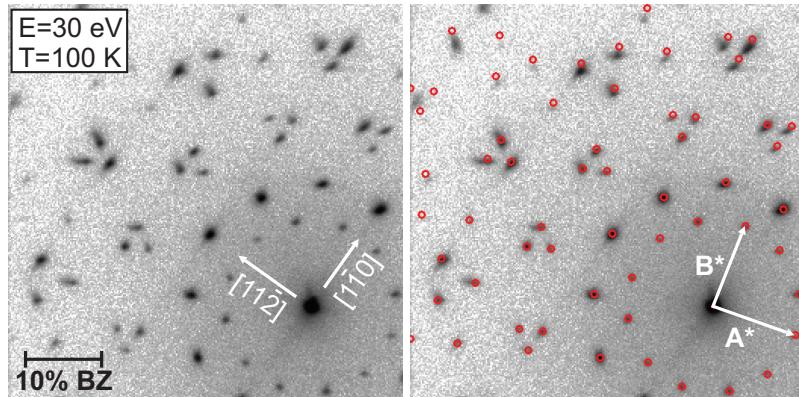


Figure 5.4: 2D SPA-LEED image showing the spot pattern of a mixed system of 0.44 ML of CuPc plus 0.47 ML of F_{16} CuPc on Ag(111). On the right, LEED model spots indicated by the red circles are superimposed. Unit cell vectors and high symmetry substrate directions are indicated by the white arrows.

image on the right side is superimposed with spots calculated from a LEED model (red circles), whereby the white arrows represent the reciprocal unit cell

5.1 Laterally mixed layers of $F_{16}CuPc$ and $CuPc$

vectors A^* and B^* . This superstructure is commensurate with respect to the substrate, as expressed by

$$\begin{pmatrix} \vec{A} \\ \vec{B} \end{pmatrix} = M_1 \begin{pmatrix} \vec{a} \\ \vec{b} \end{pmatrix} = \begin{pmatrix} 2 & -6 \\ 8 & 6 \end{pmatrix} \begin{pmatrix} \vec{a} \\ \vec{b} \end{pmatrix}, \quad (5.1)$$

with \vec{a} and \vec{b} being the unit cell vectors of the substrate. In real space the superstructure unit cell vectors have a length of $|\vec{A}| = |\vec{B}| = 20.84 \text{ \AA}$ and include an angle of 92.2° . Thus, the cell has a rhombic shape. The unit cell area of 434 \AA^2 suggests that it contains two non-equivalent molecules. Considering the stoichiometric ratio of the two types of molecules and their intermolecular attraction, the dominant structure is probably a 1-to-1 phase of one $CuPc$ molecule and one $F_{16}CuPc$ molecule in an alternating "chessboard"-like arrangement. According to surface crystallographic conventions, a primitive rhombic cell is rather described by a centered rectangular Bravais lattice. The respective centered cell M_2 is given by

$$\begin{pmatrix} \vec{A} + \vec{B} \\ \vec{B} - \vec{A} \end{pmatrix} = M_2 \begin{pmatrix} \vec{a} \\ \vec{b} \end{pmatrix} = \begin{pmatrix} 10 & 0 \\ 6 & 12 \end{pmatrix} \begin{pmatrix} \vec{a} \\ \vec{b} \end{pmatrix} \quad (5.2)$$

in this case. Interestingly, the M_2 unit cell describes a $c(2 \times 2)$ superstructure of the $\begin{pmatrix} 5 & 0 \\ 3 & 6 \end{pmatrix}$ unit cell of the c-phase of $CuPc$ on $Ag(111)$ at LT described by Kröger et al. [45]. This finding suggests that the molecules in this mixed phase form a similar lattice as those in the $CuPc$ LT phase, with the difference that every second one is now $F_{16}CuPc$ and possibly has a different in-plane rotation angle.

Since the content of the unit cell is not accessible from SPA-LEED, a more sophisticated pair potential calculation has been carried out in order to specify the most probable molecular orientations (see Fig. 5.5). The x/y potential map for one $F_{16}CuPc$ molecule inside a $\begin{pmatrix} 2 & -6 \\ 8 & 6 \end{pmatrix}$ unit cell was calculated in analogy to the calculations for the c-phase of $SnPc$ in Fig. 3.17. Therefore, intermolecular interactions to its eight nearest neighbors (four $CuPc$ molecules in the corners of the unit cell and the four next $F_{16}CuPc$ molecules, i.e. all molecules drawn in Fig. 5.7 below) were taken into account. In this way, the constraints of the commensurate structure, which in the end arise from the molecule–substrate interactions, are considered. In a detailed calculation, the position ($\Delta x, \Delta y$) of the grid of $F_{16}CuPc$ molecules was scanned across the region marked by the red square in Fig. 5.5 a) in steps of 0.1 \AA while the $CuPc$ molecules remained on fixed positions. This calculation was repeated for in-plane angles θ from 0° to 90° relative to $Ag[01\bar{1}]$ for both the $CuPc$ and the $F_{16}CuPc$ molecules in steps of 1° each.

In Fig. 5.5 b), the map containing the deepest energy minimum is shown. The $CuPc$ molecules are rotated by 52° to a high symmetry substrate direction while the $F_{16}CuPc$ molecules are rotated by 62° . As can be seen, only a small region yields attractive potentials due to the sterical confinement of the center molecule. The optimum position is exactly in the middle of the unit cell, which can be expected because of the symmetry of the arrangement of molecules.

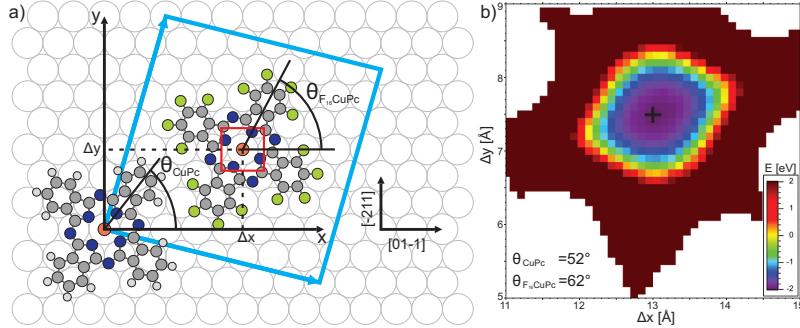


Figure 5.5: Pair potential calculation for F_{16} CuPc inside a 1-to-1 phase unit cell (shown in blue): a) shows the nomenclature of the used distances and angles. A detailed scan was done only for a small region (marked by the red square); b) shows the according potential map at the optimum in-plane orientations of both molecule types. The position of the absolute minimum is marked by a black cross.

This finding agrees well with the SPA-LEED results, since this position is equal to the position that the molecule would occupy in the $\begin{pmatrix} 5 & 0 \\ 3 & 6 \end{pmatrix}$ unit cell of the commensurate CuPc c-phase.

Generally, the commensurate arrangement of phthalocyanine molecules into a $\begin{pmatrix} 5 & 0 \\ 3 & 6 \end{pmatrix}$ unit cell seems to be favorable on the Ag(111) surface, as this unit cell is found for many phthalocyanines on this surface, e.g. CuPc [45], H₂Pc [64], partially fluorinated ZnPc ($ZnPcF_8$) [84] and FePc [68]. This adsorption structure is probably the result of a site specificity of the bonding to the Ag(111) surface, which is similar in all these systems. In a study on the metal-free H₂Pc [64, 33], it was shown that the attractive interaction with the substrate is mediated by the nitrogen atoms in the aromatic body of the molecule. The same mechanism might be responsible for the structural motifs favored by other phthalocyanines, as long as there are no other dominant interactions (e.g. permanent dipole moments or strong electrostatic repulsion). For F_{16} CuPc/Ag(111) we found a large unit cell in chapter 4 containing four molecules with a unit cell vector $\vec{A} = 21 \cdot \vec{d}$. Therefore the distance between the F_{16} CuPc molecules along $\langle 01\bar{1} \rangle$ is larger than it would be in a $\begin{pmatrix} 5 & 0 \\ 3 & 6 \end{pmatrix}$ unit cell (by 1/4 of a surface unit cell vector). This is probably a consequence of the electrostatic repulsion, influencing the structural motif.

In the case of F_{16} CuPc plus CuPc on Ag(111), the deviation of the in-plane orientation of $\Delta\theta = 10^\circ$ between the two molecular species, induced by the unit cell constraints, can be understood as a compromise between the intermolecular and the adsorbate-substrate interactions as follows. The pair potential calculation without unit cell constraints shown in Fig. 5.1 a) yielded a total minimum for *equal* in-plane orientation of the molecules. However, the energy minima

5.1 Laterally mixed layers of $F_{16}CuPc$ and $CuPc$

do not coincide with commensurate adsorption sites in this case. For a relative

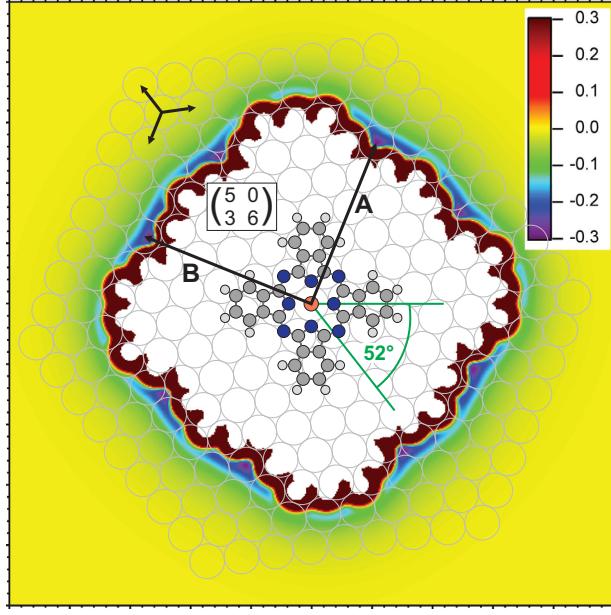


Figure 5.6: The pair potential map of CuPc and $F_{16}CuPc$ with a relative in-plane rotation of 10° and without unit cell constraints. The vectors to the nearest neighbors found from SPA-LEED coincide very well with intermolecular potential minima.

rotation of 10° on the other hand, the unit cell vectors \vec{A}_{CuPc} and \vec{B}_{CuPc} of the $\begin{pmatrix} 5 & 0 \\ 3 & 6 \end{pmatrix}$ unit cell, which describe the positions of the nearest neighbors in the 1-to-1 phase, match the minima of the intermolecular potential quite well. This is visualized in Fig. 5.6, where the Ag substrate lattice is shown superimposed on the potential map between a central CuPc molecule and an $F_{16}CuPc$ molecule, rotated by 10° . The black arrows represent the unit cell vectors with $|\vec{A}_{CuPc}| = 14.45 \text{ \AA}$ and $|\vec{B}_{CuPc}| = 15.02 \text{ \AA}$. Both vectors are only slightly longer than the optimum intermolecular distance of 14.31 \AA found in 5.1 a). Therefore the experimentally observed configuration represents an optimum compromise, similar to the findings for the c-phase of SnPc, as was shown in Fig. 3.18. At these adsorption sites, the energies of interaction of a molecule with the substrate as well as the interaction with its nearest neighbors are both minimized. The small mismatch between preferred adsorbate and substrate lattice enables a commensurate registry, because only a small elastic strain is induced upon matching the two lattices. A similar observation was made for the γ -phase of tetracene on Ag(111) [56], where the positions of intermolecular potential minima were found to be compatible with a point-on-line registry of the molecules.

Adsorption model

The resulting adsorption model is visualized in Fig. 5.7. The molecules are

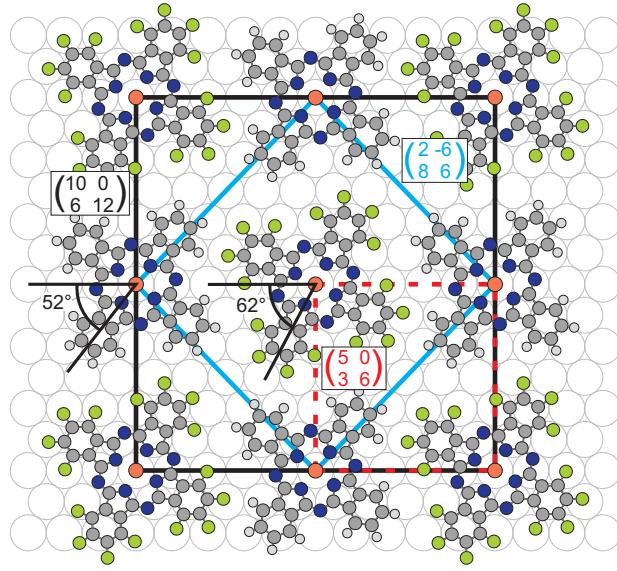


Figure 5.7: Real space model for the sub-ML 1-to-1 phase of CuPc and F₁₆CuPc in the intermediate region: The unit cell as measured by SPA-LEED is shown in blue. One molecule of each type per unit cell is suggested. The adsorption sites are arbitrarily chosen while the in-plane orientations are taken from pair potential calculations. The red dashed unit cell belongs to the commensurate LT phase of CuPc on Ag(111), the black one is a c(2 × 2) superstructure thereof.

represented by ball-and-stick models taken from Gaussian DFT calculations and are drawn on the same scale as the surface model. As already anticipated, two molecules fit very nicely into the M_1 unit cell (blue rhombus). Adsorption sites of the molecules are not known from SPA-LEED and are arbitrarily chosen in the model. However, if the molecules arrange in the optimum intermolecular geometry as given by the calculations above, then the molecule in the center occupies the same adsorption site as the corner molecules. This is visualized by the red dashed rectangle showing the unit cell of the c-phase of CuPc on Ag(111). The in-plane orientations of the molecules are adapted from the pair potential calculations described above.

Interestingly, the F₁₆CuPc molecules order quite differently in the mixed film compared to a pure F₁₆CuPc film, as described in chapter 4. Probably the commensurate adsorption geometry, which is generally favorable for most phthalocyanines on Ag(111), is not adapted by pure F₁₆CuPc islands due to the electrostatic repulsion between the molecules. This hindrance vanishes when the

5.1 Laterally mixed layers of $F_{16}CuPc$ and $CuPc$

$F_{16}CuPc$ molecules are mixed with $CuPc$ species, so that their final structure is changed.

The correctness of the in-plane angles, taken from the pair potential calculations, could be verified by STM in analogy to the measurements for $SnPc$ and $F_{16}CuPc$ discussed in chapters 3 and 4, but this was not done in the context of this work. Measuring exact adsorption sites with STM is very challenging, since atomic resolution has to be achieved for both layers (adsorbate and substrate) simultaneously. Nevertheless, such measurements have been successfully performed for some systems like PTCDA on $Ag(111)$ [85] or $CuPc$ on PTCDA/ $Ag(111)$ [10]. Another potential method might be Surface X-ray Diffraction (SXRD) [86]. The probability for multi scattering events of X-rays is very low which enables an analysis of the relative diffraction intensities with the kinematic theory. However, performing SXRD on organic layers proved to be difficult because of the low interaction cross section of the X-rays, which results in a rather low signal intensity from a thin organic layer, and because of the much higher demands on the quality of the Ag surface in particular regarding a small roughness. Successful studies have been reported only very rarely, e.g. in Ref. [87].

Closed monolayers

As was seen in Fig. 5.3, a phase transition occurs when the total adsorbate coverage approaches a closed monolayer as the commensurate mixed chessboard-like phase described above vanishes. To analyze this transition, we will have a closer look at preparations with different coverages.

We have mentioned earlier that in many preparations some of the LEED spots were elongated along one of the high symmetry directions $[1\bar{1}0]$, $[01\bar{1}]$ or $[\bar{1}01]$ of the silver substrate. Fig. 5.8 shows two LEED images of mixed films with total coverages of 0.75 ML and 0.9 ML, respectively. For 0.75 ML in Fig. 5.8 a), the spots exhibited a Gaussian shape and were well described by the commensurate 1-to-1 unit cell. In the pattern in Fig. 5.8 b) at 0.9 ML on the other hand, many spots appeared elongated, indicating that a part of the film had already started to transform into a new structure. This elongation was not caused by an anisotropic domain size of the superstructure, as can be seen in the linescan in Fig. 5.8 d). Here, clearly two peak components were found for the LEED spot enlarged in Fig. 5.8 c), which means that the spots were split and not broadened. Thus a part of the film had undergone a phase transition and both phases coexisted on the sample. The stronger spot component represents the commensurate phase described above, which still describes the dominant part of the adsorbate film at this coverage.

When the first layer is closed, the phase transition is completed and a new spot pattern evolves, as shown in Fig. 5.9. Here, the total coverage of the mixed film was 1.0 ML. A part of the prominent spot groups closely resembles the spot patterns found for the point-on-line phase of $CuPc$ on $Ag(111)$ [45]. The blue circles indicate LEED model spots for such a $CuPc$ p.o.l.-like phase with a matrix

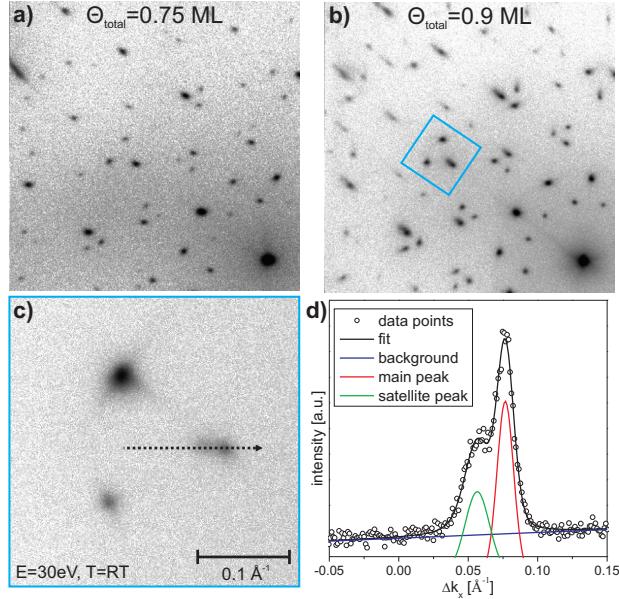


Figure 5.8: a), b) SPA-LEED images of laterally mixed films of CuPc and F₁₆CuPc with total coverages of 0.75 ML and 0.9 ML. c) Closeup of a group of superstructure spots. As indicated by the dashed arrow, a linescan has been recorded along the elongated spot as shown in d), including a fit model.

of $\begin{pmatrix} 5.04 & -0.06 \\ 2.71 & 5.76 \end{pmatrix}$. We can therefore conclude that the molecules have formed a close packed film with similar intermolecular distance vectors than for a close packed CuPc film. Additionally, we found $1/\sqrt{2}$ -order spots in analogy to the findings for the commensurate 1-to-1 pattern discussed before. The adsorbate structure is therefore described by a chessboard-like $c(2 \times 2)$ superstructure of a CuPc p.o.l.-like phase. In Fig. 5.9, a matrix of $\begin{pmatrix} 2.30 & -5.79 \\ 7.76 & 5.73 \end{pmatrix}$ was applied for calculating the corresponding LEED model spots marked in red, which is the according primitive unit cell.

This behavior can easily be explained by similar arguments as for the structure formation of CuPc/Ag(111). The doubled unit cell size indicates that CuPc molecules and F₁₆CuPc molecules alternate in a chessboard-like pattern throughout the submonolayer and monolayer coverage regime, adopting similar structures as a pure CuPc film at LT. At submonolayer coverages the molecules occupy commensurate adsorption sites due to site specific interactions with the silver substrate. In analogy to CuPc/Ag(111) at LT, the molecules are forced to deviate from their favored adsorption sites when the total adsorbate coverage approaches 1 ML due to sterical reasons, since the Pauli repulsion increases.

5.1 Laterally mixed layers of $F_{16}CuPc$ and $CuPc$

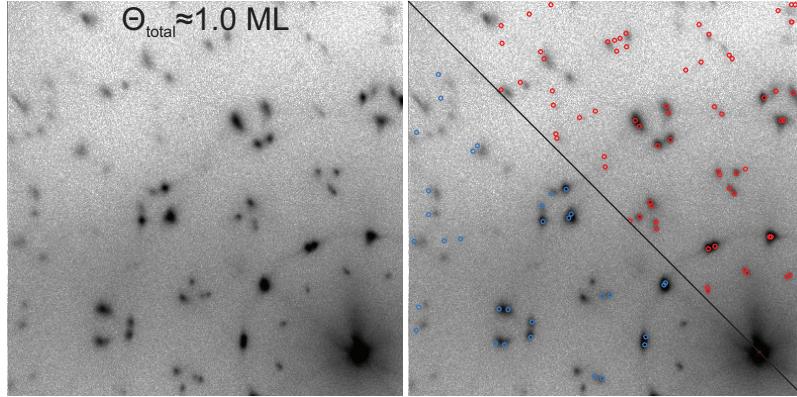


Figure 5.9: Two LEED models for a mixed film of CuPc and $F_{16}CuPc$ with a total coverage of 1 ML. The blue circles mark spots of a CuPc-p.o.l. phase, while the red circles represent a $c(2 \times 2)$ superstructure of the former.

This results in the observed phase transition as the unit cell becomes smaller with its unit cell vectors moving along lines of the substrate lattice. The deviation from the favorable commensurate registry leads to a gradual energy loss of the adsorbate lattice. Following the same argumentation as for SnPc, this effect is overcompensated by the adsorption energy gained when additional molecules are incorporated into the first molecular layer of the mixed film. Similar phase transitions from a commensurate to an incommensurate structure upon coverage increase have been reported e.g. for CuPc/Ag(111) [45], H₂Pc/Ag(111) [64], SnPc/Ag(111) [8] or NTCDA/Ag(111) [88].

Comparison with other hetero-organic systems

Mixtures of CuPc and $F_{16}CuPc$ have also been analyzed on a HOPG surface by Huang et al. [89] via STM. These authors found that for very low CuPc coverages, single CuPc molecules are incorporated into the $F_{16}CuPc$ monolayer structure which is rather similar to that on Ag(111). For mixtures containing comparable fractions of CuPc and $F_{16}CuPc$, an alternating mixed phase forms, that looks like a chessboard in STM due to the different electronic contrast of the two types of molecules. A unit cell of rhombic shape with $A = B = 20.2 \text{ \AA}$ and an angle of 88° between the unit cell vectors was reported. The two types of molecules show almost the same in-plane orientation. Therefore, this structure is very similar to the 1-to-1 phase proposed in this work. The size of the unit cell vectors is slightly larger than those of the mixed phase on Ag(111) found by SPA-LEED. However, reading out unit cells from STM is usually less precise due to the typical distortions of the technique.

A quite similar 1:1 *checkerboard pattern* has been found by Calzolari et al. [90]

for a mixed layer of ZnPc and F_{16} ZnPc on Ag(111). In their work, alternating patterns of equally oriented ZnPc and F_{16} ZnPc molecules were found, which could be differentiated in STM images due to their different electronic contrast. A unit cell of $A = 2.03$ nm, $B = 2.01$ nm and $\theta = 89^\circ$ was reported.

Altogether, mixtures of phthalocyanine molecules with their fluorinated counterparts seem to result in rather similar chessboard-like patterns if the coverages of the two components are comparable. Due to the four-fold symmetry of the molecules, almost quadratic unit cells are favored. The preference for alternating patterns of the fluorinated and the non-fluorinated molecular species was already predicted from the results of the calculation in Fig. 5.1 a). Such an arrangement is mainly stabilized by the electrostatic attraction between the positively charged hydrogen and the negatively charged fluorine terminating atoms. Deviations of the actually measured unit cell vectors and angles from the values calculated for the intermolecular interactions are basically the result of interactions with the substrate. The molecules deviate from their optimum intermolecular arrangement to optimize their bonding to the substrate. In the case of the CuPc– F_{16} CuPc sub-ML 1-to1 phase found in this work, the commensurate unit cell is evidence for a rather strong interaction with the substrate. Therefore, the angular difference of $\Delta\theta=10^\circ$ between the two molecular species calculated in Fig. 5.5, where the fixed unit cell was given as input, differs considerably from the optimum calculated in Fig. 5.1 for only two molecules.

Other STM studies have been published in literature about mixing phthalocyanines with two-fold symmetric molecules, e.g., F_{16} CuPc plus DIP (di-indenoperylene) [91] on Au(111) and on Cu(111), or CuPc plus PTCDA on Cu(111) [92, 93]. Typically, phases with different stoichiometries of both compounds are found coexisting on the surface. Due to the different symmetries of the molecular species, different arrangements are often favored instead of a chessboard pattern. In some cases, the mixed layers order into alternating rows of both species, e.g., CuPc plus DIP on Ag(111) [94]. This shows that in general the structure formation in mixed films can already be influenced, e.g., by the choice of components with specific molecular symmetries.

Interestingly, the 1-to-1 phase of F_{16} CuPc and CuPc on Ag(111) found here also strongly dominates for mixed systems with an excess of F_{16} CuPc. One might expect a phase separation in this case, so that large parts of the surface are covered by 1-to-1 phase islands while the rest is covered by the remaining excess F_{16} CuPc molecules. The LEED pattern should then be a superposition of the $(\frac{2}{8} \ -\frac{6}{6})$ spots and additional spots from ordered F_{16} CuPc regions. However, such additional spots were not observed in films with small F_{16} CuPc excess. Only a very faint indication of a hexagon-like feature was visible in some cases. This could mean that the excess regions are rather disordered. Only when the stoichiometry of deposited molecules was such that the excess of F_{16} CuPc was very large ($\geq 73\%$), a considerably different LEED pattern formed. This F_{16} CuPc-rich region of the phase diagram is described in a later subsection.

5.1.2 CuPc-rich phase

The two different mixed 1-to-1 structures described above also formed in some cases in the CuPc-rich region, i.e. when the CuPc fraction of the total coverage was $>55\%$. A phase separation of the CuPc and $F_{16}CuPc$ components was not found, since no considerably intense $F_{16}CuPc$ superstructure spots have been observed. This supports the already predicted preference for mixed structures. However, in many preparations we found another structure, which will be analyzed in the following. Two examples for this structure are shown in Fig. 5.10 together with proposed unit cells. The LEED spot patterns resem-

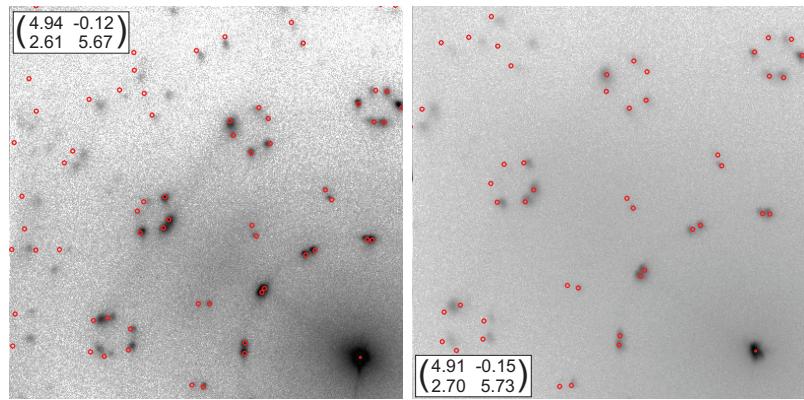


Figure 5.10: Two SPA-LEED images of CuPc-rich mixed films together with calculated LEED model spots. a) 0.6 ML CuPc + 0.4 ML $F_{16}CuPc$ at LT; b) 0.7 ML CuPc + 0.3 ML $F_{16}CuPc$ at RT. Both patterns resemble CuPc/Ag(111) p.o.l.-phase patterns.

bled CuPc/Ag(111) p.o.l.-phase patterns, but without additional $1/\sqrt{2}$ -order spots in this case. Already during the deposition, the sub-ML spot pattern rather resembled the CuPc c-phase pattern instead of the commensurate 1-to-1 mixed film pattern. Obviously the structure formation was very similar to the intermediate stoichiometry region, except that no $c(2 \times 2)$ superstructure was formed. All the CuPc-like unit cells we found in this CuPc-rich region of the phase diagram are not large enough to contain more than one molecule. However, since there are no indications for the opposite, it must be assumed that all molecules were still located in the first molecular layer and formed a disordered (regarding the CuPc- $F_{16}CuPc$ arrangement), alloy-like structure instead of the (2×2) superstructure. This means that the $F_{16}CuPc$ molecules were statistically distributed like defects in the CuPc dominated film. Therefore, no additional superstructure spots occurred as the according periodicity was missing. This is the result of an uncompleted intermixing, since it is probably not a thermodynamically stable order, and obviously happens preferably for mixtures with high CuPc ratio. The lower the $F_{16}CuPc$ ratio, the lower is the probability to find considerably large parts of the surface covered by chessboard-like

structures after the deposition, producing the according superstructure LEED spots. The LEED pattern is instead dominated by pure CuPc domains. We suppose that the higher ordered chessboard structure is more stable, since an alternating sequence of CuPc and F_{16} CuPc seems to be favorable considering the intermolecular interactions between the two species, cf. Fig. 5.1 a). This is supported by the fact that the chessboard structure was formed in some preparations even in this stoichiometric region. It can therefore be expected that it is possible to transform the CuPc-like structure into the $c(2 \times 2)$ superstructure by annealing the sample, an experiment that was not performed in the scope of this work, however.

5.1.3 F_{16} CuPc-rich phase

At last, the phase with a high stoichiometric fraction of F_{16} CuPc will be discussed. This region exists for CuPc fractions up to $\approx 27\%$ with the rest of the first layer being filled with F_{16} CuPc. Figure 5.11 shows the F_{16} CuPc-rich part

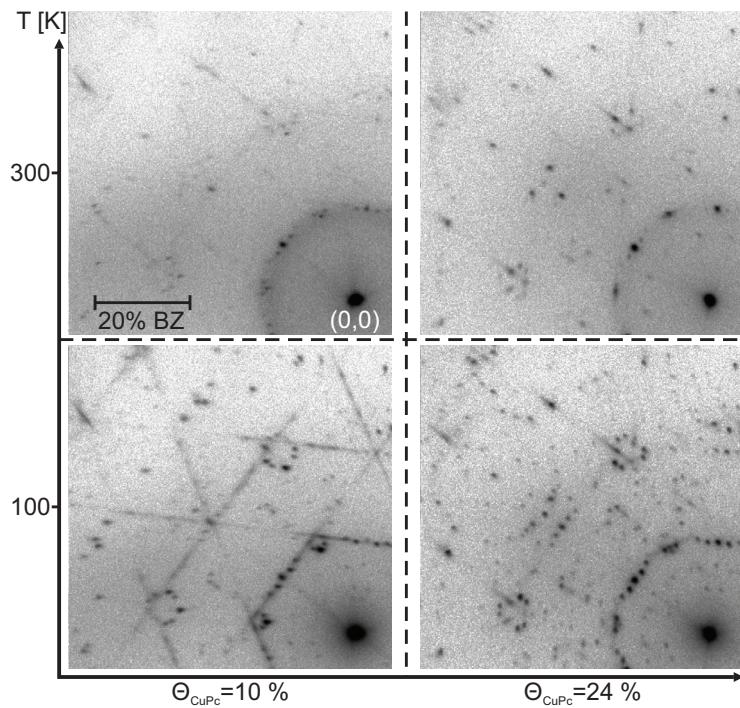


Figure 5.11: Details of the F_{16} CuPc-rich region of the structural phase diagram, showing very complicated spot patterns. Measurements for two stoichiometries are shown, conducted at RT and LT ($E=30$ eV).

of the structural phase diagram in more detail with SPA-LEED images for two

5.1 Laterally mixed layers of $F_{16}CuPc$ and $CuPc$

different stoichiometries, both investigated at RT and LT. For very small CuPc partial coverages around 10%, all spots had a very weak intensity at RT. When the CuPc fraction was increased to $\geq 20\%$, the intensity of some spots increased considerably. A closer look reveals that these strong spots at RT are identical to the spots of the commensurate 1-to-1 phase in the intermediate stoichiometric region described before in chapter 5.1.1. This is visualized in Fig. 5.12 a), where

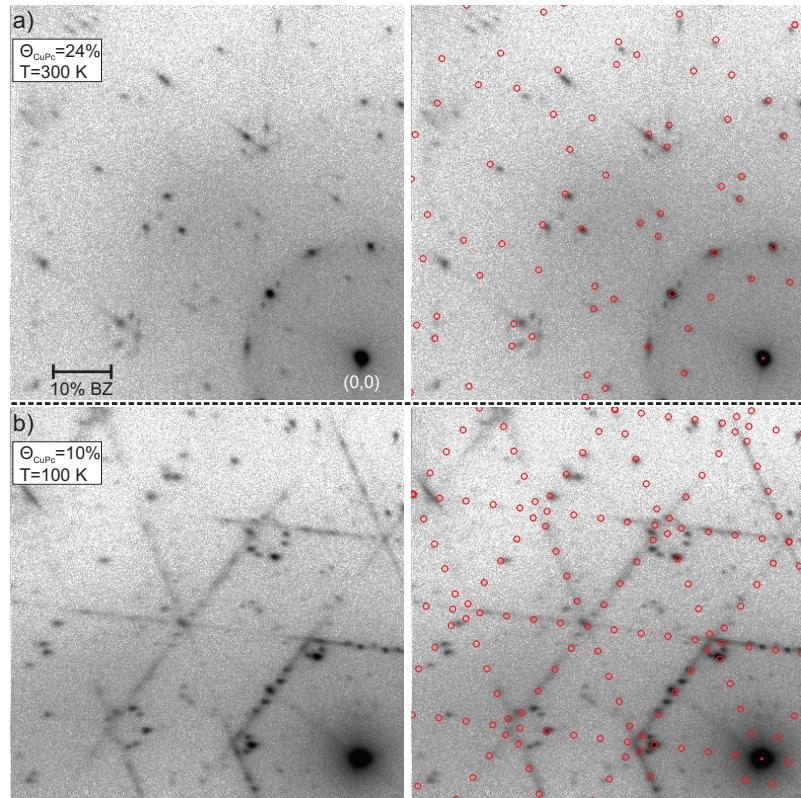


Figure 5.12: 2D SPA-LEED diffractograms of $F_{16}CuPc$ -rich mixtures with a) $\approx 24\%$ CuPc at RT and b) $\approx 10\%$ at LT. On the right side, LEED model spots are superimposed on the same images.

a mixed structure with a CuPc fraction of 24% is shown. On the right side, the SPA-LEED image is superimposed with the 1-to-1 phase spots. It can be seen that most of the intense spots are explained by the model. The interpretation is that a part of the adsorbate film arranged in this phase. The lower the CuPc coverage is, the less surface area can be filled with 1-to-1 phase islands and in turn the weaker are the according LEED spots.

However, most of the surface exhibited a different structure. This became

obvious when the sample was cooled to LT. The spots of the 1-to-1 phase were still present, but many new spots became visible that are not explained yet (see lower right image in Fig. 5.11). A large excess of $F_{16}CuPc$ naturally leads to the assumption that a large part of the adsorbate film consists of islands of pure $F_{16}CuPc$ arranging in the monolayer structure that was analyzed in chapter 4. Indeed, for very low CuPc coverages at LT, like in the lower left image in Fig. 5.11, the typical streaky features can be found. These streaks appeared at the same positions in reciprocal space like those of the $F_{16}CuPc$ monolayer pattern, as shown in Fig. 5.12 b). The according spots were hard to identify because they were very weak and/or smeared out. Also in this low CuPc coverage region, there are still unexplained spots left.

Interestingly, for CuPc coverage fractions above 20%, the streaky $F_{16}CuPc$ features almost disappeared, see lower right image in Fig. 5.11. Probably it is energetically favorable for the $F_{16}CuPc$ molecules to incorporate CuPc molecules into their structure. This is reasonable considering the informations obtained from the pair potential calculations. While the intermolecular interactions are repulsive for all lateral arrangements between two $F_{16}CuPc$ molecules, strongly attractive regions exist for interactions with CuPc molecules. Therefore, the disappearance of the streaky pattern as well as the still unexplained LEED spots are probably the result of the formation of at least one more mixed structure on the surface. The unit cell of this structure presumably contains several molecules, most of them being $F_{16}CuPc$ species. Unfortunately, a convincing LEED model explaining the missing spots could not be found so far. Here, the help of other experimental techniques like STM will be necessary.

5.1.4 Conclusion

The lateral structure formation in hetero-organic mixed films composed of CuPc and $F_{16}CuPc$ has been investigated by SPA-LEED as a function of adsorbate coverage, stoichiometry and sample temperature. Similarities and differences compared to the adsorption of pure CuPc or $F_{16}CuPc$ films on Ag(111) have been found and discussed. For stoichiometries with small CuPc portion, very complex LEED spot patterns have been found, which correspond to large unit cells containing several molecules. For higher CuPc portions, much simpler superstructures are formed. Due to the intermolecular attraction between CuPc and $F_{16}CuPc$ molecules, alternating chessboard-like patterns are favored in the film structure, which was confirmed by pair potential calculations. Only for large excesses of CuPc, a different structure was found in some cases, which could be explained by a statistical distribution of $F_{16}CuPc$ molecules in a CuPc-dominated film. In general, the molecules in the mixed film order very similar to the CuPc/Ag(111) structure formation at LT. This emphasizes that similar site specific interactions are present in different phthalocyanine species which can lead to similar adsorption behaviors. Pure $F_{16}CuPc$ films differ from this, probably due to their electrostatic intermolecular repulsion. Altering the chemical environment of the $F_{16}CuPc$ molecules by mixing them with CuPc changes their resulting structure. The mixed films were found to grow in ordered 2D

5.1 Laterally mixed layers of $F_{16}CuPc$ and $CuPc$

islands on the surface at RT, which is different from the growth mode of both pure CuPc and pure $F_{16}CuPc$ on Ag(111), forming dilute films for submonolayer coverages at this temperature.

In conclusion, it was shown that mixing different phthalocyanine species in a specific stoichiometry is an interesting approach for tuning the adsorption behavior of an adsorbate film. Together with controlling the two other external parameters of sample temperature and total coverage, different lateral structures can be produced on the Ag(111) surface.

5.2 F_{16} CuPc on closed CuPc monolayers

In this section, an investigation of vertically stacked hetero-organic adsorbate systems of CuPc and F_{16} CuPc will be reported. In contrast to the previous section, a closed layer of CuPc on Ag(111) was initially prepared by desorbing higher layers of a thicker film at $T \approx 553$ K. Afterwards, the desired amount of F_{16} CuPc was deposited on top at RT. In our SPA-LEED chamber, the F_{16} CuPc coverage was estimated from the integrated IC signal measured by the QMS. For calibration of the deposition rate, the value which was estimated for depositing a monolayer of F_{16} CuPc directly onto the Ag substrate was used. This will induce a small error since the sticking coefficient on both substrates, Ag(111) and CuPc/Ag(111), is probably not equal.

5.2.1 SPA-LEED

SPA-LEED measurements of F_{16} CuPc on CuPc/Ag(111) have been performed at RT and LT for different coverages Θ_2 of F_{16} CuPc in the 2nd layer. The results are summarized in Fig. 5.13. The first important observation is, that the

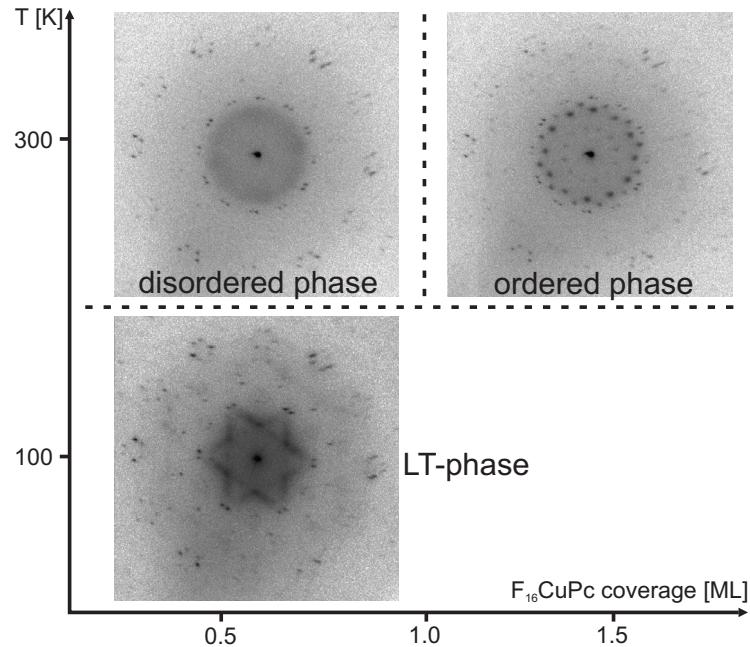


Figure 5.13: Structural phase diagram of F_{16} CuPc on CuPc/Ag(111): Rather disordered patterns with low spot intensities dominate.

typical spots of the CuPc p.o.l.-phase are visible in all structural phases of the diagram. They can be seen easily in the upper left LEED image in Fig. 5.13,

since there only a ring of diffuse scattering intensity from the $F_{16}CuPc$ is visible. Therefore, it can be concluded that the majority of $F_{16}CuPc$ molecules did not enter the CuPc layer and the lateral order of CuPc was unchanged by the deposition of $F_{16}CuPc$. However, the spot positions were usually described by the superstructure matrix given for a CuPc coverage of 0.97 ML rather than 1 ML [45]. This means, that probably a small percentage ($\approx 3\%$) of the CuPc molecules was desorbed from the 1st layer during our standard annealing procedure before $F_{16}CuPc$ was deposited. The intensity of the CuPc spots was rather weak due to the damping by the 2nd layer. Scattering at the $F_{16}CuPc$ molecules manifested in diffuse intensity around the (0,0)-spot for $\Theta_2 < 1$ ML. Close inspection revealed, that this intensity is not a uniform ring, but shows some star-like modulation. If the $F_{16}CuPc$ coverage was increased above 1 ML, new fundamental spots appeared in some preparations and the diffuse intensity disappeared. However, this phase transition was not always observed and the resulting new spots were not always as sharp and intense as in the example in Fig. 5.13. The ordered phase transformed back into the disordered phase when the sample was annealed at $T \approx 393$ K, although no desorption could be measured by the QMS. It also became gradually disordered during a longer SPA-LEED scan as a result of radiation damage. Hence this phase is not very stable. When the disordered phase was cooled to LT, the star-like scattering intensity became more distinct, so that the star could be described by short streaks. Along the contour of the star, maxima could be observed, representing broadened spots. Therefore, this pattern shows some similarities to the streaky pattern of $F_{16}CuPc$ on Ag(111), cf. Fig. 4.12. In the case of $F_{16}CuPc$ on CuPc/Ag(111), the streaks appeared at smaller k -values, however. The LT phase also formed when an adsorbate layer with $\Theta_2 > 1$ ML was cooled, but the pattern was more diffuse in this case. This phase also showed beam damage already after ≈ 30 min, which complicated the analysis of the pattern, as achieving good statistics of the intensity distribution was almost impossible. Higher orders of the superstructure spots were very faint and hardly detectable in all phases, which is a sign for incommensurability of the structure.

For the ordered diffraction pattern of $F_{16}CuPc$ on CuPc/Ag(111), a structural model has been found, which describes all diffraction spots. LEED spot positions calculated from this model are shown as red circles in Fig. 5.14. The according superstructure unit cell is described by a matrix of

$$M = \begin{pmatrix} 7.13 & 5.29 \\ 0.48 & 11.51 \end{pmatrix}. \quad (5.3)$$

This unit cell is incommensurate (possibly point-on-line) and corresponds to an oblique real space unit cell with $|\vec{A}| = 18.52$ Å, $|\vec{B}| = 32.60$ Å, including an angle of 72.34° and an area of 575.41 Å². The finding, that all spots of the 0.97 ML p.o.l.-phase of CuPc/Ag(111) can also be indexed as spots of this unit cell, indicates a strong relation between the two layers. We calculate the transition matrix T between the matrix of the ordered phase and the CuPc-matrix N [45],

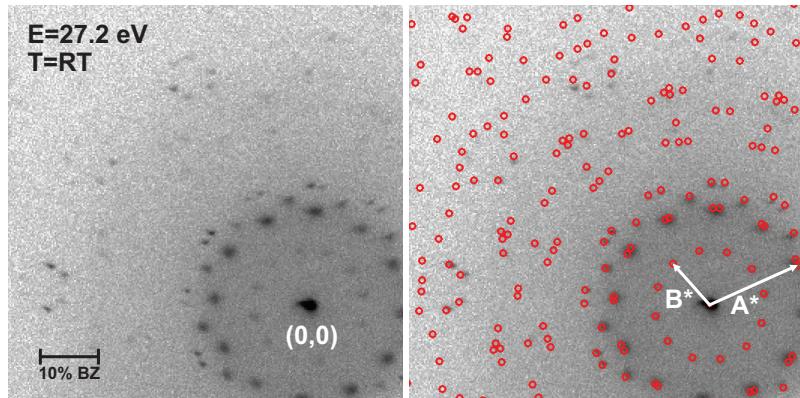


Figure 5.14: LEED model for the ordered phase of F_{16} CuPc on CuPc/Ag(111). Calculated positions of LEED spots are indicated by the red circles in the right image, reciprocal unit cell vectors are drawn as white arrows.

defined by $M = T * N$, which results in

$$T = M * N^{-1} = \begin{pmatrix} 7.13 & 5.29 \\ 0.48 & 11.51 \end{pmatrix} * \begin{pmatrix} 4.75 & -0.22 \\ 2.61 & 5.60 \end{pmatrix}^{-1} = \begin{pmatrix} 0.96 & 0.98 \\ -1.01 & 2.02 \end{pmatrix}. \quad (5.4)$$

As can be seen, all elements of the transition matrix are very close to integer values. Therefore a commensurate registry of the F_{16} CuPc layer with respect to the CuPc layer underneath is possible within error bars. This is surprising, since the CuPc layer itself only shows point-on-line registry with the Ag substrate, so that the CuPc molecules have different adsorption sites. Hence, the F_{16} CuPc adsorption sites are not strongly influenced by the interactions with the Ag substrate, but determined by the CuPc lattice. This could be caused by the interaction between partial charges on the F_{16} CuPc and CuPc molecules or by π -stacking mechanisms. Obviously these interactions are not very strong, since we found that the structure is rather unstable.

5.2.2 XSW analysis of CuPc on Ag(111)

The SPA-LEED results discussed above raise the question about the strength of the interaction between the two organic layers of CuPc and F_{16} CuPc. An interesting parameter indicating the interaction strength in stacked systems is their vertical distance, given by the adsorption heights. XSW allows the determination of adsorption heights with a high precision of typically $\Delta d^H \approx 0.05$ Å and is therefore the method of choice. However, since synchrotron radiation is necessary, only one measurement could be done in the context of this work. This has been performed at the beamline ID32 of the European Synchrotron Radiation Facility (ESRF) in Grenoble, which was equipped with a hemispheri-

cal electron analyzer (PHOIBOS 225, SPECS) at an angle of 90° relative to the incident X-ray beam.

The analysis was expected to be challenging, since both types of molecules are chemically very similar, only differing by the terminating atomic species. Therefore, an XSW analysis of an exclusively adsorbed CuPc monolayer was performed first as comparison. Due to time constraints, this measurement was done at RT only.

XPS fit models

For the XSW analysis, XPS scans at different incident photon energies around the Bragg energy of 2636 eV have been performed for the C1s, N1s and Cu2p_{3/2} core level regions. It is known that an X-ray beam induces beam damage in organic samples, which manifests in a significant reduction of the coherent fraction in XSW. The onset of this effect defines the limit for the acquisition time on one spot of the sample. Based on the experience from a previous XSW study of CuPc on Ag(111) [45], we chose a maximum acquisition time of ≈ 20 min at RT. To achieve satisfying statistics, scans for each atomic species were performed on different spots of the sample and summed up for the analysis. As a small crystal mosaicity is a prerequisite for XSW, we only measured on spots, which yielded a nicely shaped reflectivity curve with a FWHM ≤ 1.1 eV. The energy axis was calibrated by measuring the Ag3d_{3/2} and Ag3d_{5/2} core level positions of the substrate and comparing these with tabulated values.

Additionally, XPS scans with high statistics have been recorded for the same core level binding energy regions at an off-Bragg energy of the incident photons. When no Bragg condition is fulfilled, the X-ray intensity does not depend on the height of the atoms above the surface since there is only the incident wave instead of an intensity modulated standing wave. Consequently, the relative areas of different peaks or peak components will reflect the stoichiometry of the corresponding species within a molecule, since the relative intensities will mainly be given by the number of scatterers. This allows to set constraints, which reduces the number of free parameters for the fitting of the XPS data. In this way, fit models for the different atomic species have been developed, which were then used for fitting the XSW photoemission spectra. The area of the background subtracted total region or of a fit component at one specific photon energy gives one point of the according photoelectron yield curve (partial photoemission yield). Repeating this analysis for all photon energies around the Bragg energy with the same fit model, the complete yield curve is acquired.

Fig. 5.15 shows the off-Bragg XPS scans together with the final fit models. The XPS analysis has been done with the program CasaXPS [95]. Generally, peaks were modeled by Voigt functions with 30% Lorentzian contribution. The positions and FWHMs of the peaks have been left unconstrained to a large extent. The only strict constraints used were area constraints due to stoichiometry reasons for chemically different atomic species. Details of the fit models for the Cu2p_{3/2}, N1s and C1s core levels will be described in the following.

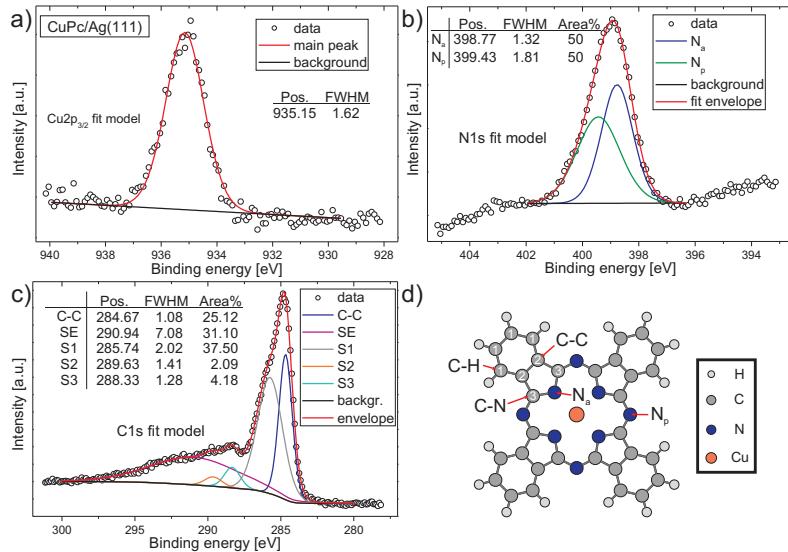


Figure 5.15: a)–c) XPS scans and fit models for the Cu2p_{3/2}, N1s and C1s core level regions. The scans were taken at an off-Bragg energy of 2640 eV of the incident photons. d) Geometrical structure of CuPc, showing the chemically different carbon and nitrogen species.

- The Cu2p_{3/2} region could simply be fitted by one peak and a linear background.

This is reasonable, since only one copper atom is present in each molecule, so that all Cu atoms are chemically identical.

- For N1s, the shape of the main peak is clearly asymmetric, so that two fit components were necessary. As background, a linear function was chosen again.

This is a consequence of the two chemically different nitrogen atoms which are present in the molecule - pyrrole nitrogens N_p and azaporphyrine nitrogens N_a, the latter being bonded to the copper atom, cf. Fig. 5.15 d). To take advantage of the stoichiometry of N_a : N_p = 1 : 1, the fit was constrained to give equal areas for both peaks. We ascribe the peak at larger binding energy to the pyrrole nitrogens in analogy to a recent XPS study on a multilayer of cobalt phthalocyanine (CoPc) on Ag(111) by Schmid et al. [96]. The authors report a chemical shift of 0.48 eV between the two nitrogen species in CoPc, which is roughly comparable to the shift of 0.66 eV found here. Note, that the background contains two broad peaks at ≈ 403 eV and ≈ 393 eV, which are due to Ag plasmon excitations. However, these are completely cut off by the linear background chosen here, so that a more sophisticated background treatment was not

necessary. This is different from the analysis of previous measurements for which a different analyzer geometry was used, however [45].

- The C1s spectrum looks quite complicated as it contains several fit components and a Shirley background [97].

Since a dedicated fit model is important for the later analysis of the stacked system, different models have been tried for C1s. The CuPc molecules contain three types of carbon atoms. Carbon species with only C or H neighbors are labeled 1 and 2 in Fig. 5.15 d) and have very similar binding energies. They are therefore represented by only one peak labeled C-C in the spectrum. The carbon atoms which are bonded to nitrogen (C-N) are chemically slightly different from the C-C carbons. The according peak is shifted to a higher binding energy E_B , so that it is located in the high energy shoulder of the main peak of the spectrum. The area of the peak should be 1/3 of the C-C peak, due to the stoichiometry of the molecules. However, the shoulder is much larger, so that it probably contains a second component. A possible explanation could be that one of the other components might be a shake-up satellite of the C-C peak. This would mean, that the photoelectrons of C-C and C-C* stem from the same source, but the C-C* electrons lost a discrete amount of energy before reaching the analyzer. In this case, the stoichiometry would have to be (C-C + C-C*) : C-N = 3 : 1. Another possibility is that the shoulder contains a component from a recoil excitation of vibrational structure. Such an effect has been studied in detail for CF_4 by Thomas et al. [98], and was found to lead to a low kinetic energy shoulder that increases with photon energy. We have tried to separate the components in the shoulder in Fig. 5.15 c), but a subsequent XSW analysis did not produce meaningful results. Therefore, only one component (S1) was used in the final fit model to reduce the number of fitting parameters. The broad component (SE) describes a continuous tail of electrons which stem from one of the sources of the other peaks, but have lost non-discrete amounts of energy on their way out of the sample due to inelastical scattering. Finally, two small peaks (S2 and S3) are necessary to fit the high energy side of the spectrum. These components could be shake-up satellites of the C-C or the C-N peak. Since their origin is unclear, no according constraints were applied.

This set of fit components describes the experimental curves quite well as can be judged from the fit envelopes (red curves in Fig. 5.15 b)-c)). However, for C1s only the XSW result for the total region will be shown in the following. Regarding the height determination by XSW, the only meaningful single component is the C-C peak, which produces almost the same XSW results as the total region.

XSW results

The fit models described above have been used to fit the XPS scans for the XSW analysis at different photon energies. Positions and widths of all peak components were fixed rather strictly to the optimum values found in the off-Bragg XPS scans, constraining all peak widths to a tolerance of ± 0.1 eV. All peak positions were coupled to the position of the first component, which was in turn constrained to the optimum value ± 0.1 eV. All former constraints for the peak areas have been loosened on the other hand, since the areas represent the photoelectron yield, which is now the fit result of interest for the XSW analysis. The complete electron yield curves are given by the areas of the according core level regions at each energy of the XSW scan taken from CasaXPS. These values are taken as input and are fitted by the electron yield equation 2.6, using the program Torricelli [99]. Fig. 5.16 shows an overview of the electron yield curves of the total Cu2p_{3/2}, N1s, and C1s regions together with the according fits and fit results, as well as a representative reflectivity curve. All curves have

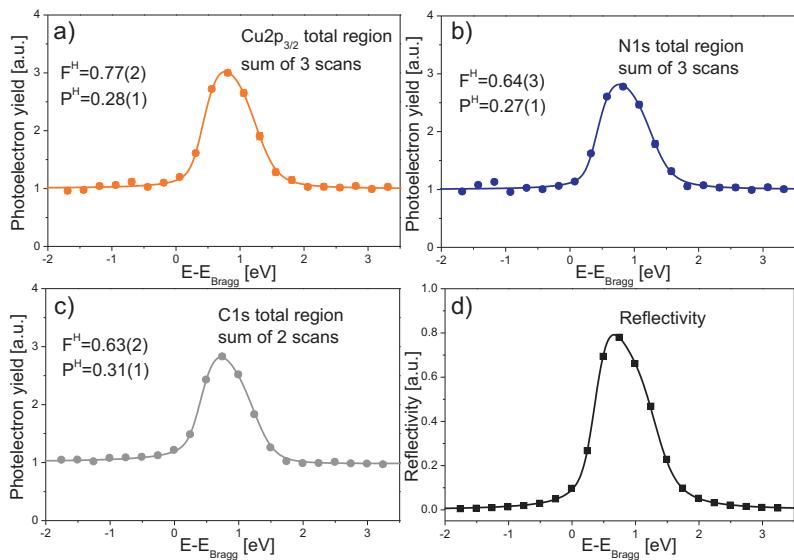


Figure 5.16: a)–c) Electron yield curves and fit results for the Cu2p_{3/2}, N1s, and C1s total regions in CuPc/Ag(111). d) shows a representative reflectivity curve.

been normalized to the incident X-ray beam intensity, since this intensity is not constant during the measurement. The reflectivity curve is rather sharp with a FWHM of ≈ 1.0 eV, which indicates a good substrate quality. All electron yield curves are nicely fitted with very small error bars and show comparable fit results for each atomic species. Copper and nitrogen are found at almost the same coherent position, while the carbon position is slightly higher. The coherent

fractions of all species are rather high, indicating that the layer is vertically well ordered. Furthermore, this means that the positions of the chemically different nitrogen (N_a , N_p) and carbon atoms (C-C, C-N) can not differ much. We can conclude that the CuPc molecules are adsorbed flat on the Ag(111) surface and essentially remain in their gas-phase intramolecular geometry. Notably, the error bars given for the fit parameters of the electron yield curves are typically very small. These errors originate from the error output from CasaXPS for the peak areas, i.e. the electron yield. Other systematic errors are probably larger, but difficult to quantify. If several measurements are performed for an atomic species, the standard deviation of the results for the separately analyzed scans can be used as a meaningful error bar for the results of the summed scans. However for CuPc/Ag(111), not enough statistics was available, so that an error of $\Delta d = 0.05 \text{ \AA}$, based on previous experience, will be assumed for the adsorption heights instead. This typical error was estimated with a different setup resulting in worse resolution and should therefore be an upper limit for our measurements.

The exact fit results are not perfectly equal, but comparable to the previous results of Kröger et al. [45]. A comparison with these results is shown in Table 5.1. While the results for C1s are very similar, the N1s and Cu2p_{3/2} results

core level	this work			Kröger et al.		
	F^H	P^H	$d^H [\text{\AA}]$	F^H	P^H	$d^H [\text{\AA}]$
Cu2p _{3/2}	0.77(2)	0.28(1)	3.02(5)	0.54(2)	0.258(3)	2.97(4)
N1s	0.64(3)	0.27(1)	3.00(5)	0.57(2)	0.297(3)	3.04(4)
C1s	0.63(2)	0.31(1)	3.09(5)	0.475(5)	0.310(2)	3.08(3)

Table 5.1: Fit parameters for the XSW analysis of 1 ML CuPc/Ag(111) and comparison with Kröger et al. [45]

differ slightly. In the measurement of Kröger et al., the copper atoms were found below the nitrogen atoms, while in our case, they are slightly above. One important difference is that the measurements of Kröger et al. have been performed with a different analyzer geometry (45° to the incident beam). In this setup, multipole correction parameters are necessary and satellites like bulk plasmons are found to be much stronger, which complicates the fitting process. However, if the adsorption heights d^H , calculated from P^H , are compared, one finds that the error bars in both measurements overlap for all species. The results are therefore compatible.

The two single N1s components have been analyzed separately, as shown in Fig. 5.17. For the N_a component, we obtain a very high coherent fraction, indicating a well defined adsorption height. The fraction of N_p is smaller, accounting for a lower degree of order. Both coherent positions of $P^H(N_a)=0.28$ and $P^H(N_p)=0.26$ are close to the average N1s value, obtained from the analysis of the total region in Fig. 5.16 b). The corresponding adsorption heights are $d^H = (3.02 \pm 0.05) \text{ \AA}$ and $d^H = (2.97 \pm 0.05) \text{ \AA}$ for N_a and N_p , respectively. The difference of 0.05 \AA between the two N1s species is smaller than the sum

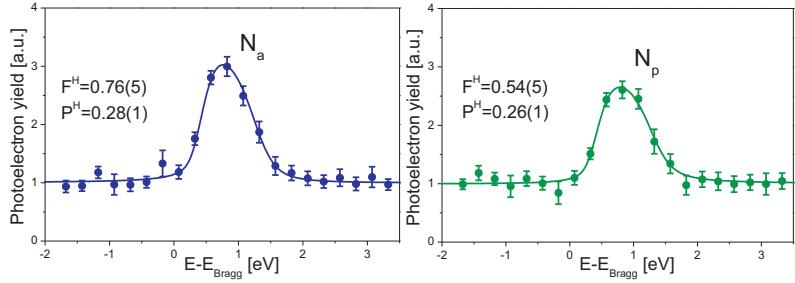


Figure 5.17: Electron yield curves and fits for the N1s components of CuPc/Ag(111).

of the error bars for the two adsorption heights. Hence, the adsorption heights of the nitrogen atoms in the CuPc molecules do not differ significantly.

5.2.3 XSW analysis of F_{16} CuPc on CuPc/Ag(111)

After the measurement of CuPc on Ag(111) was completed, F_{16} CuPc was deposited on top and a second XSW data set was collected. Conventional LEED revealed that the F_{16} CuPc coverage was below one monolayer within the disordered phase regime (cf. Fig. 5.13). An exact coverage could not be estimated from LEED but from the change of the photoelectron yield of the C1s core level before and after the deposition of the second compound. This will be shown in the following.

Coverage estimation

Regarding the photoelectron yield, one has to consider the effect, that the signal from the first adsorbate layer (CuPc) will be damped by the molecules in the second layer (F_{16} CuPc). An attenuation of the incident X-ray photons can be neglected, since their mean free path in solid material is very large. The intensity $Y(d)$ of the photoelectrons, emitted from the CuPc layer, will be attenuated on its way through the F_{16} CuPc layer of thickness d before reaching the analyzer. This attenuation follows the Lambert-Beer law

$$Y(d) = Y_0 \cdot e^{-d/\lambda}, \quad (5.5)$$

with the initial intensity Y_0 and the material-dependent attenuation length λ , which is also called inelastic mean free path here. λ could in principle be estimated by measuring the photoelectron yield of F_{16} CuPc films of different known thicknesses. However, such a study is not reported in literature to our knowledge. In this work, the inelastic mean free path for electrons in F_{16} CuPc films is instead calculated from a semi-empirical formula reported by Seah and Dench [100]. The authors compared published values for λ of many different

materials and established expressions for the dependence of λ on the kinetic energy E_{kin} of the electrons for different material groups (elements, inorganic compounds, etc). For organic compounds, they arrived at

$$\lambda[\text{nm}] = 1000 \cdot \rho \cdot \left(\frac{49}{E_{kin}^2} + 0.11 \cdot \sqrt{E_{kin}} \right), \quad (5.6)$$

where ρ is the bulk density of the according material.

For $F_{16}CuPc$, we assumed a density of 2118 kg/m^3 , which is a value that was reported for a rather thick $F_{16}CuPc$ ribbon [101]. From Eq. 5.6, we calculated $\lambda = 2.52 \text{ nm}$ at an energy of $E_{kin} = 2351 \text{ eV}$, which corresponds to the C1s energy position. An experimental determination of an attenuation length has been performed recently for PTCDA/Ag(111) by Graber et al. [102] at kinetic energies up to 1500 eV . For the C1s binding energy, their formula leads to $\lambda = 4.69 \text{ nm}$, which is in the same order of magnitude as our value determined above.

XPS curves in the regions of the core levels of interest have been measured with high statistics for both the $CuPc$ layer and the final system with $F_{16}CuPc$ on top. The scans for the C1s region can be normalized, so that the background intensity is equal in both curves on both sides of the spectra, see Fig. 5.18 d). It is then found, that the total C1s photoelectron yield, given by the areas of the spectra after normalization to the same background level and background subtraction, had increased by $\approx 15\%$ after $F_{16}CuPc$ was deposited. Assuming a thickness of 3 \AA for a single $F_{16}CuPc$ layer, Eq. 5.5 yields, that the signal from those parts of the $CuPc$ monolayer which are covered by $F_{16}CuPc$ is reduced to $Y \approx Y_0 \cdot 89\%$ of its initial value. We will further assume, that the electron yield of a $CuPc$ molecule is equal to that of an $F_{16}CuPc$ molecule. The $F_{16}CuPc$ coverage is then simply $\Theta_2 = 0.15/0.89 = 0.17 \text{ ML}$.

XPS fit models

From SPA-LEED it was known that the stacked system shows signs of radiation damage after rather short times. To reduce a similar effect, the XSW analysis was only performed at $T \approx 50 \text{ K}$. By repeatedly performing short XSW scans on the same spot of the sample and checking the evolution of the coherent fraction in this spot, radiation damage was found to occur after $\approx 20 \text{ min}$ at this temperature. This again defines the limit for the acquisition time on one spot of the sample. A similar procedure as for $CuPc/Ag(111)$ was then followed for the measurements. High statistics XPS scans have been recorded to develop the according fit models, while shorter XPS scans were performed for the C1s, N1s and F1s core levels at photon energies around the Bragg energy. Scans on different spots of the sample were summed up in the subsequent analysis for each element.

Fig. 5.18 shows an overview of the XPS fit models for $F_{16}CuPc/CuPc/Ag(111)$, whose details will be discussed in the following.

- The F1s curve is simply fit by a linear background and a single peak.

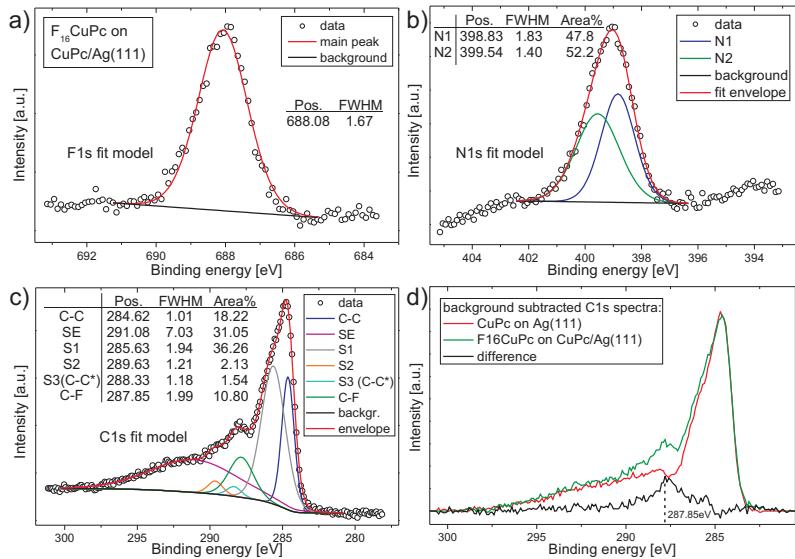


Figure 5.18: Fit models for the a) F1s, b) N1s, and c) C1s regions, taken at an off-Bragg photon energy of 2640 eV. d) shows a comparison of the background subtracted C1s spectra before and after the deposition of F_{16} CuPc.

Since all fluorine atoms are chemically equivalent and only present in the F_{16} CuPc molecules, one symmetric peak is expected.

- The N1s spectrum looks rather similar to the spectrum of CuPc/Ag(111) shown in Fig. 5.15 b). Again, two components are necessary to fit the main peak.

Nitrogen atoms are found in both the CuPc and the F_{16} CuPc molecules. Furthermore, chemically different pyrrole and azaporphyrine species exist in both cases, so that in total the spectrum should contain four different components. However, the energy resolution of the electron analyzer is not sufficient to resolve the small differences in E_B of the species from fluorinated and non-fluorinated molecules. Therefore, we use only two fit components for simplicity. Since these components are physically not meaningful, only the total region has been analyzed further.

- For C1s, all five components from the fit model of the CuPc/Ag(111) C1s spectrum have been adopted and a sixth component has been added.

Adopting the fit components from the CuPc/Ag(111) analysis is reasonable, since the XPS signal from the CuPc layer should not be changed too much by the adsorption of the F_{16} CuPc molecules. Especially since the F_{16} CuPc coverage was found to be only 0.17 ML, large parts of the CuPc

layer are still uncovered. The energy positions of the S2 and S3 components have been fixed before fitting. The sixth component (C-F) accounts for the main difference upon the adsorption of the $F_{16}CuPc$ layer. Its position is fixed to the maximum position of the difference between the XPS spectra before and after the adsorption of the 2nd layer, which is shown in Fig. 5.18 d). The C1s curves have been normalized, so that the background levels of both curves are identical on both sides of the region, and afterwards background subtracted. The main peak of the difference spectrum should describe those carbon atoms, which are bonded to fluorine and therefore considerably shifted in energy. Apart from this, the two C1s spectra show almost the same shape. The C-F peak is the only component, which stems from the 2nd layer only and is hence the most interesting part of the model. Unfortunately, the S3 satellite is located at almost the same binding energy, which complicates the XSW analysis. If both components S3 and C-F are left unconstrained, then their XSW results will contain contributions from both layers. Therefore, we decided to restrict the area of component S3 to a fixed percentage of the area of the C-C component. This is reasonable, if we assume S3 to be a shake-up satellite (C-C*) of the C-C peak. Their XSW signature should then be identical, which is ensured by the area constraint. In every fit model we tried, the C-C peak was found to be dominated by the 1st layer, judging from its XSW results. Therefore, S3 (C-C*) will also contain mainly 1st layer photoelectrons, which decouples the C-F peak from a 1st layer contribution at least to a large degree.

XSW results

At first, the results of the XSW analysis for the total regions are presented in Fig. 5.19. The interpretation of the F1s result is straightforward, as these photoelectrons can only stem from the $F_{16}CuPc$ layer. The coherent fraction of $F^H = 0.52$ means that this species shows a slight degree of disorder. However, it is very likely that the molecules adsorb flat lying on the CuPc layer in order to optimize the interactions between the π -systems of the two molecular species. For a tilted geometry, a considerably lower coherent fraction would be expected. As the LEED pattern corresponding to the LT phase was found to be rather disordered, different adsorption sites with slightly different adsorption heights are a possible reason for the observed value of F^H . The coherent position of $P^H = 0.62$ corresponds to an average adsorption height of $d^H = 6.18 \text{ \AA}$ above the Ag surface.

In contrast to F1s, the C1s and N1s regions contain contributions from both the CuPc and the $F_{16}CuPc$ layer, so that the according XSW results are basically an average of the two layers. Therefore, the coherent fractions of carbon and nitrogen are lower than for the CuPc monolayer while the coherent positions are higher for both species. All yield curves are again nicely fitted by the electron yield equation 2.6, containing only small error bars. As already mentioned, the true error of the XSW results is hard to quantify. The spread of the single

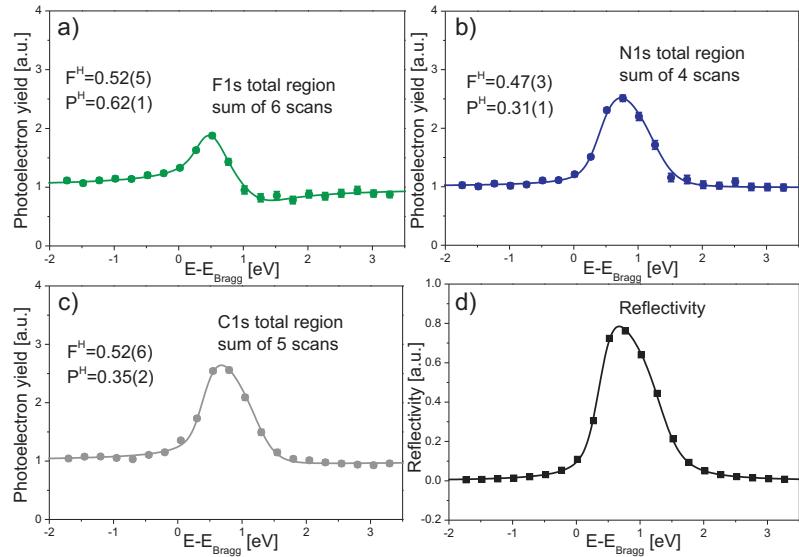


Figure 5.19: Results of the XSW analysis: Electron yield curves for the total a) F1s, b) N1s, and c) C1s regions are shown together with the according fits and the resulting fit parameters. d) shows a typical reflectivity curve.

measurements around the results for the summed up yield curves can be used to quantify this. Such a spread can be nicely visualized in an Argand diagram, as it is shown in Fig. 5.20. Here, the XSW results of the single electron yield curves are denoted as open circles in different colors for the C1s, N1s and F1s total regions. Closed circles represent the according results of the summed up yield curves. It can be seen, that the single F1s results lie very closely around the sum result, especially regarding the coherent position (i.e. the polar angle). The spread of the single measurements is larger for the N1s region and even more for C1s. A possible explanation would be an inhomogeneous F_{16} CuPc coverage on the sample. Because the measurements were conducted on different spots on the sample, a different local coverage would lead to different N1s and C1s results, since they represent averages from both layers. The F1s core level electrons stem only from the second layer, so that the according XSW results would not be effected by this. The standard deviations of the fit parameters F^H and P^H of the single scans as well as of the resulting d^H will be taken as error bars for the sum results in the following.

Since the fit results for the total C1s region were not very meaningful, we tried to extract some additional information from an XSW analysis of the single fit components. As already discussed, at least the C-F peak should originate from the 2nd layer only and hence produce XSW results similar to F1s. Fig. 5.21 shows the electron yield curves obtained for the separately analyzed C1s com-

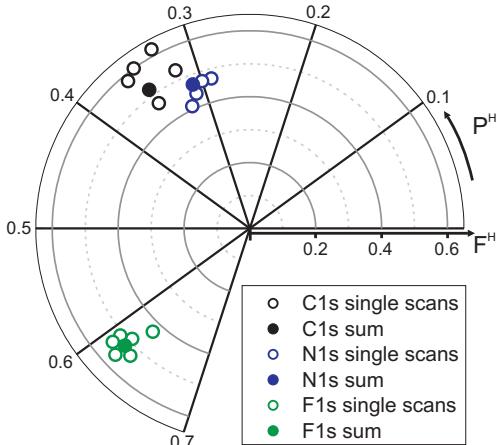


Figure 5.20: Argand diagram showing the XSW results for the total C1s, N1s and F1s regions. Open circles mark single measurements, while the results of the according sum of scans are shown as closed circles.

ponents. As already mentioned, the resulting coherent position and fraction for the C-C peak are very close to the C1s result for CuPc/Ag(111) described above. Therefore it is confirmed, that this component is dominated by the 1st layer. The coherent positions of the broad SE component and of S1 are both higher than 0.31. Hence, they probably contain a small contribution from 2nd layer molecules. As expected, the results of $F^H = 0.40 \pm 0.08$ and $P^H = 0.54 \pm 0.02$ for C-F clearly differ from the other components. The corresponding adsorption height is estimated as $d^H = (5.99 \pm 0.05)$ Å. This is 0.19 Å below the value for the fluorine atoms, which is comparable to the height difference between C and F found for $F_{16}CuPc/Ag(111)$ [61]. This could be interpreted as a similar bending with fluorine pointing away from the surface, as was also found for F4-TCNQ/Cu(111) [103]. However, the C-F peak used in our fit model might still contain contributions from the 1st layer, so that the adsorption height could be underestimated. The rather low coherent fraction might be an indication for this.

Vector construction

Since the XSW results of the 1st layer are known from the separate measurement of the CuPc monolayer, a different type of analysis becomes possible. Assuming that the photoelectron yield of the CuPc monolayer is not changed by the 2nd layer (apart from the damping described above), the XSW result of the total system can be deconvoluted to obtain the contribution of the $F_{16}CuPc$ part. This corresponds to a simple vector analysis in the Argand diagram, since the contributions from the different layers, $Y_{F_{16}CuPc}$ and Y_{CuPc} , can simply be added

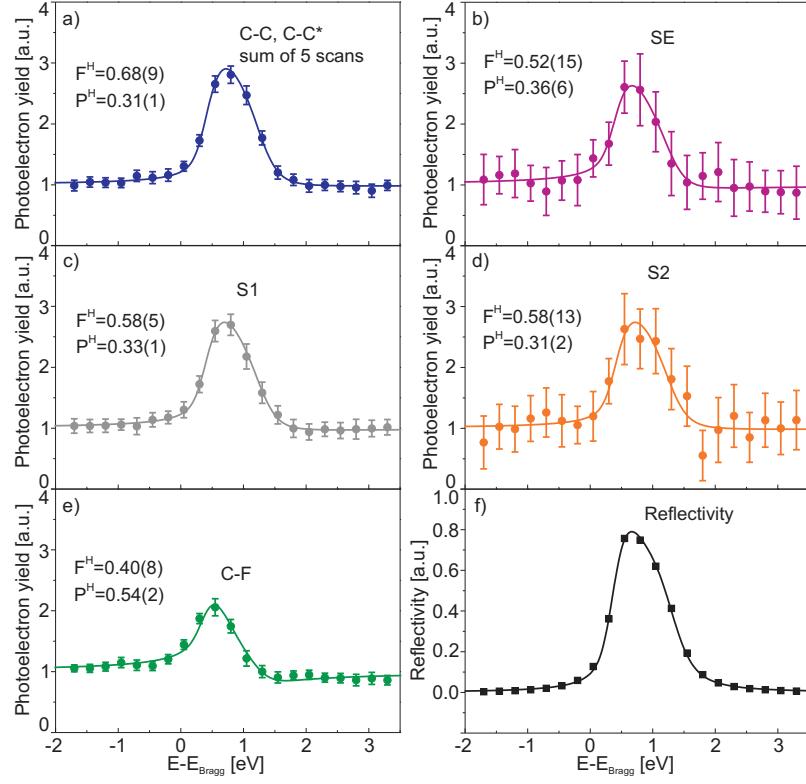


Figure 5.21: a)–e) Resulting electron yield curves and f) reflectivity curve from the XSW analysis of the single C1s components. The C-F component shows a considerably different XSW signature.

up by summing their corresponding vectors.

$$Y = a \cdot Y_{F_{16}\text{CuPc}} + (1 - a) \cdot Y_{\text{CuPc}} \quad (5.7)$$

Fig. 5.22 shows this analysis for the N1s and the C1s results.

With the knowledge of the 2nd layer coverage Θ_2 and the strength of the attenuation of the 1st layer calculated above, the $F_{16}\text{CuPc}$ fraction a of the total electron yield can be estimated as

$$a = \Theta_2 / [(1 - \Theta_2) + \Theta_2 \cdot \exp(-d/\lambda) + \Theta_2] = 14.69\%. \quad (5.8)$$

Therefore, the vector of the CuPc monolayer result Y_{CuPc} is multiplied by $(1 - a)$ to achieve the CuPc contribution to the XSW signal of the total system. Completing the parallelogram given by the total signal and the CuPc part, the $F_{16}\text{CuPc}$ contribution is constructed. Finally this vector is multiplied by $1/a$ to obtain the vector for the separated 2nd layer $Y_{F_{16}\text{CuPc}}$. This construction leads

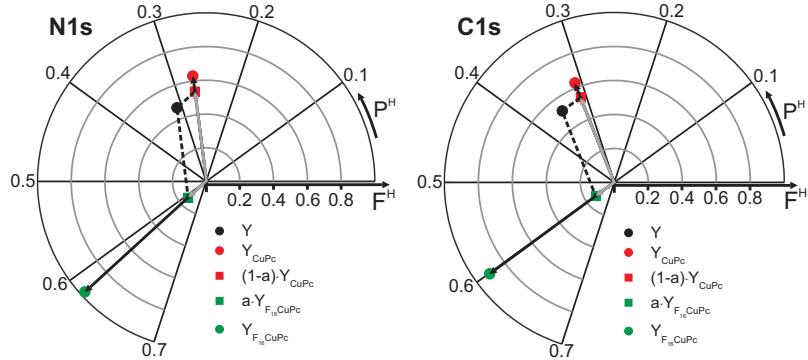


Figure 5.22: Vector construction for deconvoluting a) the N1s and b) the C1s XSW results into the single components from the CuPc and $F_{16}CuPc$ layers. The $F_{16}CuPc$ part is gained by completion of the parallelogram given by the total signal and the CuPc part.

to values of $F^H = 0.97$ and $P^H = 0.62$ for N1s and $F^H = 0.91$ and $P^H = 0.60$ for C1s, respectively. The coherent positions as well as the corresponding adsorption heights of 6.18 \AA and 6.14 \AA for N1s and C1s, respectively, are in good agreement with the XSW results for the fluorine atoms. In contrast to the result for the C-F carbon component, these values indicate that the $F_{16}CuPc$ molecules are rather flat lying than bent, when adsorbed on $CuPc/Ag(111)$.

It should be noted, that the results of the vector construction depend on the attenuation of the 1st layer photoelectrons by the 2nd layer, which was only roughly estimated. However, by trying different values for the attenuation strength, the error could be estimated. We found that only the coherent fraction is strongly influenced by changes of this value. This value seems to be generally overestimated in the vector constructions. The more interesting fit parameter P^H is only slightly affected as long as the true attenuation does not differ very strongly from the estimation.

Finally it should be mentioned, that the adsorption of a 2nd layer might change the vertical order of the atomic species in the CuPc interlayer slightly. This was e.g. observed for CuPc on PTCDA/Ag(111) [10] by a change of the PTCDA adsorption height upon CuPc adsorption, but cannot be considered in this type of vector analysis performed here. Furthermore, the measurement on CuPc/Ag(111) was performed at RT, while the stacked system was investigated at LT. However, the measurements of Kröger et al. [45] showed, that the adsorption heights as well as the coherent fractions of the atomic species in CuPc/Ag(111) do not change significantly upon cooling.

Vertical adsorption geometry

The resulting vertical adsorption geometry is sketched in Fig. 5.23. The ad-

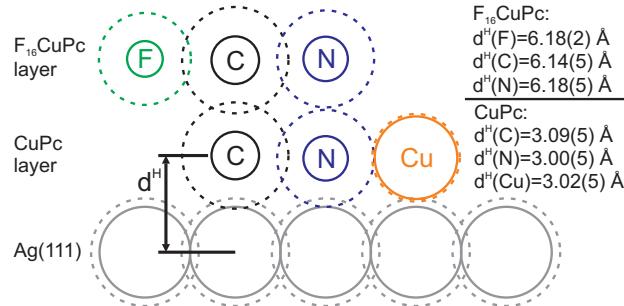


Figure 5.23: True-scale image, showing the resulting adsorption heights of the investigated atomic species in F_{16} CuPc on CuPc/Ag(111). The solid circles represent covalent bonding radii, while the dashed circles are van-der-Waals radii.

sorption heights d^H of the elements in the CuPc monolayer as well as in the F_{16} CuPc layer, calculated from Eq. 2.7, are drawn on the same scale as the atomic radii. Both the covalent and the van-der-Waals radii [104] are shown by the solid and dashed circles, respectively. A position for the Cu atoms in F_{16} CuPc is not given, since this was not measured. For the CuPc layer, the van-der-Waals radii of carbon and nitrogen clearly overlap with the Ag surface atoms, which indicates the well known weakly chemisorptive bonding character of CuPc/Ag(111). A significant overlap of van-der-Waals radii between atoms in the F_{16} CuPc molecule and atoms in the CuPc molecule is also possible but only if carbon atoms are involved and for precise on-top adsorption.

Such a configuration is possible from the electrostatic and van-der-Waals interactions, as shown in Fig. 5.24. This figure shows a pair potential map calculated for F_{16} CuPc on CuPc in analogy to Fig. 5.1 a). A vertical distance of $\Delta z = 3.1$ Å between the two molecules was set, which is the optimum stacking distance found in the calculation for Fig. 5.1 b). The global energy minimum is found here for molecules lying on top of each other with equal orientation. This is not necessarily the only favored F_{16} CuPc adsorption site, as only one molecule in the 1st layer is taken into account. However, it shows that a configuration with e.g. carbon atoms of both species facing each other is possible. In the pair potential calculation, this is probably stabilized by electrostatic attraction between fluorine and hydrogen atoms. Such an attraction also speaks against a possible upwards bending of the fluorines.

The stoichiometry of the atoms in the molecules is C:H(F):N:Cu=32:16:8:1. Considering this, one can define a weighted average adsorption height d_{av}^H from the available XSW results of the single atomic species. This results in $d_{av}^H(\text{CuPc}) = 3.07$ Å and $d_{av}^H(F_{16}\text{CuPc}) = 6.16$ Å. Therefore, the average distance between the two organic layers is $\Delta d_{av}^H = 3.09$ Å, which is close to the calculated optimum stacking distance of $\Delta z = 3.1$ Å. Interestingly, this is clearly below the weighted average of $d_{av}^H = 3.32$ Å for F_{16} CuPc on Ag(111) calculated

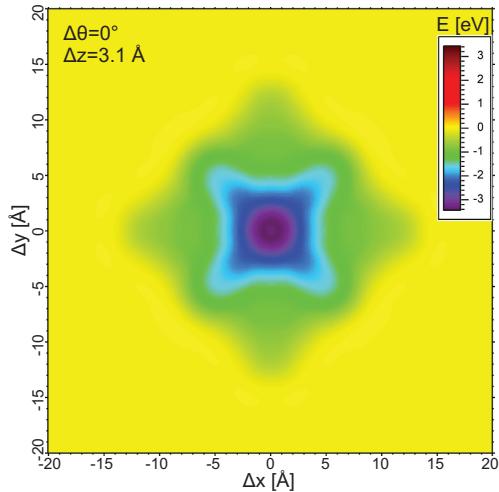


Figure 5.24: Pair potential map for the interaction of a CuPc molecule with an $F_{16}CuPc$ molecule, shifted by $\Delta z = 3.1 \text{\AA}$.

from the data in reference [61]. The layer difference, found for the components in this organic–organic interface, is comparable to adsorption heights in organic–metal systems, which are not purely physisorbed, e.g. CuPc/Ag(111) [45] or NTCDA/Ag(111) [105, 106].

5.2.4 Conclusion

The hetero-organic interface of $F_{16}CuPc$ on CuPc/Ag(111) has been investigated by SPA-LEED and XSW. $F_{16}CuPc$ initially grows in rather disordered structures, but forms an ordered structure when its layer is closed. A commensurate relation between the ordered superstructure and the CuPc interlayer was found (within error bars), indicating that an unusually strong interaction between the organic layers is possible. To characterize the interaction strength, an XSW measurement has been performed on this system. For comparison, an XSW data set of CuPc/Ag(111) was collected first, yielding results similar to a previous study [45]. Afterwards, $F_{16}CuPc$ was deposited and a second measurement was done. XSW results were obtained for the F1s, C1s and N1s core level regions of the system. While F was only present in the $F_{16}CuPc$ layer, the C1s and N1s data had to be deconvoluted into the 1st layer and 2nd layer contributions by a vector construction. All three atomic species yielded similar adsorption heights, so that $F_{16}CuPc$ adsorbs flat lying on CuPc/Ag(111). An average distance of 3.09\AA to the CuPc layer was found, which indicates that an overlap of wavefunctions between atomic species in the different organic layers is possible. This would result in a weakly chemisorptive interaction between the molecules, probably facilitated by their stacked π -systems. Such a rather strong

interaction might enable the commensurate registry between the layers found with SPA-LEED. However, the interaction can not be strongly chemisorptive and/or site specific, since the ordered structure could easily be destroyed by moderate temperatures or by radiation damage.

6 $F_{16}CuPc$ on PTCDA monolayers on Ag(111)

In this chapter, the results of the investigation of $F_{16}CuPc$ on a closed monolayer of PTCDA on the Ag(111) surface are presented. These results shall be compared to those of CuPc on PTCDA/Ag(111) [10] and of $F_{16}CuPc$ on CuPc/Ag(111) discussed in chapter 5.2 to further improve the understanding of hetero-organic interfaces.

3,4,9,10-perylenetetracarboxylic-dianhydride (PTCDA) on Ag(111) is one of the most intensively investigated organic–metal interfaces [7]. The molecular structure, calculated from DFT for a free molecule, is shown in Fig. 6.1 b). It consists of two anhydride groups attached on opposite sides of an aromatic perylene core. In contrast to phthalocyanines, PTCDA molecules show intermolecular attraction on Ag(111) at RT, resulting in island growth at submonolayer coverages. The same structure is also maintained when the monolayer is closed. The molecules arrange in a herringbone structure with two molecules per unit cell [36, 65]. This superstructure is described by a commensurate matrix of

$$M = \begin{pmatrix} 7 & 1 \\ 2 & 5 \end{pmatrix} \quad (6.1)$$

which yields a unit cell with $|\vec{A}| = 18.96 \text{ \AA}$ and $|\vec{B}| = 12.61 \text{ \AA}$, including an angle of 89° and an area of 238.7 \AA^2 in real space. From XSW [30], STM/STS [85] and UPS [107] it is known that the molecules are chemisorbed on this surface. PTCDA is more strongly bonded to the Ag(111) surface than CuPc, judging from its smaller adsorption height [30, 45]. This should also influence the structure formation of higher layers.

In the work of Benjamin Stadtmüller, mixed systems of PTCDA and CuPc within the first monolayer have been investigated as well as stacked hetero-systems [108]. For the stacked system, the surprising result was that CuPc adsorbs with a commensurate registry to the underlying PTCDA monolayer on Ag(111) [10]. This indicates that the interaction between the components of this hetero-organic system is unexpectedly strong. Usually, a pure physisorption due to van-der-Waals forces is expected for interactions at organic–organic interfaces.

In chapter 5.2 we reported about a relation between $F_{16}CuPc$ and a closed CuPc layer below, which is also commensurate within error bars. However, the corresponding ordered phase was quite unstable and the registry with the Ag substrate was not commensurate but point-on-line. In this chapter we now choose PTCDA as a different interlayer which exhibits a stronger and more site specific bonding to the Ag(111) surface to study the effect on the organic–organic

interactions.

6.1 Structural phase diagram

Each experiment in this chapter started with preparing a monolayer film of PTCDA on Ag(111), which could be done by a simple annealing procedure. A

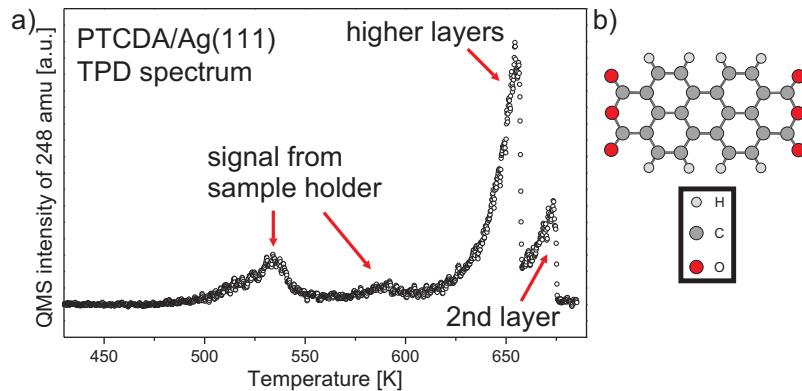


Figure 6.1: a) Typical TPD spectrum showing the desorption of a PTCDA multilayer from a Ag(111) crystal. b) Gas-phase structure of PTCDA calculated by DFT.

multilayer film of PTCDA was deposited onto the freshly cleaned silver crystal. Afterwards, the monolayer structure was produced by heating the crystal up. The higher PTCDA layers could be desorbed from the sample while the close packed first layer remained, showing the same structure as a directly prepared monolayer. Annealing from a multilayer film has the advantage that the deposition rate and the initial coverage do not have to be known precisely. This procedure was controlled by TPD while increasing the temperature of the sample by ≈ 1 K/s, as shown in Fig. 6.1 a). Thereby the ion current of the well known PTCDA fragment at $m/z = 248$ amu [109] was monitored by the mass spectrometer. In the IC vs T spectrum, two main peaks appear that can be attributed to the desorption of the 2nd layer and the higher layers, respectively. After the 2nd layer was completely desorbed, the signal dropped to background very quickly, indicating zero-order desorption kinetics. Note that the additional QMS signals at $T \approx 530$ K and $T \approx 590$ K are artifacts stemming from PTCDA molecules which did not desorb from the sample crystal but from parts of the sample holder that are closer to the heating filament. Qualitatively, the shape of this TPD curve fits to a previous study [65], although the desorption temperatures were considerably higher in our case. However, temperature measurements on different sample holder systems are not comparable on a quantitative scale.

Deposition of $F_{16}CuPc$ onto the substrate of 1 ML PTCDA on Ag(111) was

6.1 Structural phase diagram

controlled in a similar manner as for the systems investigated in the previous chapters. The sample was repeatedly checked with SPA-LEED scans during deposition and the QMS signal of 200 amu was monitored simultaneously.

Figure 6.2 shows a series of SPA-LEED diffractograms that were recorded during the deposition of $F_{16}CuPc$ onto a monolayer film of PTCDA on Ag(111) at intervals of 1 min. The first important observation is that the spots of the

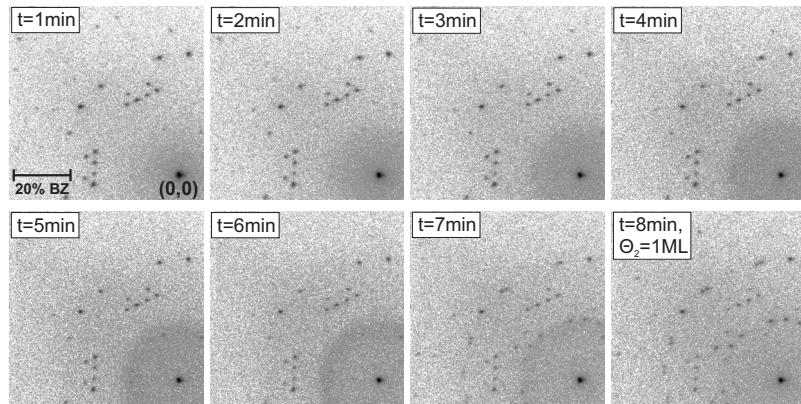


Figure 6.2: Series of SPA-LEED images recorded in-situ during deposition of $F_{16}CuPc$ onto a monolayer of PTCDA on Ag(111). ($E=30$ eV)

PTCDA monolayer (see e.g. image in the upper left) did not disappear or shift during the deposition. This means that the lateral order of the PTCDA layer remained unchanged and no intermixing of PTCDA and $F_{16}CuPc$ occurred at RT. Only the intensity of these spots decreased due to damping by the growing second layer. Diffracted intensity from the $F_{16}CuPc$ film showed up in a similar fashion as in the case of deposition onto a clean Ag(111) surface. At first, a diffuse circular intensity around the $(0,0)$ -spot appeared at RT in addition to the PTCDA spots. In the example in Fig. 6.2, this circle became ring-like after five minutes of deposition. This can be interpreted as a preferred intermolecular distance in a disordered structure in analogy to the $F_{16}CuPc$ /Ag(111) system. After seven minutes, sharp new spots appeared in the image and after eight minutes the diffuse ring was gone. Hence, the molecules had arranged into an ordered layer. The critical ring radius shortly before the phase transition started corresponds to an average intermolecular distance of (17 ± 0.5) Å. Comparing with the values found in chapter 4, the critical molecular density of the $F_{16}CuPc$ film is lower than for $F_{16}CuPc$ /Ag(111).

The intensity of the specular $(0,0)$ -spot oscillated due to interference between the electrons diffracted from the closed PTCDA layer and from the $F_{16}CuPc$ molecules on top, respectively. The electrons from the two levels did not interfere completely destructive, because the two types of molecules are not equivalent scatterers and because the electron energy of 30 eV does not precisely correspond to an out-of-phase condition. Consequently the $(0,0)$ -spot did not vanish, but

minima and maxima could still be seen. When the deposition was continued until the new superstructure spots appeared at RT, the (0,0)-intensity reached a new maximum analog to the deposition onto the bare Ag substrate. Therefore we assign a coverage of ≈ 1 closed layer on top of PTCDA/Ag(111) to this $F_{16}CuPc$ amount. The deposited flux, characterized by the integrated QMS signal, also fits very well to the amount needed to deposit a monolayer of $F_{16}CuPc$ on Ag(111), which shows that the sticking coefficient must be very similar.

Longer scans for higher statistics have been performed to analyze the system in more detail at RT as well as at a temperature of 100 K. The results are

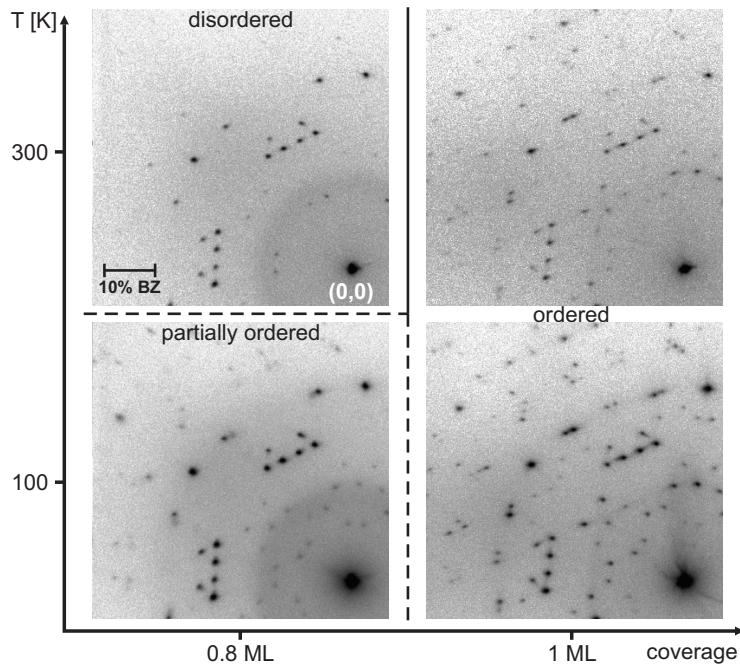


Figure 6.3: The structural phase diagram of $F_{16}CuPc$ on PTCDA/Ag(111) for different coverages and temperatures. ($E=30$ eV)

summarized in the structural phase diagram in Fig. 6.3. When a sample with a coverage below 1 ML of $F_{16}CuPc$ on PTCDA/Ag(111) was cooled to liquid nitrogen temperature, the diffuse ring-like intensity described above partially changed into an ordered, six-fold symmetric spot pattern regarding the spot positions, which were the same as for higher coverages at RT. This means that a part of the $F_{16}CuPc$ molecules condensed into ordered islands upon cooling. Since the ring-like feature did not disappear completely, there must have been disordered regions left, coexisting with the islands. This could mean that either the diffusivity of the $F_{16}CuPc$ molecules is lower than on Ag(111), or that the sample temperature was only slightly below the phase transition temperature.

In the latter case, the diffuse intensity should vanish at sample temperatures below 100 K, which could not be achieved in our SPA-LEED chamber. At a coverage of 1 ML, the same additional spots were visible at RT and only their intensity increased considerably when the sample was cooled. In conclusion, the phase diagram is quite similar to that of $F_{16}CuPc$ on Ag(111) shown in chapter 4. A disordered phase exists for submonolayer coverages of $F_{16}CuPc$ on the substrate (which is here PTCDA/Ag(111)). A disorder-to-order phase transition occurs when the coverage approaches a closed layer at RT, or when the submonolayer film is cooled. Both transitions result in the same ordered structure. However, for $F_{16}CuPc$ on PTCDA/Ag(111), a considerable part of the adsorbate film was found to remain disordered for submonolayer coverages upon cooling to liquid nitrogen temperature.

6.2 LEED model

Naively, one might expect the spot pattern of $F_{16}CuPc$ on PTCDA/Ag(111) to be a superposition of the PTCDA monolayer pattern and a second one due to the ordered $F_{16}CuPc$ layer on top. Instead of this, we found that all spots are well

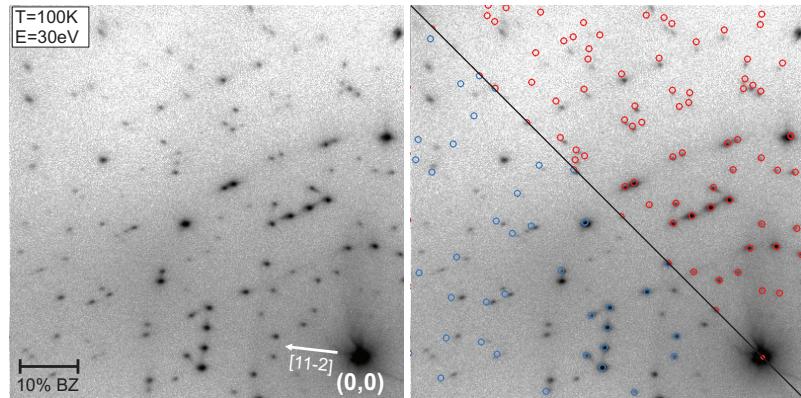


Figure 6.4: SPA-LEED image of ≈ 1 ML $F_{16}CuPc$ on PTCDA/Ag(111). The same image is shown again on the right, superimposed with simulated LEED spots for two unit cells. The blue circles mark spots of the PTCDA/Ag(111) unit cell. However, the red spots from the proposed unit cell describe both the PTCDA spots and the additional spots which appeared after the phase transition.

described by one single unit cell as shown in Fig. 6.4. The blue circles in the right image represent LEED spots calculated for the well known PTCDA/Ag(111) unit cell, while the proposed unit cell (red circles) describes both the PTCDA and the additional spots, which appeared after the phase transition. This cell

is commensurate and has a superstructure matrix of

$$M = \begin{pmatrix} 7 & 1 \\ 4 & 10 \end{pmatrix}. \quad (6.2)$$

Its dimensions in real space are $|\vec{A}| = 18.95 \text{ \AA}$, $|\vec{B}| = 25.19 \text{ \AA}$, including an angle of 89° . As can be seen from these numbers, the unit cell is twice as large as the PTCDA/Ag(111) cell given by Eq. 6.1, since the unit cell vector \vec{B} has doubled. This means that the closed $F_{16}CuPc$ layer orders in a (1×2) superstructure with respect to the unit cell of the PTCDA layer underneath. Equivalent $F_{16}CuPc$ molecules occupy sites that are separated by twice the length of the according PTCDA unit vector, which produces half-order LEED spots in this direction. The area of the (1×2) supercell of 477.39 \AA^2 lets us assume, that it contains two $F_{16}CuPc$ molecules. For comparison, the area of an $F_{16}CuPc$ molecule is given by one quarter of the unit cell area of $F_{16}CuPc/\text{Ag}(111)$ which equals 227.84 \AA^2 .

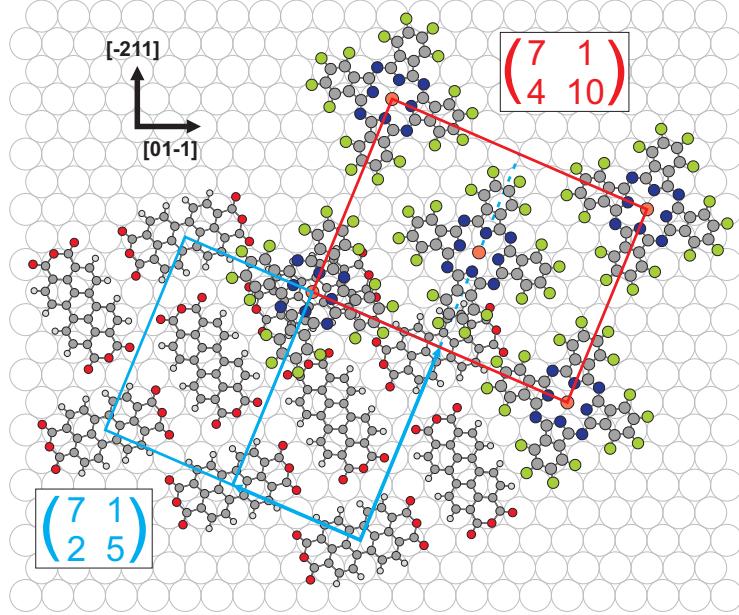


Figure 6.5: Real space model for the adsorption of $F_{16}CuPc$ on a monolayer of PTCDA on Ag(111). The commensurate relation in connection with two non-equivalent molecules per unit cell leads to a doubling of the PTCDA unit cell.

On the basis of these results, we propose a structural model for the $F_{16}CuPc$ adsorption on PTCDA/Ag(111) as shown in Fig. 6.5. While the structure of the PTCDA monolayer is well known from literature [36, 85], adsorption sites

and orientations of the $F_{16}CuPc$ molecules are arbitrarily chosen. It can easily be seen that a (1×1) superstructure of $F_{16}CuPc$ is not possible due to sterical reasons, since the smaller vector of the PTCDA unit cell is shorter than the dimensions of the $F_{16}CuPc$ molecule. Therefore, neighboring $F_{16}CuPc$ molecules in the direction of \vec{B} would overlap. Consequently, the molecules must adsorb in two non-equivalent adsorption sites with respect to the PTCDA lattice, which results in a (probably centered) $c(1 \times 2)$ superstructure. An additional (1×2) reconstruction of the PTCDA layer, induced by the $F_{16}CuPc$ adsorbate, is possible. However, this can not be confirmed or disproved by our SPA-LEED measurements.

It is remarkable that the $F_{16}CuPc$ adsorbate film shows a clearly commensurate registry on the PTCDA/Ag(111) substrate, while on clean Ag(111), commensurability was found to be probable but could not be unambiguously confirmed. This points to a rather strong interaction of $F_{16}CuPc$ with the PTCDA layer underneath or with the total substrate of PTCDA/Ag(111). As mentioned before, such strong interactions in a hetero-organic system are quite unusual, since typically weak physisorptive bonding is observed in these cases. The commensurate registry found here is a sign for a site specific, not purely physisorptive interaction.

This finding would have to be confirmed by other experimental techniques, e.g. UPS or XSW. From the adsorption heights measured in XSW a statement about the interaction strength can be made. If the difference in adsorption height between the molecules in two different layers is found to be considerably smaller than the sum of van-der-Waals radii of the atomic species, a strong interaction including charge transfer can be expected. Otherwise the interaction is probably physisorptive. The charge transfer, proving a covalent bonding character, should of course also be visible directly in UPS measurements. In many cases this was observed for organic molecules on metal substrates by the appearance of an occupied state of the adsorbate directly at the Fermi-level which was unoccupied before adsorption, but has been filled by the interaction with the substrate (F-LUMO).

As already mentioned in the beginning of the chapter, a similar principal behavior was recently reported for CuPc on PTCDA/Ag(111) [10]. When the CuPc layer is not closed, it also forms disordered structures that condense into ordered islands upon cooling. When the CuPc layer is closed, the same additional superstructure LEED spots show up at RT. Also in this system, all spots could be explained by one commensurate unit cell. However, the relation between the unit cell of CuPc on PTCDA/Ag(111) and that of PTCDA/Ag(111) is more complicated, originating from a large unit cell containing 6 CuPc and 10 PTCDA molecules. It was confirmed by XSW and UPS results [10], that the interaction between the two layers of CuPc and PTCDA can not be purely physisorptive.

Both molecular species, CuPc and $F_{16}CuPc$, show a similarly strong vertical bonding to the PTCDA layer despite their different types of terminating atoms. This suggests that a site specific interaction to PTCDA is probably mediated

by the similar aromatic bodies of the molecules via π -stacking mechanisms.

Stability of the structure

The effect of annealing the sample after deposition has been investigated and is discussed in the following. Therefore, 1.1 ML $F_{16}CuPc$ were deposited onto

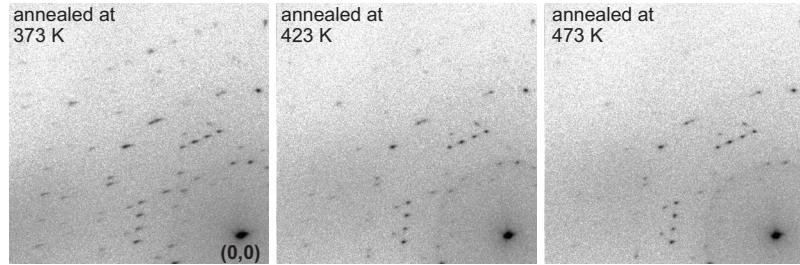


Figure 6.6: SPA-LEED images of 1.1 ML $F_{16}CuPc$ on PTCDA/Ag(111) at RT after annealing the sample at $T=373$ K, 423 K and 473 K, respectively. ($E=30$ eV)

PTCDA/Ag(111) and the sample was stepwise annealed at increasing temperatures of 373 K, 423 K and 473 K. After each annealing step, the sample was cooled to RT again, and measured by SPA-LEED as shown in Fig. 6.6.

While almost no change in the spot pattern was observed after annealing at 373 K, the additional superstructure spots stemming from the adsorbed $F_{16}CuPc$ became clearly weaker after the 423 K step. After the last step at 473 K, they had become very faint. Instead, ring-like intensity appeared, resembling the diffuse ring observed during deposition before the spots evolved. This could be interpreted as a partial desorption of the $F_{16}CuPc$ layer. However, no signal at 200 amu could be observed in the QMS for temperatures ≤ 473 K. This behavior is similar to that found for $F_{16}CuPc$ on Ag(111), see chapter 4. One possibility is, that the molecules are destroyed by the annealing process. Alternatively, $F_{16}CuPc$ could have been desorbed with a very low desorption rate, which is not detectable by the QMS but enough to result in a disordered 2nd layer.

In contrast to this, the spots of the PTCDA monolayer were found to be preserved even after annealing at high temperatures. This emphasizes, that the PTCDA monolayer is so stable, that $F_{16}CuPc$ does not diffuse into the first layer even at elevated temperatures. The reason for this might be that PTCDA is more strongly bound to Ag(111) than $F_{16}CuPc$. This can be concluded from the adsorption height of PTCDA on Ag(111) [30], which is considerably lower than that of $F_{16}CuPc$ [61], as measured by XSW. Also the growth of PTCDA in commensurate islands is a sign for a strong interaction with the substrate as well as a strong attractive intermolecular interaction. $F_{16}CuPc$ on the other

hand was found to form a dilute gas-like phase for submonolayers, as discussed in chapter 4. Hence, the binding of PTCDA to the silver substrate appears to be considerably more site specific (and hence also stronger) than that of $F_{16}\text{CuPc}$. Therefore, molecule–substrate interactions between Ag and PTCDA seem to be advantageous in the stacked hetero-organic systems. However, it should be noted that for organic heterostructures of SnPc on PTCDA/Ag(111), it was found that a thick film of SnPc completely pushes PTCDA out of the 1st layer when the sample is annealed [110]. Since SnPc is also weaker bonded to the Ag(111) surface than PTCDA (except for the Sn atom in Sn-down geometry), the same argumentation fails for this system.

To further quantify these findings, the structure formation was also analyzed from the aspect of adsorbate–adsorbate interactions. The pair potential between

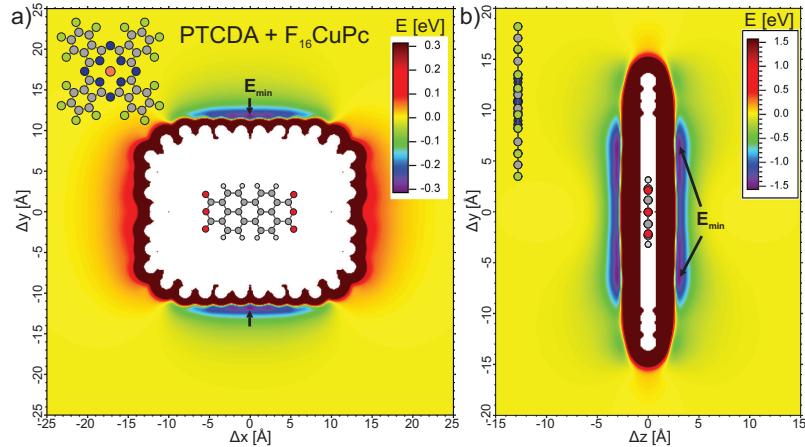


Figure 6.7: Pair potential maps for PTCDA and $F_{16}\text{CuPc}$ in a) lateral and b) stacked geometry. Slightly attractive regions are found in a) together with repulsive regions. In the stacked geometry, considerably deeper energy minima are found.

one PTCDA and one $F_{16}\text{CuPc}$ molecule in lateral and stacked geometries was calculated in analogy to calculations in the previous chapters. In the stacked case, energy minima of $E \approx -1.5$ eV were found, see Fig. 6.7 b). In the lateral map shown in Fig. 6.7 a), repulsive regions were found for configurations in which fluorine and oxygen atoms face each other, since both species carry negative partial charges. Attractive regions also exist, but the minima are rather shallow with $E \approx -0.3$ eV. This seems consistent with the finding that $F_{16}\text{CuPc}$ stays in the second layer on top of PTCDA/Ag(111). The energy minimum of a lateral arrangement of $F_{16}\text{CuPc}$ and PTCDA is considerably shallower than the minima of the stacked arrangement and also shallower than the potential minimum of $E = -0.58$ eV of the lateral interactions between two PTCDA molecules, calculated in reference [32]. Therefore, it might be speculated that an inter-

mixing is energetically also less favorable when intermolecular interactions are considered. On the other hand, this simple energetic argument fails to explain why intermixing happens in the related systems SnPc on PTCDA/Ag(111) and CuPc on PTCDA/Ag(111) after annealing.

The optimum stacking distance between $F_{16}CuPc$ and PTCDA, given by the position of the minima in Fig. 6.7 b), was found at $\Delta z = 3.0 \text{ \AA}$.

6.3 Layer distance

In chapter 5.2, the interaction strength between the two organic layers $F_{16}CuPc$ and CuPc could be quantified by XSW, yielding the adsorption heights of the involved atomic species. Similar measurements have not been performed for $F_{16}CuPc$ on PTCDA/Ag(111) in the scope of this work. However, the organic–organic layer distance could be extracted from LEED measurements as will be shown in the following.

The dependence of the (0,0)-spot intensity on the scattering phase can be used to determine energies at which out-of-phase and in-phase scattering conditions between the two adsorbate layers are given. To this extent, profiles of the (0,0)-spot have been recorded at LT along the $[\bar{1}01]$ direction at different electron energies as shown in Fig. 6.8. At LT, the $F_{16}CuPc$ molecules were found

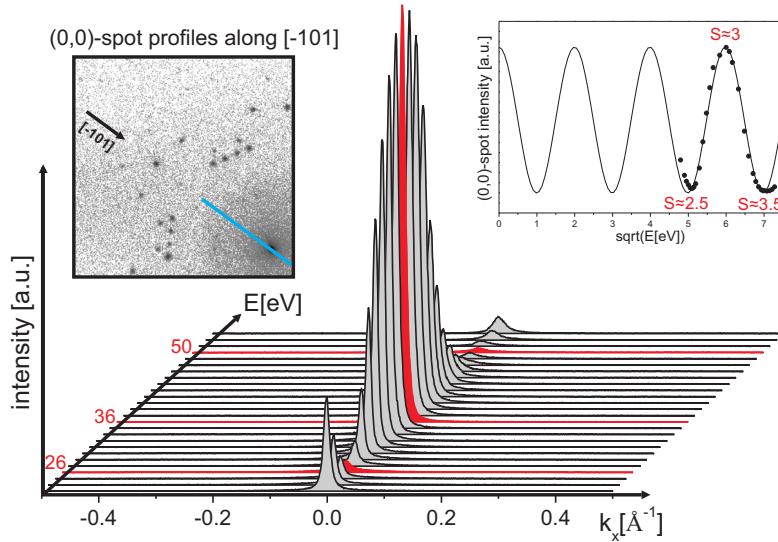


Figure 6.8: 1D SPA-LEED scans through the (0,0)-spot at different energies. The cosine dependence of the central spike intensity on the energy is nicely demonstrated in the inset.

to form islands, so that two types of regions are present on the surface. Regions in which PTCDA is covered by F₁₆CuPc molecules coexist with uncovered regions. As the total thickness of the organic film differs for F₁₆CuPc-covered and uncovered regions (by approx. the layer distance between the two types of molecules), interference effects of electrons scattered (or reflected) by the two regions occur. Since ≈ 0.5 ML of F₁₆CuPc were deposited, so that equal areas of the PTCDA layer were covered and uncovered, the destructive interference was clearly detectable for out-of-phase conditions. Several linescans are shown between 23 eV and 53 eV, which is the energy region for which the lense settings of the SPA-LEED instrument were optimized. The intensity I_{central} of the central (0,0)-reflection in a two layer system should follow a cosine dependence on the scattering phase $S \propto \sqrt{E}$, which can be expressed by

$$I_{\text{central}} = f \cdot (1 - 2\Theta_2(1 - \Theta_2)[1 - \cos(2\pi S)]), \quad (6.3)$$

see reference [13]. Here, f is the scattering factor and Θ_2 is the coverage in the 2nd layer. This cosine dependence can qualitatively be seen in Fig. 6.8. Two minima and one maximum of the intensity could be identified at 26 eV, 50 eV and 36 eV, respectively (red curves). Even for the minima, the (0,0) spike did not completely vanish. One reason for this is that the coverage was not precisely half of a complete layer. Even more important, the two types of molecules are not equivalent scatterers. Therefore the interference will never be completely destructive. Perfect destructive interference will only be observed if both layers contain the same type of molecules as was, e.g., demonstrated for C₆₀ on C₆₀(111) [111]. Nevertheless, the maximum at $E = 36$ eV corresponds to the maximum achievable constructive interference between the PTCDA layer and the F₁₆CuPc layer. From a cosine fit to I_{central} vs \sqrt{E} , the maximum was found to be the 3rd maximum of the cosine, as can be seen in the inset of Fig. 6.8. Hence the scattering phase is $S = 3$ at this energy. Accordingly, the minima at $E = 26$ eV and at $E = 50$ eV correspond to $S = 2.5$ and $S = 3.5$, respectively. It should be noted that the spot intensity did not increase as strongly after the latter minimum as it did before. The reason is probably that the beam intensity produced by the electron gun depends of the electron energy. From Eq. 4.1, the height difference d between the two layers could be calculated. The three extrema yield an average of $d = (3.04 \pm 0.10)$ Å, which is a typical value for the adsorption height of organic adsorbates on substrates with medium interaction strength, cf. CuPc/Ag(111) [45], Azobenzene/Ag(111) [112] or NTCDA/Ag(111) [105]. The value is also comparable to the optimum stacking distance calculated in Fig. 6.7 b). As the SPA-LEED measurements are not element specific, the result must be interpreted as an average adsorption height of a total molecule. No information about a possible bending can be gained in contrast to XSW measurements.

6.4 Conclusion

The adsorption of the hetero-organic system of F₁₆CuPc on PTCDA/Ag(111) has been investigated by SPA-LEED. The result was, that F₁₆CuPc does not

penetrate into the 1st layer but forms a disordered film on top of the PTCDA layer for submonolayer coverages. A phase transition to a long range ordered structure occurs when the coverage is increased to ≈ 1 ML or upon cooling, which is similar to the behavior of F₁₆CuPc adsorbed on a bare Ag(111) surface. The order is described by a commensurate registry with the Ag substrate as well as with the PTCDA interlayer. This is a hint for a strong interaction between the two organic layers, similar to the findings published for the related system of CuPc on PTCDA/Ag(111) [10]. These results are in contrast to the common expectation of only weak physisorptive interactions between organic layers [113]. For F₁₆CuPc on CuPc/Ag(111), we also found an ordered F₁₆CuPc layer with a (possibly) commensurate relation to the lower adsorbate layer as discussed in chapter 5.2. However, in this case the interlayer (CuPc) did not exhibit a commensurate registry with the Ag substrate, but the CuPc molecules adopted different adsorption sites along the substrate lines (point-on-line). This also influences the structure formation and stability of the F₁₆CuPc layer on top. The commensurate PTCDA interlayer on the other hand represents a periodic landscape with respect to substrate mediated interactions, which probably also stabilizes the F₁₆CuPc structure by enabling a more site specific interaction. Nevertheless the layer distance between F₁₆CuPc and PTCDA, determined by SPA-LEED, turned out to be very similar to that between F₁₆CuPc and CuPc, which is a sign for a similar interaction strength. In both systems, the layer distance is clearly below the sum of van-der-Waals radii for carbon–carbon (3.4 Å), which is another indication for a strong interaction between F₁₆CuPc layer and interlayer. Pair potential calculations also yielded optimum stacking distances that are comparable to the corresponding experimental results. It can be concluded, that in both hetero-organic interfaces the interaction strength appears to be stronger than pure physisorption.

7 Summary

In this work, the metal–organic interfaces SnPc/Ag(111) and F₁₆CuPc/Ag(111) as well as the organic–organic interfaces F₁₆CuPc/CuPc and F₁₆CuPc/PTCDA on Ag(111) have been investigated. The main focus of the work was on the elucidation of lateral structures with SPA-LEED and their origin using pair potential calculations. Regarding the metal–organic interfaces, further details of the lateral structure formation and molecular orientations have been investigated by STM. For the stacked hetero-organic systems, the vertical interaction strength was characterized by measuring the adsorption heights with XSW and SPA-LEED.

STM measurements on SnPc/Ag(111) have been performed for different temperatures and adsorbate coverages. Based on earlier SPA-LEED results [8], which have revealed unit cell parameters in different adsorbate phases, we have now determined molecular orientations of the SnPc molecules in all regions of the structural phase diagram. Typically, we found an alignment of the diagonal axis through one wing pair of the molecules with one of the high symmetry ⟨1̄10⟩ substrate directions. The occurrence of two different adsorption geometries (Sn-up and Sn-down) in the g-phase and in the c-phase has been confirmed. Evidence for different adsorption sites of the Sn-up and Sn-down molecules was found in the different symmetry breaking of the molecules and in an observed movement of the Sn-up molecules by half of a substrate lattice vector upon switching to Sn-down. However, the exact adsorption sites could not be determined. The adsorbate structures in the different phases could be very nicely explained by comparing favored intermolecular distance vectors, obtained by pair potential calculations, with the unit cell vectors found experimentally. In the c-phase, the measured in-plane angles of the molecules lead to a coincidence of the intermolecular potential minima with commensurate adsorption sites, thus optimizing both the adsorbate–substrate and the adsorbate–adsorbate interactions. In the other phases, the substrate influence mainly manifests in an alignment of the molecular diagonals with high symmetry directions. This alignment is especially strong in the g-phase where the molecules are sterically less confined than in the other phases. Consequently, a symmetry breaking of the molecules is found, caused by the different registry of the two pairs of molecular wings and the charge transfer with the substrate.

The adsorption of F₁₆CuPc/Ag(111) was discussed in detail in chapter 4, where the structural phase diagram was investigated with SPA-LEED for different coverages and temperatures. It includes a dilute phase at submonolayer coverages with a decreasing intermolecular distance as the coverage increases. An ordered structure forms for 1 ML coverage at RT as well as for submonolay-

7 Summary

ers at LT. The latter indicates an increased intermolecular attraction changing the film structure to 2D-island formation. These findings are very similar to the related system CuPc/Ag(111), except for the missing p.o.l.-phase regime. However, the ordered structure was found to be considerably different from all ordered CuPc/Ag(111) structures. F₁₆CuPc films consist of highly ordered rows of molecules along the $\langle 11\bar{2} \rangle$ directions. In the perpendicular $\langle 1\bar{1}0 \rangle$ directions however, the degree of order is rather low, which is indicated by streaks in the LEED images. Neighboring rows were found to be shifted against each other along the direction of the rows and two different molecular orientations occurred. This structure could be described by two row domains and a glide mirror symmetry. Consequently, the unit cell is rather large, containing four molecules with different orientations and/or adsorption sites. The observed structure deviates from the generally favored arrangement of phthalocyanines, which is probably the result of a considerable electrostatic repulsion between the terminating fluorine atoms, inducing stress in a close packed adsorbate film. Pair potential calculations yielded strictly repulsive intermolecular interactions, which is not compatible with the observed island formation at LT. However, the discrepancy could be explained by assuming that the electrostatic potential is overestimated in the calculations. Intermolecular distance vectors within the molecular rows are then well described by local vdW potential minima.

In the second part of this work (chapters 5 and 6), layers containing two different molecules (i.e. hetero-organic films) were investigated.

Lateral mixing of F₁₆CuPc molecules with CuPc was found to result in considerable changes on the growth mode as well as the resulting structural order. Lateral attraction between the two molecular species dominates, leading to 2D-island growth at RT. Alternating sequences of the two species in chessboard-like superstructures are therefore favorable, which reduces the repulsion between neighboring F₁₆CuPc molecules compared to pure F₁₆CuPc films. As a consequence, laterally mixed films with intermediate stoichiometries between the two species were found to show considerable similarities with phases of pure CuPc films at LT. A commensurate sub-ML superstructure was found, which changes into a point-on-line registry due to sterical hindrances upon approaching a coverage of 1 ML. The molecular pattern in these mixed films was found to be the same as in pure CuPc films at LT with every 2nd molecule being replaced by F₁₆CuPc. Consequently, the structures of both the sub-ML as well as the ML mixed films represent c(2×2) superstructures of a corresponding CuPc/Ag(111) structure. Obviously the CuPc lattice parameters represent a generally favorable adsorption geometry for phthalocyanine molecules regarding interactions with the Ag(111) substrate. This can be explained by similar interaction channels for both species, e.g., via a site specific interaction of the nitrogen atoms with the substrate. For mixed films with a high fraction of CuPc, the formation of chessboard-like domains did not occur in some preparations. Instead, the F₁₆CuPc molecules were statistically distributed, producing no additional superstructure spots. In case of high F₁₆CuPc fractions on the other hand, very complicated LEED patterns were found, originating from two or more coexisting superstructures.

For the *vertically* mixed (=stacked) heterosystems $F_{16}CuPc$ on $CuPc/Ag(111)$ and $F_{16}CuPc$ on $PTCDA/Ag(111)$, we found commensurate relations between the adsorbate lattices of the different organic layers. This points to an unexpectedly strong, not purely physisorptive interaction between the organic layers, similar to the system $CuPc$ on $PTCDA/Ag(111)$ [10]. For both systems, the interaction strength could be quantified by determining the organic–organic layer distance from XSW and SPA-LEED, respectively. In both cases, similar average layer distances in the range of 3.0 Å to 3.1 Å were found, which were also reproduced quite well by pair potential calculations between vertically displaced molecules. These numbers are compatible with an overlap of wave functions between atoms in different layers. Consequently, charge transfer across the organic layers is possible.

In conclusion, different structures of phthalocyanine films (mixed with PTCDA in one case) could be formed, which differ depending on species, coverages and sample temperature. This diversity of structures is caused by comparable interaction strengths of the molecules with their neighbors on the one hand and the $Ag(111)$ substrate on the other hand, leading to rather delicate force balances. While many phthalocyanine species tend to form similar adsorbate lattices for similar external parameters, variations could be induced by choosing species with permanent vertical dipole moments ($SnPc$) or strongly negatively charged terminating atoms ($F_{16}CuPc$). Adsorbate–adsorbate interactions were found to be considerably strong, as they even dominate the structure formation in most systems investigated here. Our results allow us to explain the observed adsorbate structures by rather simple calculations based on a pair potential approach, although they do not include substrate interactions. Hence, these calculations provide a simple and helpful tool for explaining the observed structures and can even be used for predictions on related systems. In case of vertically stacked systems, we showed that interactions at organic–organic interfaces can be unexpectedly strong, which might have significant influences on the growth of higher layers as well as on the efficiency of charge transport in electronic devices based on organic thin films.

For all hetero-organic films investigated here, ultraviolet photoelectron spectroscopy (UPS) measurements would be helpful to learn details about the electronic structure of the systems. These measurements might directly show whether charge transfer occurs in the vertically stacked films. Such measurements are scheduled within a subsequent PhD project.

The lateral structure in both the laterally and the vertically mixed heterosystems is not perfectly clear yet. While the unit cells are known from SPA-LEED, orientations of the molecules could only be predicted from pair potential calculations in some cases. STM measurements would be necessary to verify and complement these results. Especially the $F_{16}CuPc$ -rich lateral mixed film structure could not be solved from SPA-LEED data alone.

Finally, the knowledge about the registry of the organic layers would be in-

7 Summary

teresting for the vertically mixed films in order to quantify the possible overlap of molecular wave functions between toplayer and interlayer atoms. Such measurements are challenging, but have been performed, e.g., for CuPc on PTCDA/Ag(111) [10].

List of Acronyms

BZ	Brillouin Zone
c-phase	commensurate phase
CuPc	Copper-phthalocyanine
DFT	Density Functional Theory
DOS	Density Of States
fcc	face centered cubic
F ₁₆ CuPc	(per-)fluorinated copper-phthalocyanine
FFT	Fast Fourier Transform
FWHM	Full Width at Half Maximum
g-phase	gas-like phase
HOMO	Highest Occupied Molecular Orbital
IC	Ion Current
LDOS	Local Density Of States
LEED	Low Energy Electron Diffraction
LUMO	Lowest Unoccupied Molecular Orbital
ML	Monolayer
OMBE	Organic Molecular Beam Epitaxy
p.o.l.(-phase)	point-on-line (phase)
PTCDA	3,4,9,10-perylene-tetracarboxylic-dianhydride
QMS	Quadrupole Mass Spectrometer
SnPc	Tin(II)-phthalocyanine
SPA-LEED	Spot Profile Analysis LEED
STM	Scanning Tunneling Microscopy
STS	Scanning Tunneling Spectroscopy
UPS	Ultraviolet Photoelectron Spectroscopy
vdW	van-der-Waals
XPS	X-ray Photoelectron Spectroscopy
XSW	X-ray Standing Waves

List of Figures

2.1	Ewald construction for LEED and SPA-LEED	6
2.2	Setup of a SPA-LEED instrument	7
2.3	SPA-LEED calibration factors	9
2.4	STM tunneling junction	10
2.5	Principle of XSW	13
2.6	vdW potentials for F and Sn	17
2.7	Schematic of a Ag(111) surface	18
3.1	SnPc/Ag(111): Structural phase diagram	22
3.2	SnPc/Ag(111): STM of 0.12 ML g-phase at 5 K	24
3.3	SnPc/Ag(111): Rotations induced by STM	25
3.4	SnPc/Ag(111): STM linescans across molecules	26
3.5	SnPc/Ag(111): Switching from Sn-up to Sn-down	27
3.6	SnPc/Ag(111): STM of 0.7 ML c-phase	29
3.7	SnPc/Ag(111): STM of 0.7 ML c-phase: closeup	30
3.8	SnPc/Ag(111): Molecular orientations in c-phase	31
3.9	SnPc/Ag(111): STM of 0.9 ML p.o.l.-phase	33
3.10	SnPc/Ag(111): STM of 0.9 ML c-phase	34
3.11	SnPc/Ag(111): STM of 0.95 ML p.o.l.-phase	35
3.12	SnPc/Ag(111): STS on g-phase	36
3.13	SnPc/Ag(111): STS on p.o.l.-phase	37
3.14	SnPc/Ag(111): Relation between STM contrast and LUMO distribution	39
3.15	Pair potential map: Sn-up and Sn-down	40
3.16	Pair potential map: SnPc g-phase	42
3.17	Pair potential grid calculation for SnPc c-phase	43
3.18	Pair potential map: SnPc c-phase	44
3.19	Pair potential map: SnPc p.o.l.-phase	45
4.1	Geometrical structure and orbitals of $F_{16}CuPc$ from DFT	50
4.2	$F_{16}CuPc/Ag(111)$: Structural phase diagram	51
4.3	$F_{16}CuPc/Ag(111)$: Deposition at LT	52
4.4	$F_{16}CuPc/Ag(111)$: Deposition sequence	53
4.5	$F_{16}CuPc/Ag(111)$: Evolution of intermolecular distances in g-phase	54
4.6	$F_{16}CuPc/Ag(111)$: Superstructure spot shape	56
4.7	$F_{16}CuPc/Ag(111)$: Effect of annealing	57
4.8	$F_{16}CuPc/Ag(111)$: TPD spectrum	58
4.9	$F_{16}CuPc/Ag(111)$: LEED model	59
4.10	$F_{16}CuPc/Ag(111)$: STM of submonolayer	60

List of Figures

4.11	$F_{16}CuPc/Ag(111)$: STM of 1 ML	61
4.12	$F_{16}CuPc/Ag(111)$: SPA-LEED and STM-FFT linescans	62
4.13	$F_{16}CuPc/Ag(111)$: STM of 1 ML: closeup	63
4.14	$F_{16}CuPc/Ag(111)$: Nomenclature for structure factor calculations	64
4.15	$F_{16}CuPc/Ag(111)$: Real space model	66
4.16	Pair potential map: $F_{16}CuPc$	67
4.17	Pair potential maps: Separate electrostatic and vdW components	69
4.18	$F_{16}CuPc/Ag(111)$: STM of 2nd layer	72
4.19	Pair potential map: $F_{16}CuPc$ in 2nd layer	73
4.20	$F_{16}CuPc$ on $Au(111)$ and on $Cu(111)$	74
4.21	SPA-LEED image of 1 ML $F_{16}CuPc/Cu(111)$	75
5.1	Pair potential maps: CuPc and $F_{16}CuPc$	78
5.2	$CuPc+F_{16}CuPc/Ag(111)$: Structural phase diagram	80
5.3	$CuPc+F_{16}CuPc/Ag(111)$: Deposition sequence	81
5.4	$CuPc+F_{16}CuPc/Ag(111)$: LEED model for sub-ML 1-to1-phase	82
5.5	Pair potential grid calculation for the $CuPc+F_{16}CuPc$ submonolayer 1-to1-phase	84
5.6	Pair potential map: $CuPc+F_{16}CuPc$ submonolayer 1-to1-phase	85
5.7	$CuPc+F_{16}CuPc/Ag(111)$: Real space model for sub-ML 1-to1-phase	86
5.8	$CuPc+F_{16}CuPc/Ag(111)$: 1-to1-phase spot shapes	88
5.9	$CuPc+F_{16}CuPc/Ag(111)$: LEED model for ML 1-to1-phase	89
5.10	$CuPc+F_{16}CuPc/Ag(111)$: LEED models for CuPc-rich films	91
5.11	$CuPc+F_{16}CuPc/Ag(111)$: Details of the $F_{16}CuPc$ -rich region	92
5.12	$CuPc+F_{16}CuPc/Ag(111)$: LEED models for $F_{16}CuPc$ -rich films	93
5.13	$F_{16}CuPc$ on $CuPc/Ag(111)$: Structural phase diagram	96
5.14	$F_{16}CuPc$ on $CuPc/Ag(111)$: LEED model	98
5.15	$CuPc/Ag(111)$: XPS fit models	100
5.16	$CuPc/Ag(111)$: XSW results	102
5.17	$CuPc/Ag(111)$: XSW results N1s single components	104
5.18	$F_{16}CuPc$ on $CuPc/Ag(111)$: XPS fit models	106
5.19	$F_{16}CuPc$ on $CuPc/Ag(111)$: XSW results	108
5.20	$F_{16}CuPc$ on $CuPc/Ag(111)$: Argand diagram	109
5.21	$F_{16}CuPc$ on $CuPc/Ag(111)$: XSW results C1s single components	110
5.22	$F_{16}CuPc$ on $CuPc/Ag(111)$: XSW vector constructions	111
5.23	$F_{16}CuPc$ on $CuPc/Ag(111)$: Vertical adsorption geometry	112
5.24	Pair potential map: $F_{16}CuPc$ on CuPc	113
6.1	TPD spectrum of PTCDA/ $Ag(111)$	116
6.2	$F_{16}CuPc$ on PTCDA/ $Ag(111)$: Deposition sequence	117
6.3	$F_{16}CuPc$ on PTCDA/ $Ag(111)$: Structural phase diagram	118
6.4	$F_{16}CuPc$ on PTCDA/ $Ag(111)$: LEED model	119
6.5	$F_{16}CuPc$ on PTCDA/ $Ag(111)$: Real space model	120
6.6	$F_{16}CuPc$ on PTCDA/ $Ag(111)$: Annealing effect	122
6.7	Pair potential maps: $F_{16}CuPc$ and PTCDA	123
6.8	$F_{16}CuPc$ on PTCDA/ $Ag(111)$: Layer distance from SPA-LEED .	124

Bibliography

- [1] M. Gross, D. C. Muller, H.-G. Nothofer, U. Scherf, D. Neher, C. Brauchle, and K. Meerholz. Improving the performance of doped π -conjugated polymers for use in organic light-emitting diodes. *Nature*, 405:661–665, 2000.
- [2] A. Facchetti. Semiconductors for organic transistors. *Materials Today*, 10(3):28–37, 2007.
- [3] F. Yang, M. Shtein, and S. R. Forrest. Controlled growth of a molecular bulk heterojunction photovoltaic cell. *Nature Materials*, 4(1):37–41, 2005.
- [4] S. Uchida, J. Xue, B. P. Rand, and S. R. Forrest. Organic small molecule solar cells with a homogeneously mixed copper phthalocyanine: C_60 active layer. *Appl. Phys. Lett.*, 84(21):4218–4220, 2004.
- [5] P. Peumans, S. Uchida, and S. R. Forrest. Efficient bulk heterojunction photovoltaic cells using small-molecular-weight organic thin films. *Nature*, 425(6954):158–162, 2003.
- [6] J. V. Barth, G. Costantini, and K. Kern. Engineering atomic and molecular nanostructures at surfaces. *Nature*, 437(7059):671–679, 2005.
- [7] F. S. Tautz. Structure and bonding of large aromatic molecules on noble metal surfaces: The example of PTCDA. *Prog. Surf. Sci.*, 82(9-12):479–520, 2007.
- [8] C. Stadler, S. Hansen, I. Kroeger, C. Kumpf, and E. Umbach. Tuning intermolecular interaction in long-range-ordered submonolayer organic films. *Nature Physics*, 5(2):153–158, 2009.
- [9] C. Stadler. *Strukturuntersuchungen organischer Monolagen auf Ag(111)*. PhD thesis, University of Würzburg, 2009.
- [10] B. Stadtmüller, T. Sueyoshi, G. Kichin, I. Kroeger, S. Soubatch, R. Temirov, F. S. Tautz, and C. Kumpf. Commensurate Registry and Chemisorption at a Hetero-organic Interface. *Phys. Rev. Lett.*, 108(10):106103, 2012.
- [11] C. Davisson and L. H. Germer. Diffraction of Electrons by a Crystal of Nickel. *Phys. Rev.*, 30(6):705–740, 1927.
- [12] I. K. Robinson. Crystal truncation rods and surface roughness. *Phys. Rev. B*, 33(6):3830–3836, 1986.
- [13] M. Horn-von Hoegen. Growth of semiconductor layers studied by spot profile analysing low energy electron diffraction - Part I. *Zeitschrift Für Kristallographie*, 214(10):591–629, 1999.

Bibliography

- [14] U. Scheithauer, G. Meyer, and M. Henzler. A new LEED instrument for quantitative spot profile analysis. *Surface Science*, 178:441–451, 1986.
- [15] P. Bayersdorfer. *SPA-LEED-Studie zur Adsorption von metallfreien Phthalocyaninen auf Ag(111) im Bereich kleiner Bedeckungen*, Diplomarbeit, University of Würzburg, 2008.
- [16] G. Binnig, H. Rohrer, C. Gerber, and E. Weibel. Tunneling through a controllable vacuum gap. *Appl. Phys. Lett.*, 40:178–180, 1982.
- [17] C. J. Chen. *Introduction to scanning tunneling microscopy*. Oxford University Press, 2008.
- [18] J. Tersoff and D. R. Hamann. Theory of the scanning tunneling microscope. *Phys. Rev. B*, 31(2):805–813, 1985.
- [19] J. Bardeen. Tunnelling from a Many-Particle Point of View. *Phys. Rev. Lett.*, 6(2):57–59, 1961.
- [20] I. Tamm. Über eine mögliche Art der Elektronenbindung an Kristalloberflächen. *Zeitschrift für Physik A Hadrons and Nuclei*, 76(11-12):849–850, 1932.
- [21] W. Shockley. On the Surface States Associated with a Periodic Potential. *Phys. Rev.*, 56(4):317–323, 1939.
- [22] C. Weiss, C. Wagner, C. Kleimann, M. Rohlfing, F. S. Tautz, and R. Temirov. Imaging Pauli Repulsion in Scanning Tunneling Microscopy. *Phys. Rev. Lett.*, 105(8):086103, 2010.
- [23] C. Weiss, C. Wagner, R. Temirov, and F. S. Tautz. Direct Imaging of Intermolecular Bonds in Scanning Tunneling Microscopy. *J. Am. Chem. Soc.*, 132(34):11864–11865, 2010.
- [24] G. Kichin, C. Weiss, C. Wagner, F. S. Tautz, and R. Temirov. Single Molecule and Single Atom Sensors for Atomic Resolution Imaging of Chemically Complex Surfaces. *J. Am. Chem. Soc.*, 133(42):16847–16851, 2011.
- [25] R. Temirov, S. Soubatch, O. Neucheva, A. C. Lassise, and F. S. Tautz. A novel method achieving ultra-high geometrical resolution in scanning tunnelling microscopy. *New J. Phys.*, 10:053012, 2008.
- [26] I. Horcas, R. Fernandez, J. M. Gomez-Rodriguez, J. Colchero, J. Gomez-Herrero, and A. M. Baro. WSXM: A software for scanning probe microscopy and a tool for nanotechnology. *Rev. Sci. Instr.*, 78(1):013705, 2007.
- [27] D. Necas and P. Klapetek. Gwyddion: an open-source software for SPM data analysis. *Centr. Europ. J. Phys.*, 10(1):181–188, 2012.
- [28] P. L. Cowan, J. A. Golovchenko, and M. F. Robbins. X-Ray Standing Waves at Crystal Surfaces. *Phys. Rev. Lett.*, 44(25):1680–1683, 1980.
- [29] D. P. Woodruff. Surface structure determination using x-ray standing waves. *Rep. Prog. Phys.*, 68:743–798, 2005.

Bibliography

- [30] A. Hauschild, K. Karki, B. C. C. Cowie, M. Rohlfing, F. S. Tautz, and M. Sokolowski. Molecular distortions and chemical bonding of a large π -conjugated molecule on a metal surface. *Phys. Rev. Lett.*, 94(3):036106, 2005.
- [31] I. A. Vartanyants and J. Zegenhagen. Photoelectric scattering from an X-ray interference field. *Solid State Comm.*, 113(6):299–320, 1999.
- [32] I. Kroeger, B. Stadtmueller, C. Wagner, C. Weiss, R. Temirov, F. S. Tautz, and C. Kumpf. Modeling intermolecular interactions of physisorbed organic molecules using pair potential calculations. *J. Chem. Phys.*, 135:234703, 2011.
- [33] I. Kroeger. *Adsorption von Phthalocyaninen auf Edelmetalloberflächen*. PhD thesis, University of Würzburg, 2011.
- [34] J. P. Foster and F. Weinhold. Natural hybrid orbitals. *J. Am. Chem. Soc.*, 102(24):7211–7218, 1980.
- [35] M. J. Frisch, G. W. Trucks, H. B. Schlegel, G. E. Scuseria, M. A. Robb, J. R. Cheeseman, J. A. Montgomery, T. Vreven, K. N. Kudin, J. C. Burant, J. M. Millam, S. S. Iyengar, J. Tomasi, V. Barone, B. Mennucci, M. Cossi, G. Scalmani, N. Rega, G. A. Petersson, H. Nakatsuji, M. Hada, M. Ehara, K. Toyota, R. Fukuda, J. Hasegawa, M. Ishida, T. Nakajima, Y. Honda, O. Kitao, H. Nakai, M. Klene, X. Li, J. E. Knox, H. P. Hratchian, J. B. Cross, V. Bakken, C. Adamo, J. Jaramillo, R. Gomperts, R. E. Stratmann, O. Yazyev, A. J. Austin, R. Cammi, C. Pomelli, J. W. Ochterski, P. Y. Ayala, K. Morokuma, G. A. Voth, P. Salvador, J. J. Dannenberg, V. G. Zakrzewski, S. Dapprich, A. D. Daniels, M. C. Strain, O. Farkas, D. K. Malick, A. D. Rabuck, K. Raghavachari, J. B. Foresman, J. V. Ortiz, Q. Cui, A. G. Baboul, S. Clifford, J. Cioslowski, B. B. Stefanov, G. Liu, A. Liashenko, P. Piskorz, I. Komaromi, R. L. Martin, D. J. Fox, T. Keith, M. A. Al-Laham, C. Y. Peng, A. Nanayakkara, M. Challacombe, P. M. W. Gill, B. Johnson, W. Chen, M. W. Wong, C. Gonzalez, and J. A. Pople. Gaussian 03, Revision C.02, 2003.
- [36] M. Rohlfing, R. Temirov, and F. S. Tautz. Adsorption structure and scanning tunneling data of a prototype organic-inorganic interface: PTCDA on Ag(111). *Phys. Rev. B*, 76(11):115421, 2007.
- [37] J. Shanker, P. S. Bakhshi, and L. P. Sharma. Analysis of the crystal binding and the Anderson-Gruneisen parameters in the halides of copper(I), silver(I) and thallium(I). *J. Inorg. Nucl. Chem.*, 41(9):1285–1288, 1979.
- [38] R. A. Scott and H. A. Scheraga. Method for Calculating Internal Rotation Barriers. *J. Chem. Phys.*, 42(6):2209–2215, 1965.
- [39] S. R. Forrest and Y. Zhang. Ultrahigh-vacuum quasiepitaxial growth of model van der Waals thin films. I. Theory. *Phys. Rev. B*, 49(16):11297–11308, 1994.
- [40] W. M. Haynes. *CRC Handbook of Chemistry and Physics*, volume 92. CRC Press, 2011-2012.

Bibliography

- [41] A. Bondi. van der Waals Volumes and Radii. *J. Phys. Chem.*, 68(3):441–451, 1964.
- [42] C. Stadler, S. Hansen, F. Pollinger, C. Kumpf, E. Umbach, T.-L. Lee, and J. Zegenhagen. Structural investigation of the adsorption of SnPc on Ag(111) using normal-incidence x-ray standing waves. *Phys. Rev. B*, 74(3):035404, 2006.
- [43] S. C. B. Mannsfeld and T. Fritz. Understanding organic-inorganic heteroepitaxial growth of molecules on crystalline substrates: Experiment and theory. *Phys. Rev. B*, 71:235405, 2005.
- [44] M. Lackinger and M. Hietschold. Determining adsorption geometry of individual tin-phthalocyanine molecules on Ag(111) - a STM study at submonolayer coverage. *Surface Science*, 520(1-2):L619–L624, 2002.
- [45] I. Kroeger, B. Stadtmueller, C. Stadler, J. Ziroff, M. Kochler, A. Stahl, F. Pollinger, T.-L. Lee, J. Zegenhagen, F. Reinert, and C. Kumpf. Submonolayer growth of copper-phthalocyanine on Ag(111). *New J. Phys.*, 12:083038, 2010.
- [46] B. Stadtmueller, I. Kroeger, F. Reinert, and C. Kumpf. Submonolayer growth of CuPc on noble metal surfaces. *Phys. Rev. B*, 83(8):085416, 2011.
- [47] G. Held, W. Braun, H.-P. Steinrueck, S. Yamagishi, S. J. Jenkins, and D. A. King. Light-Atom Location in Adsorbed Benzene by Experiment and Theory. *Phys. Rev. Lett.*, 87(21):216102, 2001.
- [48] G. Xu, X.-Q. Shi, R. Q. Zhang, W. W. Pai, H. T. Jeng, and M. A. Van Hove. Detailed low-energy electron diffraction analysis of the (4x4) surface structure of C₆₀ on Cu(111): Seven-atom-vacancy reconstruction. *Phys. Rev. B*, 86(7):075419, 2012.
- [49] H. Lüth. *Solid surfaces, interfaces and thin films*. Graduate texts in physics. Springer, Heidelberg, 5. edition, 2010.
- [50] H. Karacuban, M. Lange, J. Schaffert, O. Weingart, T. Wagner, and R. Moeller. Substrate-induced symmetry reduction of CuPc on Cu(111): An LT-STM study. *Surface Science*, 603(5):L39–L43, 2009.
- [51] Y. Wang, J. Kroeger, R. Berndt, and W. Hofer. Structural and Electronic Properties of Ultrathin Tin-Phthalocyanine Films on Ag(111) at the Single-Molecule Level. *Angewandte Chemie-international Edition*, 48(7):1261–1265, 2009.
- [52] J. D. Baran, J. A. Larsson, R. A. J. Woolley, Y. Cong, P. J. Moriarty, A. A. Cafolla, K. Schulte, and V. R. Dhanak. Theoretical and experimental comparison of SnPc, PbPc, and CoPc adsorption on Ag(111). *Phys. Rev. B*, 81(7):075413, 2010.
- [53] Y. Wang, J. Kroeger, R. Berndt, and W. A. Hofer. Pushing and Pulling a Sn Ion through an Adsorbed Phthalocyanine Molecule. *J. Am. Chem. Soc.*, 131(10):3639–3643, 2009.

Bibliography

- [54] Y. L. Huang, Y. Lu, T. C. Niu, H. Huang, S. Kera, N. Ueno, A. T. S. Wee, and W. Chen. Reversible Single-Molecule Switching in an Ordered Monolayer Molecular Dipole Array. *Small*, 8(9):1423–1428, 2012.
- [55] J. D. Baran and J. A. Larsson. Inversion of the shuttlecock shaped metal phthalocyanines MPc (M = Ge, Sn, Pb)-a density functional study. *Phys. Chem. Chem. Phys.*, 12(23):6179–6186, 2010.
- [56] S. Soubatch, I. Kroeger, C. Kumpf, and F. S. Tautz. Structure and growth of tetracene on Ag(111). *Phys. Rev. B*, 84(19):195440, 2011.
- [57] M. Haeming, C. Scheuermann, A. Schoell, F. Reinert, and E. Umbach. Coverage dependent organic-metal interaction studied by high-resolution core level spectroscopy: SnPc (sub)monolayers on Ag(111). *J. El. Spec. Rel. Phen.*, 174(1-3):59–64, 2009.
- [58] M. Toader and M. Hietschold. Tuning the Energy Level Alignment at the SnPc/Ag(111) Interface Using an STM Tip. *J. Phys. Chem. C*, 115(7):3099–3105, 2011.
- [59] H. Huang, W. Chen, and A. T. S. Wee. Low-temperature scanning tunneling microscopy investigation of epitaxial growth of F₁₆CuPc thin films on Ag(111). *J. Phys. Chem. C*, 112(38):14913–14918, 2008.
- [60] H. Huang, S. L. Wong, W. Chen, and A. T. S. Wee. LT-STM studies on substrate-dependent self-assembly of small organic molecules. *J. Phys. D: Appl. Phys.*, 44(46):464005, 2011.
- [61] A. Gerlach, F. Schreiber, S. Sellner, H. Dosch, I. A. Vartanyants, B. C. C. Cowie, T. L. Lee, and J. Zegenhagen. Adsorption-induced distortion of F₁₆CuPc on Cu(111) and Ag(111): An x-ray standing wave study. *Phys. Rev. B*, 71(20):205425, 2005.
- [62] I. Kroeger, B. Stadtmueller, C. Kleimann, P. Rajput, and C. Kumpf. Normal-incidence x-ray standing-wave study of copper phthalocyanine submonolayers on Cu(111) and Au(111). *Phys. Rev. B*, 83(19):195414, 2011.
- [63] E. F. Lazneva. Laser desorption from the surface of copper phthalocyanine films on silicon and cadmium sulfide. *Tech. Phys. Lett.*, 33(11):926–929, 2007.
- [64] I. Kroeger, P. Bayersdorfer, B. Stadtmueller, C. Kleimann, G. Mercurio, F. Reinert, and C. Kumpf. Submonolayer growth of H₂-phthalocyanine on Ag(111). *Phys. Rev. B*, 86(19):195412, 2012.
- [65] L. Kilian, E. Umbach, and M. Sokolowski. Molecular beam epitaxy of organic films investigated by high resolution low energy electron diffraction (SPA-LEED): 3,4,9,10-perylenetetracarboxylic acid-dianhydride (PTCDA) on Ag(111). *Surface Science*, 573(3):359–378, 2004.
- [66] J. H. Neave, B. A. Joyce, P. J. Dobson, and N. Norton. Dynamics of film growth of GaAs by MBE from RHEED observations. *Appl. Phys. A*, 31(1):1–8, 1983.

Bibliography

- [67] M. Henzler. LEED studies of surface imperfections. *Applications of Surface Science*, 11–12:450–469, 1982.
- [68] S. C. Bobaru, E. Salomon, J.-M. Layet, and T. Angot. Structural Properties of Iron Phtalocyanines on Ag(111): From the Submonolayer to Monolayer Range. *J. Phys. Chem. C*, 115(13):5875–5879, 2011.
- [69] M. Koudia, M. Abel, C. Maurel, A. Bliek, D. Catalin, M. Mossyan, J. C. Mossyan, and L. Porte. Influence of chlorine substitution on the self-assembly of zinc phthalocyanine. *J. Phys. Chem. B*, 110(20):10058–10062, 2006.
- [70] X. Lu and K. W. Hipps. Scanning Tunneling Microscopy of Metal Phthalocyanines: d6 and d8 Cases. *J. Phys. Chem. B*, 101(27):5391–5396, 1997.
- [71] D. G. de Oteyza, A. El-Sayed, J. M. Garcia-Lastra, E. Goiri, T. N. Krauss, A. Turak, E. Barrena, H. Dosch, J. Zegenhagen, A. Rubio, Y. Wakayama, and J. E. Ortega. Copper-phthalocyanine based metal–organic interfaces: The effect of fluorination, the substrate, and its symmetry. *J. Chem. Phys.*, 133(21):214703–6, 2010.
- [72] P. Avouris, R. Kawai, N. D. Lang, and D. M. Newns. On the mechanism of desorption from surfaces induced by electronic transitions. *J. Chem. Phys.*, 89(4):2388–2396, 1988.
- [73] K. Katoh, T. Komeda, and M. Yamashita. Surface morphologies, electronic structures, and Kondo effect of lanthanide(iii)-phthalocyanine molecules on Au(111) by using STM, STS and FET properties for next generation devices. *Dalton Trans.*, 39(20):4708–4723, 2010.
- [74] L. Smykalla, P. Shukrynau, and M. Hietschold. Investigation of Ultrathin Layers of Bis(phthalocyaninato)lutetium(III) on Graphite. *J. Phys. Chem. C*, 116(14):8008–8013, 2012.
- [75] Y. Wakayama. Assembly Process and Epitaxy of the F₁₆CuPc Monolayer on Cu(111). *J. Phys. Chem. C*, 111(6):2675–2678, 2007.
- [76] L. Chen, H. Li, and A. T. S. Wee. Nonlocal Chemical Reactivity at Organic-Metal Interfaces. *ACS Nano*, 3(11):3684–3690, 2009.
- [77] B. E. Murphy, S. A. Krasnikov, A. A. Cafolla, N. N. Sergeeva, N. A. Vinogradov, J. P. Beggan, O. Lübben, M. O. Senge, and I. V. Shvets. Growth and ordering of Ni(II) diphenylporphyrin monolayers on Ag(111) and Ag/Si(111) studied by STM and LEED. *J. Phys.: Condens. Matt.*, 24(4):045005, 2012.
- [78] S. M. Suturin, N. S. Sokolov, J. Roy, and J. Zegenhagen. STM and LEED studies of CaF₂ submonolayer coverage on Si(001). *Surface Science*, 605:153–157, 2011.
- [79] J. Wang, H. Wang, X. Yan, H. Huang, and D. Yan. Organic heterojunction and its application for double channel field-effect transistors. *Appl. Phys. Lett.*, 87(9):093507–3, 2005.

Bibliography

- [80] S. Barth, P. Muller, H. Riel, P. F. Seidler, W. Riess, H. Vestweber, and H. Bassler. Electron mobility in tris(8-hydroxy-quinoline)aluminum thin films determined via transient electroluminescence from single- and multi-layer organic light-emitting diodes. *J. Appl. Phys.*, 89(7):3711–3719, 2001.
- [81] H. Huang, W. Chen, S. Chen, D. C. Qi, X. Y. Gao, and A. T. S. Wee. Molecular orientation of CuPc thin films on C₆₀/Ag(111). *Appl. Phys. Lett.*, 94(16):163304, 2009.
- [82] F. Babudri, G. M. Farinola, F. Naso, and R. Ragni. Fluorinated organic materials for electronic and optoelectronic applications: the role of the fluorine atom. *Chem. Commun.*, (10):1003–1022, 2007.
- [83] H. Brinkmann, C. Kelting, S. Makarov, O. Tsaryova, G. Schnurpfeil, D. Woehrle, and D. Schlettwein. Fluorinated phthalocyanines as molecular semiconductor thin films. *phys. stat. sol. (a)*, 205(3):409–420, 2008.
- [84] V. Oison, M. Koudia, M. Abel, and L. Porte. Influence of stress on hydrogen-bond formation in a halogenated phthalocyanine network. *Phys. Rev. B*, 75(3):035428–, 2007.
- [85] A. Kraft, R. Temirov, S. K. M. Henze, S. Soubatch, M. Rohlfing, and F. S. Tautz. Lateral adsorption geometry and site-specific electronic structure of a large organic chemisorbate on a metal surface. *Phys. Rev. B*, 74(4):041402, 2006.
- [86] R. Feidenhans'l. Surface structure determination by X-ray diffraction. *Surf. Sci. Rep.*, 10(3):105–188, 1989.
- [87] H. L. Meyerheim, Th. Gloege, M. Sokolowski, E. Umbach, and P. Baeuerle. Adsorption-induced distortion of a large π -conjugated molecule studied by surface X-ray diffraction: End-capped quaterthiophene on Ag(111). *EPL (Europhysics Letters)*, 52(2):144–150, 2000.
- [88] L. Kilian, U. Stahl, I. Kossev, M. Sokolowski, R. Fink, and E. Umbach. The commensurate-to-incommensurate phase transition of an organic monolayer: A high resolution LEED analysis of the superstructures of NTCDA on Ag(111). *Surface Science*, 602(14):2427–2434, 2008.
- [89] Y. L. Huang, H. Li, J. Ma, H. Huang, W. Chen, and A. T. S. Wee. Scanning Tunneling Microscopy Investigation of Self-Assembled CuPc/F₁₆CuPc Binary Superstructures on Graphite. *Langmuir*, 26(5):3329–3334, 2009.
- [90] A. Calzolari, W. Jin, J. E. Reutt-Robey, and M. B. Nardelli. Substrate-Mediated Intermolecular Hybridization in Binary Phthalocyanine Superstructures. *J. Phys. Chem. C*, 114(2):1041–1045, 2010.
- [91] E. Barrena, D. G. de Oteyza, H. Dosch, and Y. Wakayama. 2D Supramolecular Self-Assembly of Binary Organic Monolayers. *ChemPhysChem*, 8(13):1915–1918, 2007.
- [92] M. C. Cottin, J. Schaffert, A. Sonntag, H. Karacuban, R. Moeller, and C. A. Bobisch. Supramolecular architecture of organic molecules: PTCDA

Bibliography

- and CuPc on a Cu(111) substrate. *Appl. Surf. Sci.*, 258(6):2196–2200, 2012.
- [93] C. Bobisch, T. Wagner, A. Bannani, and R. Moller. Ordered binary monolayer composed of two organic molecules: Copper-phthalocyanine and 3,4,9,10-perylene-tetra-carboxylic-dianhydride on Cu(111). *J. Chem. Phys.*, 119(18):9804–9808, 2003.
- [94] H. Huang, Y. Huang, J. Pflaum, A. T. S. Wee, and W. Chen. Nanoscale phase separation of a binary molecular system of copper phthalocyanine and di-indenoperylene on Ag(111). *Appl. Phys. Lett.*, 95(26):263309–3, 2009.
- [95] N. Fairley. CasaXPS: Processing Software for XPS, AES, SIMS and more, version 2.3.16.
- [96] M. Schmid, A. Kaftan, and J. M. Steinrueck, H.-P. and Gottfried. The electronic structure of cobalt(II) phthalocyanine adsorbed on Ag(111). *Surface Science*, 606:945–949, 2012.
- [97] D. A. Shirley. High-Resolution X-Ray Photoemission Spectrum of the Valence Bands of Gold. *Phys. Rev. B*, 5(12):4709–4714, 1972.
- [98] T. D. Thomas, E. Kukk, R. Sankari, H. Fukuzawa, G. Prumper, K. Ueda, R. Puttner, J. Harries, Y. Tamenori, T. Tanaka, M. Hoshino, and H. Tanaka. Recoil excitation of vibrational structure in the carbon 1s photoelectron spectrum of CF₄. *J. Chem. Phys.*, 128(14):144311–10, 2008.
- [99] G. Mercurio. *Study of Molecule-Metal Interfaces by Means of the Normal Incidence X-ray Standing Wave Technique*. PhD thesis, RWTH Aachen University, 2012.
- [100] M. P. Seah and W. A. Dench. Quantitative electron spectroscopy of surfaces: A standard data base for electron inelastic mean free paths in solids. *Surf. Interface Anal.*, 1(1):2–11, 1979.
- [101] S. M. Yoon, H. J. Song, I. Hwang, K. S. Kim, and H. C. Choi. Single crystal structure of copper hexadecafluorophthalocyanine (F₁₆CuPc) ribbon. *Chem. Commun.*, 46(2):231–233, 2010.
- [102] T. Gruber, F. Forster, A. Schoell, and F. Reinert. Experimental determination of the attenuation length of electrons in organic molecular solids: The example of PTCDA. *Surface Science*, 605(9–10):878–882, 2011.
- [103] L. Romaner, G. Heimel, J.-L. Brédas, A. Gerlach, F. Schreiber, R. L. Johnson, J. Zegenhagen, S. Duhm, N. Koch, and E. Zojer. Impact of Bidirectional Charge Transfer and Molecular Distortions on the Electronic Structure of a Metal-Organic Interface. *Phys. Rev. Lett.*, 99(25):256801, 2007.
- [104] <http://www.webelements.com>.
- [105] C. Stadler, S. Hansen, A. Schoell, T.-L. Lee, J. Zegenhagen, C. Kumpf, and E. Umbach. Molecular distortion of NTCDA upon adsorption on Ag(111): a normal incidence x-ray standing wave study. *New J. Phys.*,

Bibliography

- 9(3):50, 2007.
- [106] A. Bendounan, F. Forster, A. Schoell, D. Batchelor, J. Ziroff, E. Umbach, and F. Reinert. Electronic structure of 1 ML NTCDA/Ag(111) studied by photoemission spectroscopy. *Surface Science*, 601(18):4013–4017, 2007.
 - [107] Y. Zou, L. Kilian, A. Scholl, T. Schmidt, R. Fink, and E. Umbach. Chemical bonding of PTCDA on Ag surfaces and the formation of interface states. *Surface Science*, 600(6):1240–1251, 2006.
 - [108] B. Stadtmueller. *Study of intermolecular interactions in hetero-organic thin films*. PhD thesis, RWTH Aachen University, 2013.
 - [109] Z. Iqbal, D. M. Ivory, and H. Eckhardt. Synthesis, Crystal Structure and Spectroscopy of 3,4-Perylene-dicarboxylic Monoanhydride. *Mol. Cryst. Liq. Cryst.*, 158(2):337–352, 1988.
 - [110] A. Schoell, private communications.
 - [111] C. Klein, T. Nabbelefeld, H. Hattab, D. Meyer, G. Jnawali, M. Kammler, F.-J. Meyer zu Heringdorf, A. Golla-Franz, B. H. Mueller, T. Schmidt, M. Henzler, and M. Horn-von Hoegen. Lost in reciprocal space? Determination of the scattering condition in spot profile analysis low-energy electron diffraction. *Rev. Sci. Instr.*, 82(3):035111, 2011.
 - [112] G. Mercurio, E. R. McNellis, I. Martin, S. Hagen, F. Leyssner, S. Soubatch, J. Meyer, M. Wolf, P. Tegeder, F. S. Tautz, and K. Reuter. Structure and Energetics of Azobenzene on Ag(111): Benchmarking Semiempirical Dispersion Correction Approaches. *Phys. Rev. Lett.*, 104(3):036102, 2010.
 - [113] S. Braun, W. R. Salaneck, and M. Fahlman. Energy-Level Alignment at Organic/Metal and Organic/Organic Interfaces. *Adv. Mater.*, 21(14–15):1450–1472, 2009.

Statutory declaration

I hereby truthfully and solemnly declare that I have carried out the work at hand entirely by myself and without the help of any third party, and that all sources of consulted material have been acknowledged.

Jülich, August 12, 2013

Christoph Kleimann

Acknowledgements

The past years in Jülich have been a great experience for me. This PhD thesis would not have been possible without the help of many other people. My thanks go to everybody who supported me during this time, especially

- Prof. Dr. Christian Kumpf for being a good mentor and supervisor and for always taking time for his students' problems
- Prof. Dr. Moritz Sokolowski for providing the second opinion on my thesis
- Prof. Dr. Stefan Tautz for giving me the chance to work in his institute
- Benjamin Stadtmüller for his help in all scientific concerns and for providing his pair potential calculation program
- Ingo Kröger for helping me with my first steps to UHV physics and to SPA-LEED
- Dr. Ruslan Temirov, Christian Weiss and Christa Elsaesser for the help with the STM measurements
- my successor Sonja Schröder for always being very entertaining. Take good care of the SPA-LEED!
- the rest of PGI-3 for the nice atmosphere in the institute
- the staff of the beamline ID32 of the ESRF for their support during our beamtime
- my friends and team-mates in the EBC Jülich and the Badminton group of the BSG
- my family for supporting me in all aspects of life
- everybody I forgot to mention here

Curriculum Vitae

Christoph Kleimann

Born on November 1st, 1980 in Herford, Germany
Nationality: German

Education

- 1991 - 2000: Abitur at Städtisches Gymnasium im Schulzentrum Aspe,
Bad Salzuflen, Germany
- 2001 - 2008: Study of physics at Bielefeld University, Germany
Workgroup: "Exp. Biophysics and Applied Nanoscience"
- 2008: Diplom degree in physics
Thesis title: "Weiterentwicklungen an der Optischen Pinzette"
Advisor: Prof. Dr. Dario Anselmetti
- 2009 - 2013: PhD student at Forschungszentrum Jülich, Germany
Institute: "PGI-3: Functional Nanostructures at Surfaces"
Advisor: Prof. Dr. Christian Kumpf
- 2013: Dr. rer. nat. degree in physics at RWTH Aachen University
Thesis title: "Adsorption of (hetero-)organic Phthalocyanine
and PTCDA thin films on Ag(111)"

Professional experience

- 2008 - 2009: Research Associate at Bielefeld University, Germany
Workgroup: "Exp. Biophysics and Applied Nanoscience"

Military service

- 2000 - 2001: German Federal Armed Forces, basic military service

Jülich, August 12, 2013

Schriften des Forschungszentrums Jülich
Reihe Schlüsseltechnologien / Key Technologies

Band / Volume 54

**Einfluss unkonventioneller Medien auf die
Selektivität ThDP-abhängiger Enzyme**

T. Gerhards (2013), XIV, 199 pp

ISBN: 978-3-89336-846-4

Band / Volume 55

**Aufbau einer Vierspitzen-
Rastertunnelmikroskop/Rasterelektronenmikroskop-Kombination
und Leitfähigkeitsmessungen an Silizid Nanodrähten**

E. Zubkov (2013), 150 pp

ISBN: 978-3-89336-848-8

Band / Volume 56

**Interplay between magnetic and dielectric phenomena
at transition metal oxide interfaces**

D. Schumacher (2013), IV, 128 pp

ISBN: 978-3-89336-855-6

Band / Volume 57

**Single NdPc₂ Molecules on Surfaces:
Adsorption, Interaction, and Molecular Magnetism**

S. Fahrendorf (2013), viii, 100 pp

ISBN: 978-3-89336-856-3

Band / Volume 58

**Heyd-Scuseria-Ernzerhof Screened-Exchange Hybrid Functional for
Complex Materials: All-Electron Implementation and Application**

M. Schlipf (2013), XV, 170 pp

ISBN: 978-3-89336-857-0

Band / Volume 59

**Orbital-dependent exchange-correlation functionals in density-functional
theory realized by the FLAPW method**

M. Betzinger (2013), vi, 173 pp

ISBN: 978-3-89336-858-7

Band / Volume 60

Structural influences on electrical transport in nanostructures

R. D. Frielinghaus (2013), viii, 190 pp

ISBN: 978-3-89336-867-9

Band / Volume 61

Study of intermolecular interactions in hetero-organic thin films

B. Stadtmüller (2013), viii, 198 pp

ISBN: 978-3-89336-871-6

Schriften des Forschungszentrums Jülich
Reihe Schlüsseltechnologien / Key Technologies

Band / Volume 62

**Structure, magnetism and excitations in some
Mn-based magnetocaloric effect compounds**

M. Gottschlich (2013), 175 pp

ISBN: 978-3-89336-874-7

Band / Volume 63

Neutron Scattering

Lectures of the JCNS Laboratory Course held at Forschungszentrum Jülich and
the research reactor FRM II of TU Munich

edited by Th. Brückel, G. Heger, D. Richter, G. Roth and R. Zorn (2013),
ca 350 pages

ISBN: 978-3-89336-880-8

Band / Volume 64

Neutron Scattering

Experiment Manuals of the JCNS Laborator Course held at Forschungszentrum
Jülich and the research reactorFRM II of TU Munich

edited by Th. Brückel, G. Heger, D. Richter, G. Roth and R. Zorn (2013),
ca. 150 pages

ISBN: 978-3-89336-881-5

Band / Volume 65

Solutions of Exercises in “An Introduction to Dynamics of Colloids”

J. K. G. Dhont, K. Kang (2013), 143 pp

ISBN: 978-3-89336-882-2

Band / Volume 66

**Strukturelle und chemische Charakterisierung von selbst-assemblierten
Monolagen organischer Moleküle auf Oberflächen**

M. Müller (2013), 168 pp

ISBN: 978-3-89336-883-9


Band / Volume 67

**Adsorption of (hetero-)organic Phthalocyanine
and PTCDA thin films on Ag(111)**

C. Kleimann (2013), iv, 149 pp

ISBN: 978-3-89336-888-4

Weitere **Schriften des Verlags im Forschungszentrum Jülich** unter
<http://wwwzb1.fz-juelich.de/verlagextern1/index.asp>



Schlüsseltechnologien / Key Technologies
Band / Volume 67
ISBN 978-3-89336-888-4

